A COUPLED INITIALIZATION STRATEGY TO REPRESENT HISTORICAL ATLANTIC MERIDIONAL OVERTURNING CIRCULATION DECADAL VARIATION AND PREDICTION

A Dissertation

by

QIUYING ZHANG

Submitted to the Graduate and Professional School of
Texas A&M University
in partial fulfillment of the requirements for the degree of

DOCTOR OF PHILOSOPHY

Chair of Committee,	Ping Chang
Co-Chair of Committee,	Shaoqing Zhang
Committee Members,	Ramalingam Saravanan
	Achim Stössel
Head of Department,	Shari Yvon-lewis

May 2022

Major Subject: Oceanography

ABSTRACT

Decadal variations of the Atlantic meridional overturning circulation (AMOC) play a key role in decadal climate predictions. Previous studies suggest that forced ocean — sea-ice (FOSI) model simulations, which can represent historical decadal variation of AMOC under the observation-based atmospheric forcing, can be used to initialize decadal climate predictions with high skill in the North Atlantic. However, the methodology of the FOSI initialization can generate large ocean initialization shocks, potentially lowering model predictive skill based on seasonal climate prediction studies. This study aims to address the initialization shock issue by developing and evaluating an alternative initialization strategy in which historical AMOC decadal variation is simulated in a fully coupled predictive model. It is shown that a simple initialization strategy that restores model sea-surface temperature (SST) and sea-surface salinity (SSS) to those of FOSI can effectively reproduce historical AMOC decadal variation and the associated dense water propagation in FOSI. This approach can be viewed as an extension of the SST-restoring technique widely used in the seasonal prediction community with a key emphasis on the inclusion of SSS restoring. Extensive model sensitivity experiments, including using observed SST and SSS as restoring target, are conducted to further investigate the role of SSS restoring in simulating historical AMOC decadal variability. The results suggest that restoring coupled model SSS to observed climatological SSS while restoring SST to full observed values can reproduce historical AMOC decadal variation in FOSI, indicating that the role of SSS restoring is primarily

to correct coupled model salinity bias, ensuring a realistic surface density distribution that is essential for a realistic simulation of AMOC decadal variation. Preliminary decadal prediction experiments using this simple coupled initialization strategy show that the historical AMOC decadal variation replicated by SST- and SSS- restoring in a coupled predictive model can indeed lead to improved model prediction skill in the North Atlantic compared to FOSI initialization. This new initialization strategy offers a potential improvement to decadal climate predictions by reducing initialization shock using only observed SST and SSS that are more readily available.

DEDICATION

I dedicate this dissertation to my beloved parents, 张代胜 (Daisheng Zhang) and 曹文艳 (Wenyan Cao) for their unconditional love and encouragements.

ACKNOWLEDGEMENTS

First and foremost, I would like to express my sincere appreciation to my advisor Dr. Ping Chang, for leading me to experience the magic of science and encouraging me when I faced difficulties. He helps me walk through all the writings and present my research logically. His enthusiasm, curiosity and responsible attitude for research have deeply inspired me and will benefit not only my research but also my life.

I would like to extend my thanks to my co-chair, Dr. Shaoqing Zhang, for his suggestions to my experiments and his immediate feedback, which let me almost forget time zone difference. I would like to thank Dr. Ramalingam Saravanan and Dr. Achim Stössel for serving on my dissertation committee and for helpful discussions during committee meetings. I would like to thank Dr. Stephen Yeager and Dr. Gokhan Danabasoglu for their insights on my work. I'm also grateful for Dr. Who Kim, Dr. Frederic Castruccio for providing me the datasets and guidance on running my experiments.

Thanks also goes to all my dear friends and colleagues for their supports. I feel so lucky to be at TAMU and in Ping's group. I owe special thanks to Kelly Williams, who helps me correct spelling and grammar mistakes of this dissertation. I'm grateful for Gaopeng Xu, my 6-year classmate and groupmate. We together stayed up for assignments, joined the Big Event, complained our IQs, and fought for our graduations. I'm grateful for Xue Liu and Dan Fu, who helped me quickly adapt to the new environment when I came here. I would like to thank my dear roommate Hedanqiu Bai

and my friend Chenrui Diao, for their company during the pandemic, talking our futures and dreams, criticizing television dramas and policies.

I am grateful for China Scholarship Council for their financial support. I am also grateful for the Texas A&M University Supercomputing Facility and the Texas Advanced Computing Center at the University of Texas at Austin, which provided the computing resources used in this dissertation.

Finally, I would like to express my thanks to my lifelong friend, Sijia Zou. I am always filled with energy after talking with her. We laugh, share and grow up, and will grow old together. I would like to express my deepest thanks to my beloved parents, Daisheng Zhang and Wenyan Cao, who trust my every decision and raise me up to more than I can be.

CONTRIBUTORS AND FUNDING SOURCES

Contributors

This work was supervised by a dissertation committee consisting of Professor Ping Chang (advisor), Professor Shaoqing Zhang (co-advisor) and Professor Achim Stössel of the Department of Oceanography, and Professor Ramalingam Saravanan of the Department of Atmospheric Sciences.

The CESM2 FOSI and HIST data were provided by Dr. Stephen Yeager and Dr. Who Kim at NCAR. Initializations from SMYLE were provided by Dr. Stephen Yeager at NCAR.

All other work conducted for the dissertation was completely by the student independently.

Funding Sources

Graduate study was supported by a fellowship from Texas A&M University and China Scholarship Council.

NOMENCLATURE

ACC	Anomaly Correlation Coefficient
AMOC	Atlantic Meridional Overturning Circulation
AMV	Atlantic Multidecadal Variability
CDA	Coupled Data Assimilation
CESM	Community Earth System Model
CGCM	Coupled General Circulation Model
CMIP	Coupled Model Intercomparison Project
DPLE	Decadal Prediction Large Ensemble Project
GPCPv2.3	Global Precipitation Climatology Project Version 2.3
ENSO	El Niño-Southern Oscillation (ENSO)
ERSSTv5	Extended Reconstructed Sea Surface Temperature, version5
FOSI	Forced Ocean – Sea-Ice Model Simulations
HIST	Fully Coupled Historical Simulations
MAR	Mid-Atlantic Ridge
MSSS	Mean-Square Skill Score
NAO	North Atlantic Oscillation
LF	Low-Frequency
LS	Labrador Sea
LSW	Labrador Sea Water
LSWM	Labrador Sea Water Mass
ODA	Ocean Data Assimilation

PDV	Pacific Decadal Variability
PPVF	Potential Predictable Variance Fraction
OSNAP	Overturning in the Subpolar North Atlantic Program
RMSE	Root Mean Square Error
SMYLE	the Seasonal-to-multiyear Large Ensemble
SPNA	Subpolar North Atlantic
SSH	Sea Surface Height
SSS	Sea Surface Salinity
SST	Sea Surface Temperature
STD	Standard Deviation
T295m	Upper 295-m Averaged Ocean Temperature
UI	Uninitialized Simulations
WMF	Water Mass Formation
WMT	Water Mass Transformation
WOA13v2	World Ocean Atlas 2013 version 2
Z_{LSW}	Labrador Sea Water Thickness
ΔACC	Anomaly Correlation Coefficient Differnce
ΔZ_{LSW}	Labrador Sea Water Thickness Anomaly

TABLE OF CONTENTS

Page

LIST OF FIGURES

Page

LIST OF TABLES

Page

CHAPTER I

INTRODUCTION

1.1 Benefits and Challenges of Decadal Climate Prediction

El Niño-Southern Oscillation (ENSO), Pacific Decadal Variability (PDV) and Atlantic Multidecadal Variability (AMV) are the most dominant modes of global sea surface temperatures (SST) after removing the warming trend (Tung et al., 2019). Among these three, ENSO is the dominant mode at interannual timescales and has already been studied extensively. Since the seminal work of Bjerknes (Bjerknes, 1969), a vast amount of research has been carried out to understand the structure and evolution of ENSO (Wallace et al., 1998 and references therein), as well as ENSO mechanism (Philander, 1990; Neelin et al., 1998; Dijkstra, 2006). This understanding along with the establishment of the tropical ocean-atmosphere observing system (TAO array, https://www.pmel.noaa.gov/gtmba/building-tao) has laid the foundation for seasonal climate prediction, which has been in operation since the 1980s. Skillful ENSO-based seasonal climate predictions have brought immeasurable benefits for society (e.g. Latif et al., 1998; Hansen et al., 2002).

However, seasonal climate predictions alone are not sufficient to solve climate issues that occur over the longer timescales (Kushnir et al., 2019). Sahel droughts over West Africa, for example, cannot be fully explained by ENSO-related SST in the Pacific (Giannini et al. 2003) and occur on decadal timescales (Rodríguez-Fonseca et al., 2015 and references therein; Villamayor et al., 2015). Atlantic major hurricane frequency also exhibits multidecadal variability based on observations since the 1940s (Landsea et al.,

1999; Goldenberg et al., 2001; Yan et al., 2017). Observational studies point out that AMV is a leading factor causing sea level pressure anomalies between subtropical and subpolar North Atlantic, which can have a major impact on the North Atlantic westerlies, precipitation, surface heat loss and so on (Zhang et al., 2019 and references therein). Given considerable impact of decadal climate variability on society and environment, developing the capability of decadal climate prediction can be extremely valuable and beneficial (Smith et al., 2019). Nevertheless, compared to ENSO-based seasonal climate predictions, decadal climate prediction efforts which started much later in the early 2000s (Meehl et al., 2009) are much more challenging. This may be due to combined reasons of 1) a less well-established theoretical basis for decadal climate prediction and 2) an inadequate observing system for initializing decadal climate prediction.

One of the active research areas in decadal climate prediction is the predictability of the AMV in the North Atlantic, and many studies indicate that AMV's impact may be far beyond the North Atlantic with some studies suggesting an impact of AMV on PDV (e.g. Zhang & Delworth, 2007). The traditional definition of AMV index is a linearly detrended SST anomalies averaged over the entire North Atlantic subject to a low-pass filter. Regression of the AMV index on SST anomalies reveals an inhomogenous warming amplitudes (horseshoe pattern) in the North Atlantic with strong warming in the subpolar North Atlantic and cooling in the South Atlantic (Figure 1.1). The leading driver of AMV is still under considerable debate because of certainties raised from the relatively short observation record, and the deficiency of a coupled climate model

leading to large model bias (e.g. Ruprich-Robert et al., 2021). The weak coupling between atmosphere and ocean also makes it difficult for coupled climate models to fully capture AMV dynamics (e.g. Kim et al., 2018).

Many studies suggest AMV is a result of internal ocean circulation variations associated with the Atlantic Meridional Overturning Circulation (AMOC). AMOC transports heat meridionally to the high latitudes of the North Atlantic and helps bring high-latitude changes to the tropics (Zhang et al.,2016). Yan et al. (2018) showed that low-frequency (LF) AMOC can generate AMV by regressing LF SST on LF AMOC index in the North Atlantic using multimodal simulations. The "horseshoe" patterns of AMV appeared in all simulations, exhibiting stronger amplitudes when the strength of AMOC was stronger. Zhang et al.(2019) summarized observed key elements of AMV such as the propagation of AMV SST anomalies along the "horseshoe" pathway, the anticorrelated variations between the upper and deep ocean temperature in the Subpolar North Atlantic (SPNA), the positive correlation between observed AMV and LF turbulent surface heat flux and so on, which could be reproduced by AMOC-driven AMV. For example, Zhang et al. (2016) found the surface turbulent heat flux damps the North Atlantic SST in a Coupled General Circulation Model (CGCM), however, it can play a leading role in the non AMOC-driven AMV model (a slab ocean model). The anticorrelation between subsurface and SST in tropical North Atlantic, another observed key element of AMV, also exists in CGCMs, which possibly results from the combined effects of AMOC and the thermocline adjustment (Zhang, 2007). In addition, it has been hypothesized that AMOC can provide a deep ocean memory for AMV decadal

prediction. Many modeling studies suggest a realistic AMOC initialization can lead to skillful decadal predictions of SST in the North Atlantic (Yeager et al., 2012; Karspeck et al., 2015 and references therein), and the stronger LF AMOC amplitudes in the simulations can lead to more predictable LF North Atlantic SSTs (Yan et al., 2018). Therefore, it is important to initialize a realistic AMOC variation for decadal prediction.

Although the theory of AMOC-driven AMV is persuasive and has been supported by some observations, other studies show that AMV is a LF SST variation mainly forced by atmosphere (e.g., Booth et al., 2012; Cane et al., 2017; Clement et al., 2015; Murphy et al., 2017). Radiative forcing, such as greenhouse gases and sulfate aerosols, and stochastic atmospheric forcing like the North Atlantic Oscillation (NAO) are considered two major sources of forcing for AMV. Booth et al. (2012) showed that anthropogenic aerosol forcing in the 20th century may produce an AMV-like pattern if climate models properly include aerosol-cloud microphysical effects, which is deficient for many coupled climate models. However, Zhang et al. (2013) argued that the model used by Booth et al. (2012) overestimated the aerosol effects leading to a decreasing warming trend in the upper ocean North Atlantic and a salinification trend in the SPNA, which are unrealistic. Mann et al. (2020) and Mann et al. (2021) directly questioned the existence of internal decadal or multidecadal oscillations in the climate model simulations. They pointed out the volcanic radiative forcing before the industrial period (1000-1835CE) and the competition of greenhouse gas and aerosols after the year 1850 are the driving force behind the so-called "AMV". Mann et al. (2020) suggested that LF variability of radiative forcings can determine the LF SST variability after removing

linear trends. Mann et al. (2016) suspected it is the Pinatubo eruption (the second-largest volcanic eruption in the 20th century) in 1991, rather than the phase of internal decadal variability, which leads to the cold SSTs in the mid-1990s, an important information of initial conditions resulting in the success of predicting the early-2000s hiatus of global warming (Meehl et al., 2014). Clement et al. (2015) simulated AMV pattern using a slab ocean model, suggesting the NAO is the leading cause of AMV. However, the negative correlations between the net surface flux and the LF SST in SPNA are inconsistent with the observed AMV elements (Zhang et al., 2016). The successful prediction at decadal lead times also provide evidence shows the predictable AMV signal cannot be simply from the surface heat flux forcing, because the atmospheric forcing is unpredictable beyond its persistence (Zhang et al., 2016; Manne et al. 2020).

In this study, we are taking the view that LF AMOC is a dominant driver of AMV, even though we are fully aware of the controversy about this issue. The focus of this study is on how to improve the representation of historical AMOC decadal variation in coupled climate models, rather than on the driver of AMV. We hypothesize an improved AMOC representation can lead to more skillful forecast of SST on decadal timescales.

1.2 AMOC and Decadal Variability

AMOC can be characterized by a streamfunction (Unit: Sv, 1 Sv=10^6 m^3/s) of the zonal integrated meridional and vertical volume transport in depth or density coordinates (e.g., Buckley and Marshall, 2016; Zhang, 2010a, 2010b; Li et al., 2018). At any given time, this so-called overturning streamfunction is defined as follows:

$$\mathrm{AMOC_z}(y,z) = \int_z^{\eta} \int_{x_w}^{x_e} v\,dx\,dz, \quad (1)$$

or, $$\mathrm{AMOC_\sigma}(y,\sigma) = \int_{\sigma_{min}}^{\sigma} \int_{x_w}^{x_e} v\,dx\,d\sigma, \quad (2)$$

where $\mathrm{AMOC_z}$ and $\mathrm{AMOC_\sigma}$ represent the AMOC streamfunction in depth and density coordinates, respectively, v is the meridional velocity, η is the height of the free surface, σ_{min} is the density surface. x_e and x_w are the eastern and western boundaries at a particular depth or density. Kwon and Frankignoul (2014) discussed the different focus of the circulation represented by $\mathrm{AMOC_z}$ and $\mathrm{AMOC_\sigma}$. They showed that $\mathrm{AMOC_z}$ emphasizes the location of deep water formation, while $\mathrm{AMOC_\sigma}$ focuses on water mass formation and transformation. $\mathrm{AMOC_z}$ and $\mathrm{AMOC_\sigma}$ are similar south of 40°N because the relatively weak density gradients between eastern and western basin. The higher latitudes, the more obvious differences occur between $\mathrm{AMOC_z}$ and $\mathrm{AMOC_\sigma}$.

As mentioned previously, decadal variability of AMOC is important for the variation in meridional transport of ocean heat, salinity, and carbon to adjust the balance between low and high latitudes, and between surface and deep oceans (Kostov et al., 2014; Buckley and Marshall, 2016), which in turn can impact on the climate not only in the North Atlantic sector, including Europe and North America, but also the globe. However, the continuous measurement of the AMOC only began in the year 2004 when the RAPID-MOCHA array was established along 26.5°N in the North Atlantic (Smeed et al., 2019). Before 2004, AMOC can only be reconstructed based on paleo proxies, SST and Argos. The reconstructed AMOC suffers from larger uncertainties occasionally leading to controversial results due to different reconstructed methods and resolutions

(Mann et al., 2021). The birth of RAPID provided a new and reliable reference for the recent evolution of AMOC (e.g. Bryden et al, 2005; Moat et al., 2020). However, 26.5°N is a latitude where wind-driven ocean circulation plays a leading role in AMOC variability (Larson et al., 2020), and thus the RAPID time series does not provide a key constrain for AMOC-related decadal prediction. In contrast, the deep convection region in the high latitudes provide more critical information for predicting AMOC changes at decadal timescales.

To better observe AMOC variation, and its connectivity with the tropics through the deep boundary current system, a new observational project – *Overturning in the Subpolar North Atlantic* (OSNAP) was launched in 2014 (Lozier et al., 2017; https://www.o-snap.org/). The observing system is divided into two legs: leg one extends from southern Labrador to the southwestern tip of Greenland (OSNAP West), the second leg extending from the southeastern tip of Greenland to Scotland (OSNAP East). The analysis from the 21-month OSNAP observations questioned the contribution of Labrador Sea Waters (LSW) formation to the AMOC variability which has been regarded as a key in the traditional view based on non-eddy-resolving climate model simulations (Lozier et al. 2019). Lozier et al. argued those non-eddy-resolving climate models simulate unrealistically strong LSW formation, and thus over-emphasize the role of LSW in AMOC decadal variability. However, a recent study by Yeager et al. (2021) shows, based on a multi-century eddy-resolved coupled climate model simulation, increasing model resolution results in a much improved simulation of LSW which is consistent with OSNAP observations, and still the decadal AMOC variation in the eddy-

resolving model simulation is driven by LSW. Thus, the LSW-dominated AMOC decadal variation in non-eddy-resolving climate model simulations may still be a valid mechanism. This study will use a non-eddy resolving climate model to simulate historical AMOC decadal variation.

Danabasoglu et al. (2016) compared the variation of AMOC from 1958 to 2007 among twenty non-eddy-resolving ocean—sea-ice coupled models forced by the same observation-based atmospheric forcing. They showed nearly all models displayed a consistent decadal variation in the AMOC: steady from the late 1950s to the mid- to late-1970s followed by an intensification till the mid- to late-1990s, and then a weakening towards the end of integration. These results are consistent with the AMOC variation inferred from observed surface fields (Latif et al., 2004; Huck et al., 2008; Swingedouw et al., 2013). This inverted U-shaped time variation is regarded as a defining characteristic of the AMOC decadal variation that is critical for decadal predictions. Capturing this AMOC decadal variation in initialized predictions is a key reason that initialized predictions have a better skill in forecasting North Atlantic SST at decadal times than uninitialized predictions (e.g., Robson et al., 2012; Yeager and Robson, 2017).

1.3 Initialization Methods for Decadal Climate Prediction

1.3.1 A Brief Description of Initialization Technique

Initial conditions are critically important for skillful decadal prediction (e.g. Boer et al., 2013; Yeager and Robson, 2017; Yeager et al., 2018). There are several

strategies to generate initial conditions, including a “brute force” method, “nudging” method, hindcast initialization, and coupled data assimilation (Meehl, 2021).

The “brute force” method refers to a procedure where initiations are derived from an existed analysis or reanalysis product after interpolating the dataset to the model grid (Meehl, 2021). One disadvantage of this method is the existence of possible mismatches between different components (ocean and atmosphere for instance) and mismatches between analysis/reanalysis state and model state, which may lead to initialization shocks and large model drift.

“Nudging” method or “restoring” method may be used to reduce, to some extent, these mismatches, which may lead to improved forecast skill. This method typically involves relaxing the prediction model state to a “truth” which can be derived from a reanalysis product or observational source. By combining the observational information directly into prediction models, which has already been applied to seasonal climate prediction and shown some success in improving model forecast skill (e.g., Chen et al., 1995), Keelyside et al. (2008) extended this method to decadal prediction and showed an improved surface temperature hindcast skill in parts of the North Atlantic. The number of selected restoring variables and restoring strength are important: too many variables may disrupt the prediction modeling system; too strong “nudging” may lose the effectiveness of model adjustment, however, too weak “nudging” may miss the observed information.

Hindcast initialization is to derive initial conditions from a forced model simulation where forcing is based on observations. The decadal prediction experiment

by Yeager et al. (2018) is based on this initialization method. They took the last forcing cycle of forced ocean – sea-ice (FOSI) model simulations using observation-based atmospheric forcing to derive initial conditions for a decadal prediction large ensemble (DPLE) experiment using the Community Earth System Model (CESM). The results show more skillful prediction of North Atlantic SST anomalies and upper ocean heat content anomalies than that of uninitialized simulations and persistent predictions at decadal timescales. The skill of SST prediction also leads to a skillful prediction of monsoonal rainfall associated with the West Africa Monsoon. However, this hindcast initialization can suffer from strong initialization shock due to the inconsistency in atmospheric forcing between FOSI and a coupled prediction model. This initialization shock may have a negative impact on model prediction skill.

Coupled data assimilation (CDA) is the most expensive and advanced initialization method in which available observations in the atmosphere and ocean are assimilated simultaneously into a coupled prediction model, and initial conditions for predictions are directly generated by the CDA within the coupled model. Ideally, this method is the most effective procedure to generate initial conditions, provided that continuous observations are available for both the atmosphere and oceans. In practice, however, deep ocean observations below 2000 m are sparse, creating difficulties in representing AMOC and its decadal variation. For example, Karspeck et al. (2017) compared six different ocean data assimilation (ODA) products, less complicated than CDA (Penny, 2017), to a multi-model ensemble of FOSI simulations and showed the ODA products are less consistent in their year-to-year AMOC changes. They suggest a

possible reason for this consistency may be the lack of deep ocean observations that cause an imbalanced upper and deeper ocean state. As a result, there are no conclusive studies at the moment suggesting that CDA initialization is more superior than other methods in initializing decadal climate prediction.

1.3.2 Initialization Shocks and Prediction Drifts

Because of insufficient observations and biases in coupled prediction models, all initialization techniques we discussed above can introduce errors during predictions, which can limit decadal prediction skills. In the following, we discuss two commonly encountered errors in decadal prediction: ocean initialization shocks and prediction drifts.

The main cause for the ocean initialization shock is the mismatch between the atmospheric forcings used to generate initial conditions, and those in coupled climate models used for prediction. Climate models are notorious for their bias problems. Even given a perfect observed SST forcing, atmospheric models can generate strong biases in surface winds and surface fluxes. An example, Figure 1.2 shows a comparison between the observed pseudo wind stress from QuikSCAT during 2000 to 2008, and simulated pseudo wind stress from the atmospheric component of CESM version 2 (CESM2) forced by observed SST and sea ice. It is evident that there are significant differences between the observed and simulated pseudo wind stress. The simulated values are generally too weak in the tropics, but too strong in the subtropics and the Southern Ocean (Figure 1.2b). This atmospheric model bias pattern in pseudo wind stress carries over to the fully coupled CESM2 simulation as revealed by the similarity of the bias

patterns between the atmosphere-only (Figure 1.2b) and coupled model simulations (Figure 1.2c), suggesting the SST bias in CESM2 is secondarily important for the wind stress bias. This biased wind stress will cause imbalance between the predictions and the initial conditions, causing the ocean to adjust. Even though the short memory in the atmospheric component may not largely impact on the skill of decadal prediction (different from sub-seasonal to seasonal predictions), the adjustment may introduce spurious ocean waves and SST anomalies which can have an impact on forecast qualities due to long-memory in the ocean component. Therefore, to reduce this ocean initialization shock, it is highly desirable to initialize predictions with a more balanced state in the coupled model.

Prediction drifts come from the different mean states between initial conditions and free simulations (no extra forcings except external forcings) of a coupled prediction model. Prediction simulations can drift significantly from initial conditions to the coupled prediction model "preferred" states if the difference between the two mean states is large. As such, using "brute force" and ODA techniques to initialize decadal predictions can lead to major prediction drifts, if a coupled prediction model suffers from severe bias problems.

Model drift problems may be reduced in the case of hindcast initialization, if, an identical ocean model is used in hindcast simulation and coupled model prediction, simply because biases due to intrinsic ocean model physics and numerics will be the same for both the hindcast and coupled simulations. However, even in this case, the mean state of the hindcast (e.g., FOSI) and free simulation of the coupled prediction

model can be different because of the observation-based forcing used in the hindcast can be significantly different from coupled climate models (e.g., Figure 1.2c). Figure 1.3 shows the difference of upper ocean mean temperature and salt content (upper 500 m) between a FOSI simulation and fully coupled CESM2 historical simulations. As can be seen, upper ocean temperature in FOSI is colder than CESM2 in mid- and high-latitudes and equatorial Pacific, but warmer in other tropical regions. Upper ocean salinity in FOSI is saltier in most regions with exception of the North Atlantic. Thus, one can expect these differences in the mean states of upper ocean temperature and salinity will lead to prediction drifts. These drifts can potentially affect model forecast skill. To reduce drift, it is highly desirable to reduce the differences of ocean mean state in initial conditions and prediction models.

1.4 Objectives

Motivated by the above discussion and previous studies, the fundamental purpose of this dissertation is to develop and evaluate a potential coupled model initialization technique alternative to the hindcast initialization based on FOSI simulations for decadal climate prediction by Yeager et al. (2018). A key requirement for this coupled model initialization technique is that it must be able to represent realistic AMOC decadal variation in a fully coupled model. Since the same fully coupled model will be used for initialization and prediction, one expects the inconsistency of the atmospheric state will be reduced, and thus possibly lead to a reduction in the ocean initialization shock and potentially improve model forecast skills. To simulate realistic AMOC decadal variability in a fully coupled model, we need to constrain upper ocean density variability

to observations, as near-surface buoyancy fluxes are shown to play an important role for AMOC decadal variability. A straightforward way of constraining model surface buoyancy fluxes is to simply "restore" coupled model simulated SST and sea surface salinity (SSS) to observed values. Therefore, in this study, we will explore the question: To what extent can a fully coupled model simulate historical AMOC decadal variations by simply restoring model SST and SSS. Specifically, this study attempts to address the following questions: Can "restoring" only SST and SSS, without any constrains on the deep ocean circulation, produce a realistic decadal variation of AMOC? Is this simple restoring method capable of capturing the key dynamical elements of AMOC changes that are critical for decadal prediction in the North Atlantic? Will this restored model solution be able to produce a more consistent atmospheric state that can potentially reduce ocean initialization shocks? How important is restoring SSS for the AMOC decadal variability? Are SSS anomalies critical for generating realistic local surface buoyancy flux anomalies that force AMOC variability at decadal timescales? Does this modeling strategy work in practice? These and other related scientific questions will be explored in the following chapters.

After describing the primary research approach, including a brief description of model, datasets, restoring technique, and several analyzed methods in Chapter 2, the following three chapters will focus on exploring the above scientific questions. Chapter 3 will evaluate the SST/SSS restoring technique on its ability of realistically representing AMOC decadal variation in the framework of CESM2. Several related key elements of AMOC relevant to decadal predictability will also be discussed. Chapter 4 will focus on

the role of SSS in simulating AMOC decadal variability. Results from an extensive set of model sensitivity experiments will be discussed. In particular, the importance of SSS anomalies in simulating realistic AMOC decadal variability will be examined. Chapter 5 will demonstrate whether SST/SSS restoring initialization improves decadal prediction skill compared to hindcast initialization. An overall summary and some future works will be presented in Chapter 6.

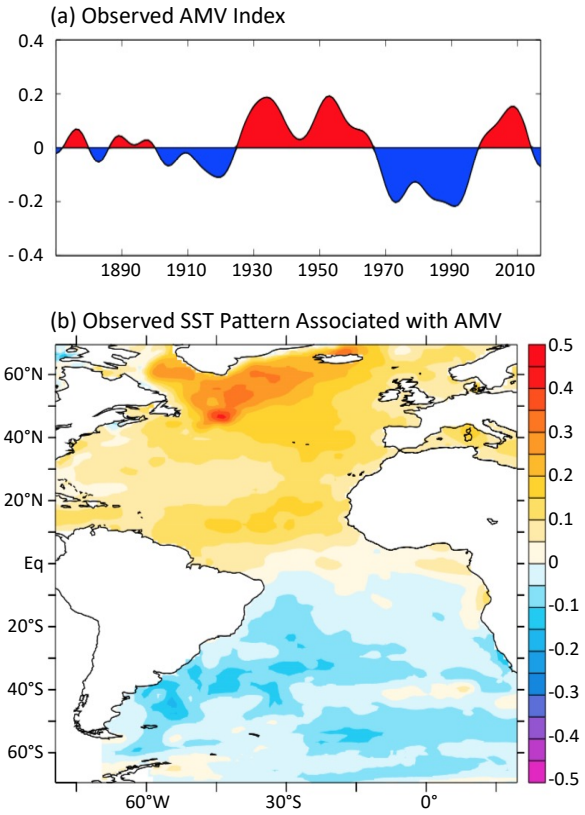

Figure 1.1 (a) Observed AMV index which is defined as the 10-year low-pass-filtered area-weighted average of SST anomalies over the North Atlantic (80°W to 0°E, 0–65°N), and (b) the regression of SST anomalies on the observed AMV index. The figure is edited from Zhang et al. (2019). The dataset is from Hadley Centre Sea Ice and Sea Surface Temperature data set (HADISST; Rayner et al., 2003). The SST anomaly at each grid point is computed by removing the local component regressed on the global mean SST anomaly.

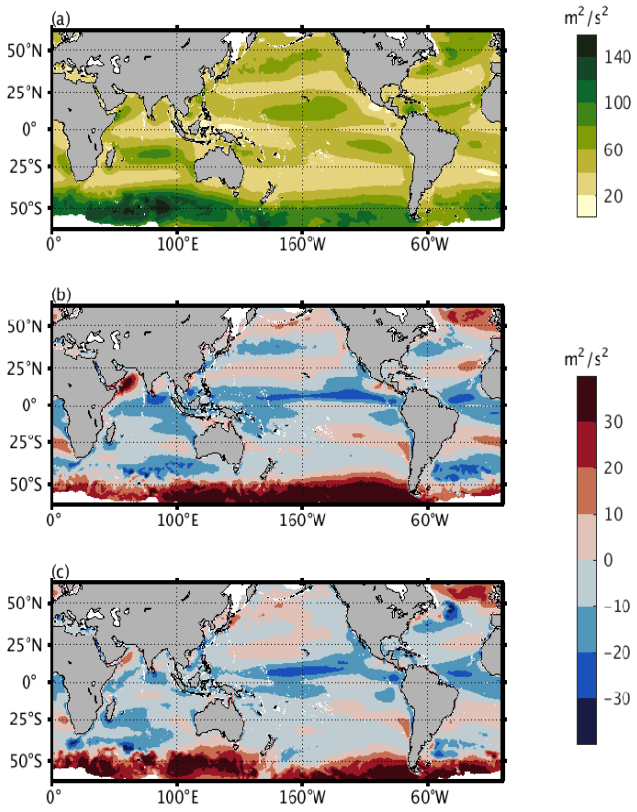

Figure 1.2 (a) magnitude of pseudo wind stress from QuikSCAT; (b) difference between CESM2 atmosphere-only simulations and QuikSCAT; (c) difference between CESM2 coupled historical simulation and QuikSCAT. The atmosphere - only result is based on ensemble average of 10 members forced by observed SST and ice (http://www.cesm.ucar.edu/working_groups/CVC/ simulations/cam6-prescribedsst.html). The CESM2 result is based on ensemble average of 11 members of CESM2 historical climate simulations (see more details in Danabasoglu et al., 2020). All results are based on the period of 2000-2008 and pseudo wind stress, defined as wind stress dividing by both air density and drag coefficient, is in unit of m^2/s^2 . The horizontal resolution of all CESM2 simulations is nominal 1°.

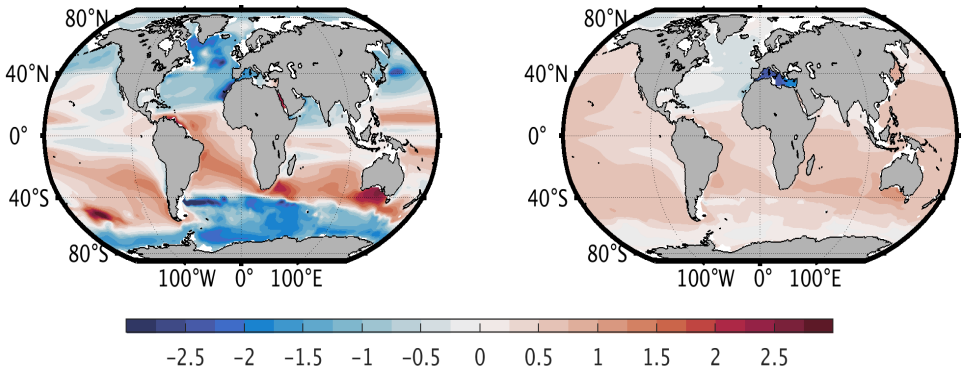

Figure 1.3 Difference of upper 500 m averaged temperature (left; unit: ºC) and upper 500m averaged salinity (right; unit: psu) between FOSI and fully coupled CESM2 historical climate simulation. The analysis period is the temporal mean between 1975 and 2014.

CHAPTER II

METHODS

2.1 Model Description

All the numerical experiments in this study are based on the NCAR CESM2—the latest generation of CESM, with a nominal 1° horizontal resolution forced by historical climate forcings following the protocol of Coupled Model Intercomparison Project (CMIP) phase 6 from the year 1958 to 2014. The information related to code and downloading scripts is available at https://escomp.github.io/CESM/versions/cesm2.1/html/downloading_cesm.html. CESM2 consists of atmosphere, ocean, land, sea ice, river, and coupler, and is one of the most widely used climate models in the research community (Danabasoglu et al. 2020).

The atmosphere component is the Community Atmosphere Model Version 6 (CAM6) with a Finite Volume dynamical core (Lin & Rood, 1997). Compared with the previous versions, CAM6 has all new physics parameterizations except for the radiation physics (Rapid Radiative Transfer Model for General circulation models, RRTMG; Iacono et al., 2008). The horizontal resolution is 1.25° in longitude and 0.9° in latitude with 32 vertical levels and the model top is set at 2.26 hPa.

The ocean component is the Parallel Ocean Program Version 2 (POP2; Smith et al., 2010), a z-level vertical coordinate ocean general circulation model. The North Pole in POP2 is placed on Greenland instead of its geographical location in order to avoid numerical issues within the Arctic Ocean. Thus, the POP2 grid in the high latitudes in the Northern Hemisphere are highly non-uniform, while the grid in the Southern

Hemisphere is the spherical coordinate. The horizontal resolution is 1.125° in the zonal direction and varies in the meridional direction with finest resolution of 0.27° at the equator and coarsest resolution in the northwestern Pacific Ocean. There are 60 z-levels in the vertical, with the finest resolution of 10 m in the upper 160 m. Although, the POP version in CESM2 is the same with Community Climate System Model version 4 (CCSM4) and CESM1, it is noted that there are some improvements including increasing mesoscale eddy diffusivities at depth, moving the Caspian Sea to land components as a lake and so on.

Sea-ice component uses CICE Version 5.1.2 (CICE5; Hunke et al., 2015). The horizontal resolution shares the same grid gx1v7 with the ocean component. The vertical resolution is increased to eight layers in order to better resolve the temperature and salinity profiles than previous versions.

The Community Land Model Version 5 (CLM5; Lawrence et al., 2019) is used for the land component. The horizontal resolution of the land component is identical to that of the atmosphere component. Soil biogeochemistry scheme is not included in our experiments.

The Model for Scale Adaptive River Transport (MOSART; Li et al., 2013) is used for river transport with grid resolution 0.5° x 0.5°, which is totally different from previous CESM versions.

The coupler in CESM2 is based on a new modeling framework, known as the Common Infrastructure for Modeling the Earth (CIME; http://github.com/ESMCI/cise).

More details for the description and improvement of CESM2 are provided in Danabasoglu et al. (2020).

2.2 Datasets

2.2.1 Observations and Analysis Datasets

The NOAA Extended Reconstructed Sea Surface Temperature, version 5 (ERSSTv5; Huang et al., 2017) is used in this study for SST comparison, and as one of the restored target variables in model sensitivity experiments. ERSSTv5 is a monthly SST dataset from 1854 to present on a 2° x 2° grid (88.0°N - 88.0°S, 180.0°W – 180.0°E), based on statistical interpolation of the International Comprehensive Ocean-Atmosphere Data Set (ICOADS) release 3.0 data which contains observations from many different observing systems. Argo float data has been used since approximately year 2000, which improves the agreement with SST estimates from satellite observations.

The three-dimensional temperatures and salinities are from the monthly mean dataset, the UK Met Office EN4.2.1 objective analysis (Good et al., 2013), with horizontal resolution of 1^{o} from 1900 to present (89.0°N - 83.0°S, 1.0°E – 360.0°E). It is used for subsurface comparison with the model simulations. This dataset is based on a collection of historical ocean temperature and salinity profiles in the global oceans to which a series of quality control checks have been applied, including uncertainty estimates. It should be noted the analyses relax to climatology which covers over 1971-2000 from EN2 when any observations are absent. Thus, a trend may be unrealistic if there were no observations. The uncertainty has apparently been improved globally as

time develops, particularly after the 2000s as Argo float data has been encompassed, and increases when the depth is deeper than around 300 m for both temperature and salinity which may be due to the historical lack of observations at depth (see details in Good et al., 2013 Figure 7). Decade-year uncertainty maps could bring us more details of to what extent EN4.2.1 has been improved at surface level over the period of our numerical experiments (Figure 2.1). The uncertainty is obviously decreased in the open seas. However, most of western boundary current regions and the Labrador Sea region (LS) are still waiting for further improvement.

World Ocean Atlas 2013 version 2 (WOA13v2; Zweng et al., 2013) SSS is also used here as one of the restoring targets. Unlike EN4.2.1 salinity, WOA13v2 is a set of objectively analyzed climatological *in situ* salinity with horizontal resolution of 1° averaged from 1955 to 2012, which is widely used for ocean model initialization and validation. However, the dataset still bears some limitations due to the sparse observations and inconsistent sampling in some regions and depths.

The monthly Global Precipitation Climatology Project Version 2.3 combined precipitation data set (GPCPv2.3; Adler et al., 2003) is used as the "truth" to compare the predicted precipitation in the Sahel region in Chapter 5. GPCPv2.3 is an integration of various satellite data sets over land and ocean, and a gauge analysis over land started from 1979. The resolution is 2.5°× 2.5° (88.75°N – 88.75°S, 1.25°E – 358.75°E). GPCP products provide the most complete precipitation analysis and uncertainty over land due to the careful combination of satellite-based rainfall estimates.

2.2.2 Simulations

Two existing CESM2 simulations are used in this study. One is CESM2 FOSI forced by the adjusted Japanese 55-year atmospheric reanalysis (JRA-55-do) product (Tsujino et al., 2018) and corrected by WOA13v2 freshwater flux at 1-year restoring timescale, which has been integrated for 5 forcing cycles, totaling 267 years of global ocean and sea-ice simulation. The first four cycles covered the 1958-2009 period and the fifth cycle extended from 1958 to 2016. Kim et al. (2018) showed that FOSI has a generally good agreement with the observations especially in the fields which have impact on the variability of AMOC at decadal timescales. Since long-term AMOC observations are not available, we will use FOSI simulation as the "truth" when validating AMOC decadal variations from our experiments. In addition, we will use FOSI SST and FOSI SSS from the last cycle as restoring target variables. This modeling framework that assumes FOSI simulation as the "truth" provides us a convenient and consistent method to evaluate the effectiveness of restoring SST and SSS in a fully coupled CESM2 to replicate AMOC decadal variation.

The other existing simulation used in this study is the CESM2 historical simulations (HIST) that include 11 ensemble members. All the members, following the CMIP phase 6 protocol, are integrated from 1850 to 2014 initialized by 11 different model years of the long CESM2 preindustrial control simulation. Danabasoglu et al. (2020) provide more details about the choice of initial conditions and forcings for HIST. HIST and all our numerical experiments share the same model code with identical model resolution. FOSI simulations are based on the same ocean and sea ice model used in

CESM2. This experimental design helps to minimize the simulation differences due to inconsistent model physics and numerics.

2.3 "Restoring" Technique

The "Restoring" technique is considered as a primitive coupled data assimilation approach. It is a common modeling method designed to constrain certain model variables to a specified target value which can be taken from either observations or experiments. The model variables are nudged to the specified field at a particular restoring timescale. Take temperature as an example, the effect of restoring can be modeled as:

$$\frac{dT}{dt} = -\frac{T_{model} - T_{target}}{\tau}, \tag{3}$$

where T_{model} is the simulated temperature, T_{target} is the specified temperature and τ is a timescale, often referred to as restoring timescale. The solution to equation (3) is

$$T_{model} = T_{target} + T_0 e^{-\frac{t}{\tau}}, \tag{4}$$

where T_0 is the difference between T_{model} and T_{target} at the initial time (t=0). T_{model} approaches T_{target} faster as τ decreases. That is, the longer the restoring timescale τ, the weaker restoring. However, too strong restoring of one variable may lead to large inconsistencies with other variables or with the same variable at different depths (Karspeck et al., 2017; Ortega et al., 2017). A proper τ should be chosen to balance the reality and model solution.

In this study, different restoring timescales, 3 days, 5 days and 10 days, have been tested to determine a suitable restoring strength before large ensemble experiments are carried out. The results from those restoring-time-scale-related sensitivity experiments show similarity in the temporal evolution of globally averaged temperature and salinity, ENSO patterns and AMOC, although annual SST and SSS biases become larger as the restoring strength is weaker. Given the similarity, the 10-day-restoring timescale is selected for all the strong restoring experiments.

2.4 Diagnostics and Analysis

2.4.1 Labrador Sea Water Thickness

Labrador Sea water thickness (Z_{LSW}) is defined as the depth of the Labrador Sea water mass (LSWM,51^{o}N-65^{o}N, 65^{o}W-45^{o}W; Yeager, 2020), based on the surface water mass formation (WMF) analysis. Langehaug et al. (2012) derived an equation for estimating annual water mass transformation (WMT) between two density surfaces σ and $\sigma + \Delta\sigma$,

$$F_i(\sigma) = \frac{1}{N_T \Delta\sigma} \sum_{n=1}^{N_T} D_{n,i} dA_i \quad , \tag{5}$$

where F_i represent the WMT at grid i, $N_T = 12$ is the number of months in a year, $D_{n,i}$ is the surface density flux (unit: kg/m^2/s) in month n and at grid i, and A_i is the area at grid i. Thus, WMF is defined as $F_i(\sigma) - F_i(\sigma + \Delta\sigma)$. The upper and lower boundaries of the LSWM are the depths where WMF are close to zero in LS region.

In CESM2, WMF in LS completely dominates the total WMF in the North Atlantic subpolar region and determines the development of the simulated AMOC in the

deep ocean, underlying the persistence of the deep ocean anomaly associated with AMOC changes which determines the ocean memory at decadal time scales (Yeager, 2020). Therefore, Z_{LSW} is a vital metric to evaluate the potential predictability at decadal time scales. The correlation of Z_{LSW} anomalies between the proposed experiments and FOSI will be used to further analyze the extent to which the various restoring strategies can have an impact on reproducibility of the deep ocean anomalies in FOSI.

2.4.2 Potential Predictability Variance Fraction

Potential predictability variance fraction (PPVF) is defined as the ratio of the signal variance estimated from ensemble mean to the total variance of all ensemble members (e.g., Boer et al., 2013; Yeager, 2020), that is,

$$\text{PPVF} = \sigma_{sig}^2 / \sigma_{tot}^2 \quad \rightarrow 1 \ , \tag{6}$$

where σ_{sig}^2 is the variance from ensemble mean and σ_{tot}^2 is the total variance from individual members. The arrow suggests the upper limitation of this equation. A higher PPVF represents a narrower spread of one variable among ensemble members, indicating the signal is better represented in each individual member with a relatively lower noise.

2.4.3 Drift Adjustment

As mentioned in Chapter 1, initialized predictions suffer from model drifts. These unrealistic trends caused by drifts towards the model climate could offset the anomaly signals and degrade prediction skill. Thus, drift adjustment should be applied before further evaluating the skill of predictions. A simple method of drift adjustment is to treat the drift as a function of lead time (e.g., Boer et al., 2013; Yeager et al., 2018). In

other words, the drift is hypothesized as a constant when the predicted time is fixed. The drift d at a given lead time τ should be:

$$d_\tau = P_{\cdot\cdot\tau} - O_{\cdot\tau} = \frac{1}{M\times Y}\sum_{m=1}^{M}\sum_{y=1}^{Y} P_{my\tau} - \frac{1}{Y}\sum_{y=1}^{Y} O_{y\tau} \quad , \tag{7}$$

where $P_{\cdot\cdot\tau}$ is the predictions averaged by all the ensemble members M and the number of start times Y, and $O_{\cdot\tau}$ is the climatology of the observations averaged by the number of same start times.

The prediction at specific member, start time and lead time after drift adjustment should be:

$$P^{d}_{my\tau} = P_{my\tau} - d_\tau = P_{my\tau} - (P_{\cdot\cdot\tau} - O_{\cdot\tau}) = O_{\cdot\tau} + P'_{my\tau} \quad , \tag{8}$$

where $P'_{my\tau}$ is the prediction anomaly, defined as $P_{my\tau} - P_{\cdot\cdot\tau}$ at the specific member m, start time y and lead time τ.

$$P'_{my\tau} = P^{d}_{my\tau} - O_{\cdot\tau} = P_{my\tau} - (d_\tau + O_{\cdot\tau}) \quad , \tag{9}$$

The prediction anomaly relative to the identically sampled climatology removes the effect of the drift. Similar equation happens to the observations with $d_\tau = 0$. That is,

$$O'_{y\tau} = O_{y\tau} - O_{\cdot\tau} \quad , \tag{10}$$

Thus, the prediction anomaly is feasible to compare to observations instead of the raw data, which largely avoids the impact of model drifts. This drift adjustment will be applied in Chapter 5 to present the preliminary results of decadal predictions.

2.4.4 Hindcast Evaluation Metrics

Following the verification framework outlined by Goddard et al. (2003), three metrics are considered for use in this study to assess the skill of predictions. These are anomaly correlation coefficient (ACC), RMSE, and mean-square skill score (MSSS).

ACC is the correlation coefficient of timeseries from two different datasets after removing the long-term mean climatologies or linear trends or model drifts. In this study, Pearson correlation coefficient is applied, defining

$$\rho(P,O) = \frac{1}{N-1}\sum_{i=1}^{N}\left(\frac{P_i-\mu_P}{\sigma_P}\right)\left(\frac{O_i-\mu_O}{\sigma_O}\right) \quad , \tag{11}$$

where P_i and O_i are the values at the specific time point from two timeseries, *P* and *O*, representing the prediction and observation, respectively. μ_P and μ_O are the mean states from those two timeseries, and σ_P and σ_O are their standard deviation. t-test is used to estimate significant intervals for ACC after Fisher's Z transformation. ACC difference (ΔACC) is the difference between two simulations' ACC skills which are each associated with the same dataset. Generally, ΔACC is the ACC difference between objective predictions and reference predictions, and the positive score indicates the higher skill from objective predictions.

ACC measures the relative association between two variables. However, relative magnitude between those two variables could not be assessed using ACC. Instead, RMSE and MSSS are introduced to make up the deficiency, which are defined as

$$RMSE = \sqrt{\frac{\sum_{i=1}^{N}(P_i-O_i)^2}{N}} \quad , \tag{12}$$

$$MSSS = \frac{MSE_{ref} - MSE_{obj}}{MSE_{ref}} = 1 - \frac{MSE_{obj}}{MSE_{ref}} \quad , \tag{13}$$

where P and O still stand for the prediction and observation timeseries, respectively. MSE is the mean-square-error, the squared RMSE. MSE_{obj} is the MSE from objective prediction relative to observations and MSE_{ref} is the MSE from reference prediction which is also relative to observations.

RMSE is a simple metric which directly evaluates the bias of the prediction from the observations. A higher value indicates a lower prediction skill with a farther deviation from the observations. MSSS normalizes the MSE difference between the reference and the objective prediction. Same to the criteria of ΔACC, a higher skill score of MSSS suggests a better performance in the objective prediction.

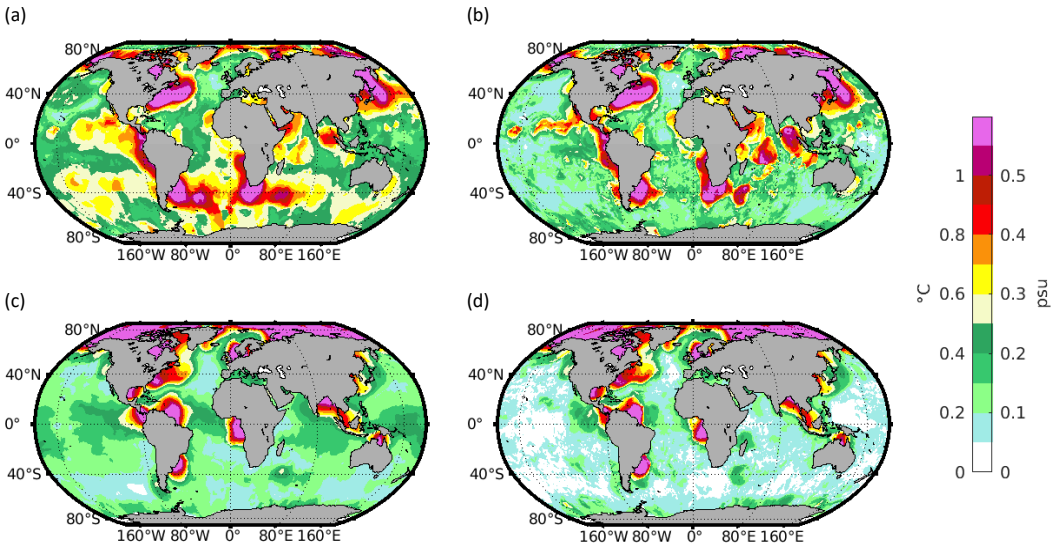

Figure 2.1 EN4.2.1 error standard deviation for (a) SST average of 1960-1969, (b) SST average of 2005-2014, (c) SSS average of 1960-1969, and (d) SSS average of 2005-2014.

CHAPTER III

A COUPLED MODELING STRATEGY TO SIMULATE HISTORICAL DECADAL VARIATIONS OF ATLANTIC MERIDIONAL OVERTURNING CIRCULATION*

3.1 Motivation

As discussed in Chapter 1, AMOC is very important for climate adjustment. Strengthened AMOC leads to convergence of ocean heat transport in SPNA, driving LF temperature anomalies in the North Atlantic (Wills et al., 2019). A realistic simulation of AMOC can potentially lead to skillful decadal predictions. However, how to simulate realistic historical AMOC decadal variations in a fully coupled model is a nontrivial task which requires some careful considerations. One issue to be considered is coupled model biases and their impact on the representation of AMOC. For example, AMOC mean state biases are tightly linked to SSS bias in the North Atlantic (Drews et al., 2015). Kim et al. (2018) compared coupled and atmosphere-only simulations using CESM, and suggested the model might be deficient in representing air-sea coupling that in turn leads to underestimation of the strength of multidecadal NAO, which then results in underestimation of LF AMOC variability. Xu et al. (2019) also pointed out that CGCMs generally simulate a weaker linkage between AMOC and NAO compared to simulated AMOC response to the NAO in FOSI simulations.

FOSI experiments using observation-based atmospheric forcings generally simulate a well-defined decadal variation of AMOC. This well-simulated AMOC decadal variation has motivated the use of FOSI-based initialization for decadal climate prediction. As shown by Yeager et al. (2018), this initialization technique is capable of

* Part of the articles are published in Zhang, Q., Chang, P., Yeager, S. G., Danabasoglu, G., & Zhang, S. (2022). Role of Sea-Surface Salinity in Simulating Historical Decadal Variations of Atlantic Meridional Overturning Circulation in a Coupled Climate Model. *Geophysical Research Letters*, e2021GL096922

producing skillful SST and upper ocean heat content forecasts at decadal time scales in the North Atlantic. However, the hindcast initialization technique, as discussed in section 1.3, endures large ocean initialization shocks and model drifts, and one possible solution may be to reduce the ocean initialization shock introduced by FOSI-based initialization.

It has been shown in seasonal climate prediction studies that the initialization shock problem can be alleviated by restoring SST or wind stress towards observations in a coupled prediction model during the initialization procedure, leading to improvements in seasonal prediction skill (e.g., Chen et al. 1995; Zhu et al., 2017; Tang et al., 2018; Wang et al., 2019). Keenlyside et al., (2008) attempted to extend this SST-restoring technique to decadal predictions. Because the atmospheric forcing is generated by the coupled system, rather than taken from an independent, observation-based data set as in FOSI simulation, the inconsistency in atmospheric forcing, and thus the initialization shock are much reduced. In this chapter, we will further extend the use of this restoring technique in fully coupled climate models by using not only SST restoring but also SSS restoring. As discussed previously, SSS is an important variable for simulating AMOC variability because of its strong influence on surface density in SPNA and LS regions (e.g., Swingedouw et al. 2013; Park et al., 2016; Ortega et al., 2017). However, compared to SST, SSS is less well observed (see Chapter 2 discussion on EN4.2.1 dataset), and observed AMOC record is too short to be used for the AMOC-decadal-variation study. Therefore, in order to fully evaluate the impact of both SST- and SSS-restoring on simulating AMOC decadal variations, a careful experimental design is

required. In the following section, we discuss a modeling framework developed to test effectiveness of SST- and SSS-restoring on simulating AMOC decadal variation in a fully coupled CESM simulation.

3.2 Experiment Design

To address the shortness of observed AMOC records, and less reliable SSS observations, we design a model-based framework to test the hypothesis that restoring SST and SSS in a fully coupled model can lead to historical AMOC simulation. In this framework, we assume ocean model is perfect, and thus FOSI simulation can present observed temperature and salinity, as well as AMOC decadal variations. In other words, we are treating FOSI simulation as "observation" and using it to validate our SST- and SSS-restoring coupled model simulations. Specifically, we will use the fifth cycle of CESM-ocean FOSI simulation for model validation.

The SST- and SSS-restoring simulations will be based on the same CESM, where monthly mean SST and SSS from the fifth cycle of FOSI are used as restoring target files for an ensemble of 6 coupled CESM2 simulations (hereafter referred to as REST). The restoring time scale of REST is 10 m over 10 days from January 1, 1958 to December 31, 2014. Each ensemble member is initialized from the start of the fifth cycle of the FOSI simulation and integrated for the same period as one FOSI cycle, i.e., from 1958 to 2014 with the historical climate forcing. The atmosphere, land, and runoff restart files of REST are from one CESM2 historical simulation, and ensemble members are generated by applying round-off perturbations to the initial atmospheric temperature field. No restoring is applied in regions covered by sea ice in REST. In addition to

validate REST against FOSI, we also compare REST and the ensemble of CESM2 HIST for the same period. 5-year running mean is applied for LF analysis.

3.3 Results

Figures 3.1a-c present a comparison of the mean AMOC among FOSI, REST, and HIST in density-latitude space which focuses on the water formation and transformation in the high latitudes, referred to as AMOC(σ_2), as discussed in Chapter 1. σ_2 indicates the density relative to the pressure at the depth of 2000 m. REST successfully reproduces AMOC(σ_2) spatial structure and the mean transport of FOSI. REST maximum transport (21.7 Sv) is only slightly larger than in FOSI (20.8 Sv). In contrast, HIST shows the strongest transport with 26.8 Sv. In general, the high detrended LF standard deviations (STDs) fall into two regions in all simulations: one in the lighter water class representing the upper limb and the other in the denser water class representing the lower limb where the southward denser currents carry the long-lasting predictive memory (Yeager, 2020; Yeager et al. 2021). The location and magnitude of the lower limb STD in REST are similar to those in FOSI, both occurring in a denser water class (>36.875σ_2) than in HIST (>36.775σ_2). Unlike in HIST where decadal variance only contributes to 27.23% of the total variance in the lower limb between 45°N and 60°N, the decadal variance contribution in FOSI and REST reaches 81.24% and 86.95%, respectively (decadal variance contribution is defined as LF variance divided by the total variance). The good agreement between REST and FOSI suggests that by constraining only the surface density variations through SST and SSS restoring, we can indeed reproduce overall AMOC(σ_2) structure and its decadal variability. We

note that AMOC(σ_2) in REST does not suffer from any structural distortions and remains similar to those in FOSI and HIST, unlike in three-dimensional ocean data assimilation products where the vertical inconsistency in the mean AMOC structure is reported (e.g., Karspeck et al., 2017; Lu et al., 2020).

The temporal variation of AMOC in these simulations is shown in Figure 3.1d where AMOC indices, defined as anomalies of the maximum annual-mean AMOC(σ_2) transport at 45°N, are compared. Consistent with Danabasoglu et al. (2016), the AMOC index in FOSI presents an "inverse U" shape with a peak in the mid-1990s. This decadal variation is unlikely a result of the external climate forcings, but more likely caused by internal dynamics of the coupled climate system, because the AMOC index in HIST shows a different temporal variation – a slight increase from 1975 to mid-1980s followed by a steep decreasing trend. In contrast, the AMOC index in REST clearly reveals a decadal variation that bears a close resemblance to that in FOSI with a very similar amplitude, indicating that with both SST and SSS restoring the coupled model is capable of replicating decadal variations in AMOC(σ_2). The small ensemble spread of the AMOC index in REST indicates a weak within-ensemble-variability and a consistency among the ensemble members in simulating AMOC decadal variations. In contrast, the ensemble spread of the AMOC index is considerably larger in HIST than in REST. This is true even if the ensemble size of HIST is randomly decreased to the same size of REST (not shown). These results suggest the signal-to-noise ratio (the ensemble mean divided by STD of the inter-ensemble spread) of AMOC decadal variations is

significantly amplified by the strong SST and SSS restoring, from 24.12 in HIST to 26.13 in REST with the same ensemble size.

Figure 3.2 further demonstrates the successful replication of FOSI AMOC(σ_2) decadal variability from REST in the whole North Atlantic basin. ACC skill score between FOSI and REST could reach 0.8 in both upper and lower limbs north of 45°N and the lower limb, holding the high score, could extend to the equator, whereas, positive ACC skill score between FOSI and HIST only constrains in the high latitudes. The score south of 45°N is close to zero. It suggests that LF historical AMOC variability in REST is well-represented, particularly in the denser regions. Figure 3.2c shows the improved skill of representing AMOC(σ_2) decadal variability in REST by only restoring SST and SSS compared to HIST. The positive values are almost filled in the whole ΔACC map.

To further validate whether the decadal AMOC variation in REST is consistent with the mechanism proposed by Yeager (2020) emphasizing the importance of AMOC lower limb in decadal prediction, we examine the LF co-evolution of AMOC(σ_2) and sea surface height (SSH). Yeager (2020) suggested the deep flow associated with decadal AMOC variations can induce an SSH response which is critical in sustaining decadal prediction skill. Here, the phase evolutions of AMOC(σ_2) and SSH are firstly compared among FOSI, REST, and HIST (Figure 3.3 & Figurer 3.4), followed by their LF variability relation between these two variables shown in Figure 3.6.

Figure 3.3 shows decadal phases of AMOC(σ_2) from 1975 to 2014. The upper and lower limbs in FOSI exhibit the different phase evolutions led by different driven

factors. The upper limb, which is largely impacted by external forcings, show an increasing trend, consistent to the global warming signal. The lower limb related to dense water, dominated by buoyancy forcings, show the "inverse U" pattern. Both REST and HIST replicate the increasing trend of FOSI in the upper limb because these three simulations share the same external forcings. However, the phases in the lower limb of REST and HIST in period 1975-1984, and period 1995-2004 are completely opposite. The lower limb phase in REST follows the "inverse U" pattern. In contrast, the one in HIST only shows a decreasing trend. Similar results happen to SSH decadal phase evolution (Figure 3.4). Based on the FOSI LF STD of SSH in the North Atlantic (Figure 3.5), the dominant variations locate in the western SPNA where LF AMOC variability originates, and the boundary of SPNA and subtropical gyre. The SSH phases in these regions show a "positive-negative-negative-positive", that is, "U" pattern in both FOSI and REST, while, an increasing pattern in HIST. Thus, the separated phase evolutions for AMOC(σ_2) and SSH suggest that REST follows the decadal variations of FOSI not only in AMOC (particularly the lower limbs), but SSH as well , totally different to HIST.

Figure 3.6 verifies the response relation between dense AMOC(σ_2) and SSH. The selected AMOC(σ_2) and SSH anomalies in time and latitude are the locations where LF dominates. In both FOSI and REST, maximum positive anomalies of lower limb AMOC(σ_2) appear between 1985 and 1995, ahead of the peak of AMOC index at 45°N, indicating that the source of the decadal variations originates from the dense water anomalies in LS. In contrast, AMOC(σ_2) variations in HIST show a dominant decreasing

trend with little indication of decadal variations. The zonal-averaged SSH anomalies in western SPNA (40°W-55°W) in FOSI and REST show a similar evolution pattern, both displaying a delayed response to the change in the AMOC(σ_2) lower limb, suggesting that in both FOSI and REST the deep circulation changes are driving the upper ocean circulation changes as reasoned by Yeager (2020). The magnitude of the decadal variations in REST is, however, smaller than that in FOSI, likely due to the ensemble average in REST. In comparison, no such delayed response in SSH is found in HIST. These results confirm the similarity between FOSI and REST in simulating AMOC and its variability, specially the lower limb of AMOC(σ_2) and subpolar gyre decadal variations, which are distinctively different from HIST.

Observations reveal a similar but opposite sign of decadal variation in temperature and salinity in the deep ocean of SPNA to that in the upper ocean (Polyakov et al., 2005). This vertical structure of the decadal variation is consistent with a downward propagation of temperature and salinity anomalies as shown in EN4.2.1. Both FOSI and REST capture the vertical propagation to a depth range of ~2000 m, consistent with EN4.2.1 (Figure 3.7). HIST is able to simulate some vertical decadal propagation, but the depth of the vertical propagation is shallower and the phase of the propagating signal is not in line with those in FOSI and REST. It suggests the SST and SSS restoring strategy enables the fully coupled model to simulate the observed SPNA decadal variations down to at least 2000 m depth.

Labrador Sea Water thickness (Z_{LSW}) is considered as a critical factor for understanding AMOC's role in decadal prediction because it represents an important

deep ocean memory in the North Atlantic (Yeager, 2020). The ACC of Z_{LSW} between FOSI and REST (Figure 3.8a) shows this deep ocean memory in FOSI is well represented by REST. High correlation values of above 0.9 exist in the eastern and western flanks of the mid-Atlantic ridge (MAR), where deep water mass information accumulates and persists (Yeager, 2020). However, the positive ACC of Z_{LSW} between FOSI and HIST only exists in SPNA and the decadal variation in HIST fails to propagate to the MAR (Figure 3.8b). PPVF is calculated for REST and HIST in order to estimate the potential predictable variance in the REST and HIST ensemble, respectively (Figure 3.8c&d). They show the ensemble mean of Z_{LSW} anomalies (ΔZ_{LSW}) in REST represents over 60% of the total variance in all ensemble members in the northern North Atlantic and reaches 90% or higher in much of the region south of 45°N, while PPVF in HIST is slightly higher than that in REST only in the western SPNA because of the consistent decreasing trends among all HIST ensemble members, and reach the highest in the western MAR where the correlations are not statistically significant.

Finally, we examine replicability of global upper 295-m averaged ocean temperature (T295m) in REST and HIST compared to FOSI, and the wind stress differences in FOSI and REST compared to HIST (Figure 3.9). T295m is critical for skillful decadal prediction in the North Atlantic and other regions (Yeager et al., 2018). The LF T295m ACC between EN4.2.1 and FOSI, REST, and HIST, respectively, are shown in Figure 3.9a-c after removing linear trends. Both FOSI and REST reproduce the observed T295m variability in SPNA. FOSI does a better in the subtropical regions but REST has higher ACC values in the tropical North Atlantic (Figure 3.9d). Outside of the

North Atlantic, FOSI and REST show similar distributions of high ACC in much of the Pacific and Indian Oceans. Overall ACC values are nevertheless slightly higher in FOSI than in REST, the horizontal average of which is 0.56 ± 0.28 in FOSI and 0.52 ± 0.27 in REST between 65°S and 65°N, particularly in the tropical eastern Pacific where ENSO related variance dominates. For example, ACC in the Niño3 region is 0.88 ± 0.06 in FOSI and 0.82 ± 0.06 in REST. This is expected because FOSI is forced by the observed atmospheric forcing, whereas in REST the ocean is forced by the simulated atmospheric forcing in CESM2 with SST restored to the FOSI SST. Given this difference, it is remarkable REST can reproduce so well the observed T295m variability over wide areas of the global ocean, which is a significant improvement over HIST (Figure 3.9b&c). In addition, the mean atmospheric wind forcing in REST remains close to that in HIST. The difference of mean wind stresses between FOSI and HIST and between REST and HIST are shown in Figure 3.9e&f, respectively. The large differences in the Southern Ocean and SPNA between FOSI and HIST are largely reduced between REST and HIST, and the tropical wind forcing in REST is also closer to that of HIST compared to the observations used in FOSI. The global RMSE of wind stresses is 0.0143 N/m^2 between FOSI and HIST and reduces to 0.0058 N/m^2 between REST and HIST. In the tropical Pacific (5°S-5°N, 150°E-80°W), the averaged wind stress RMSE decreases from 0.0070 N/m^2 between FOSI and HIST to 0.0037 N/m^2 between REST and HIST. These results suggest that the imbalance between atmospheric forcing and ocean state could be reduced and higher prediction skill would be obtained if decadal predictions were

initialized from REST. Verifying this claim, however, requires carrying out ensembles of decadal prediction runs.

3.4 Conclusion and Discussion

In this chapter, we introduce and evaluate a modeling strategy for realistically simulating AMOC and related decadal ocean variability in a fully coupled climate model within a framework where FOSI is regarded as "observation" or "truth". By conducting an ensemble of 6 coupled CESM2 simulations, referred to as REST, where SST and SSS are restored to the monthly-mean FOSI-simulated SST and SSS. We assess the skill of REST to replicate AMOC and associated deep ocean decadal variations in SPNA of FOSI that are shown to be critical for decadal climate predictions. The major findings of our study are summarized as follows:

1) AMOC structure and its transport, as well as LF STD, are well reproduced in REST,
2) REST not only realistically reproduces the decadal variation of AMOC and the associated upper ocean circulation changes in FOSI, but also faithfully replicates AMOC-related decadal variations in the deep ocean, particularly the Labrador Sea Water thickness anomalies that have been shown to be critical for decadal predictions,
3) REST also realistically simulates global upper ocean heat content variability with ACC skills comparable to those in FOSI,

4) REST produces an atmospheric forcing whose mean state is more consistent with that of HIST compared to the mean atmospheric forcing between JRA-55 used in FOSI and HIST.

These findings open a perspective for the potential use of this coupled model strategy as an alternative to FOSI or full-depth ocean data assimilation for initializing decadal predictions. Compared to the FOSI initialization used by Yeager et al. (2018), this modeling strategy has the potential to reduce ocean initialization shock, because the mean atmospheric forcing to the ocean model is much closer to that in the coupled model used for prediction (e.g., Figure 1.2; Figure 3.9 e&f). This should reduce the imbalance between atmospheric forcing and ocean state at the initial stage of prediction simulations. Compared to full-depth ocean data assimilation, this modeling strategy does not suffer from the problem of inconsistent vertical structure of ocean states due to the lack of sufficient ocean observations below 2000 m (Karspeck et al. 2017). However, whether this modeling strategy can lead to an actual skill improvement in decadal climate prediction remains to be seen. Some preliminary prediction results will be presented in Chapter 5.

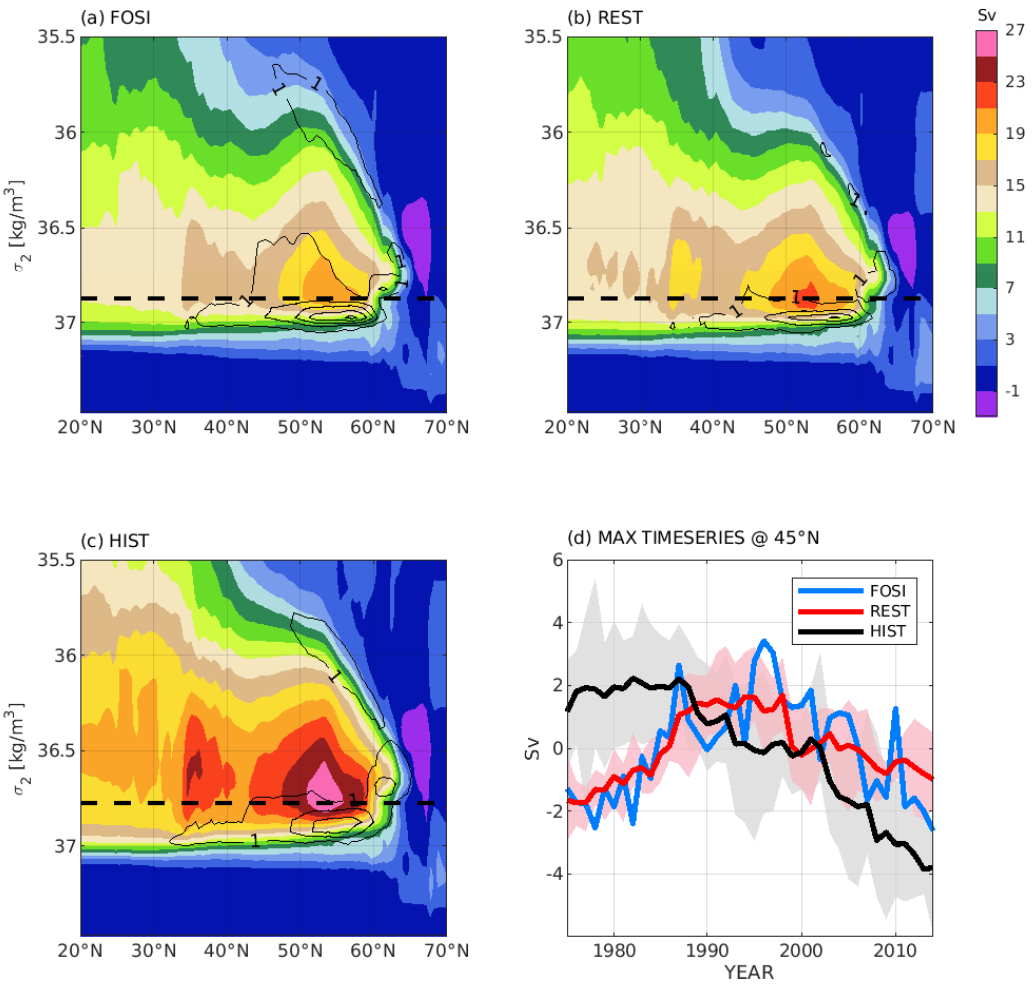

Figure 3.1 Time mean AMOC(σ_2) (color fill) and linearly detrended 5-year running mean (LF) standard deviation (STD, contoured at 1 Sv interval) in (a) FOSI, (b) REST, and (c) HIST. The black dashed line at (a) 36.875σ_2, (b) 36.875σ_2, and (c) 36.775σ_2 indicates the density surface where the maximum AMOC transport locates, separating the upper and lower limb of AMOC(σ_2). AMOC index (maximum transport anomaly at 45°N) time series for the 1975-2014 period from FOSI (blue), ensemble mean of REST (red), and ensemble mean of HIST (black) are shown in (d). Pink and grey shadings indicate the range of respective ensemble spreads in REST and HIST, respectively. The STDs in (b) and (c) are the average of individual members. The anomalies in (d) are with respect to the 1975-2014 period. (unit: Sv; 1 Sv = 10^6 m^3/s)

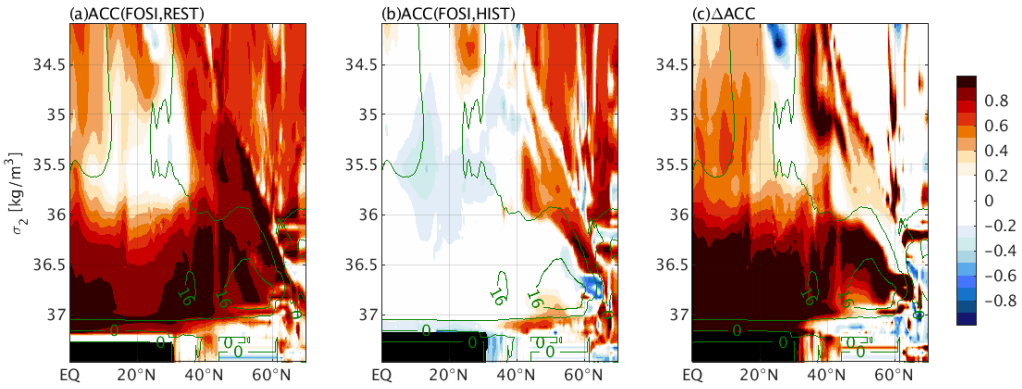

Figure 3.2 Anomaly Correlation Coefficients (ACC) of 5-year running mean (LF) AMOC(σ_2) between (a) FOSI and REST, and (b) FOSI and HIST, (c) ACC differences (ΔACC) between (a) and (b). The green contours are the mean state of FOSI AMOC(σ_2, contoured at 8 Sv interval). Regions where ACC is not significant at the 95% level are shown as white.

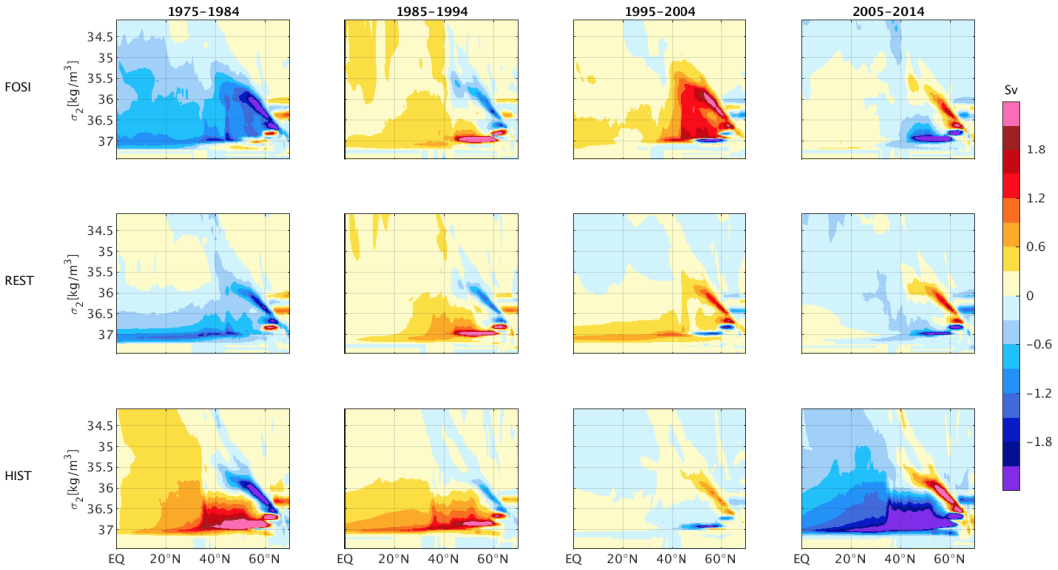

Figure 3.3 AMOC(σ_2) decadal anomalies in FOSI (upper), REST (middle), and HIST (lower). The four columns from left to right are the 10-year-time-average anomalies of 1975-1984, 1985-1994, 1995-2004, and 2005-2014, which are with respect to the 1975-2014 period.

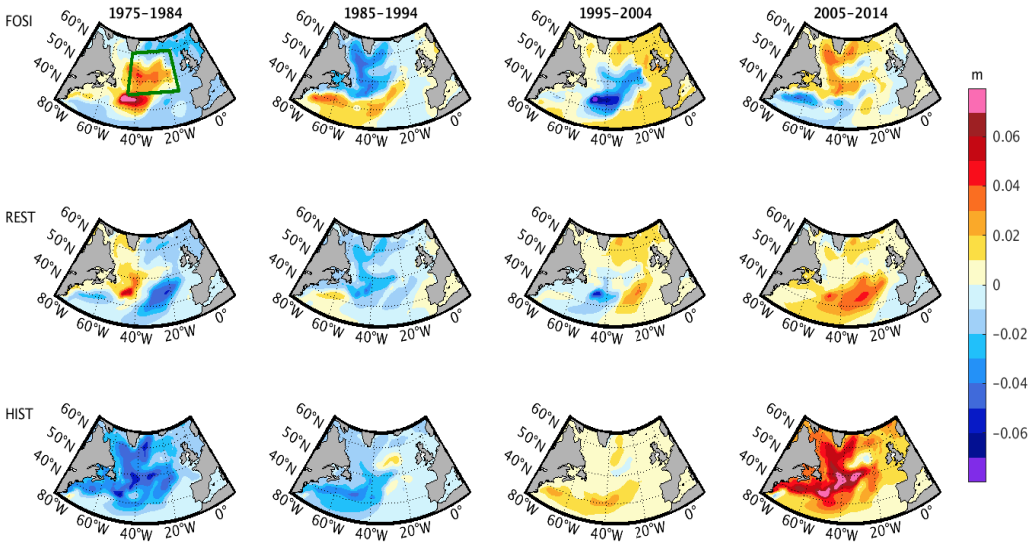

Figure 3.4 The same with Figure 3.3, except for SSH. The green box in the first panel is the region (45°-60°N,15°-45°W) defined as SPNA where Figure 3.8 refers.

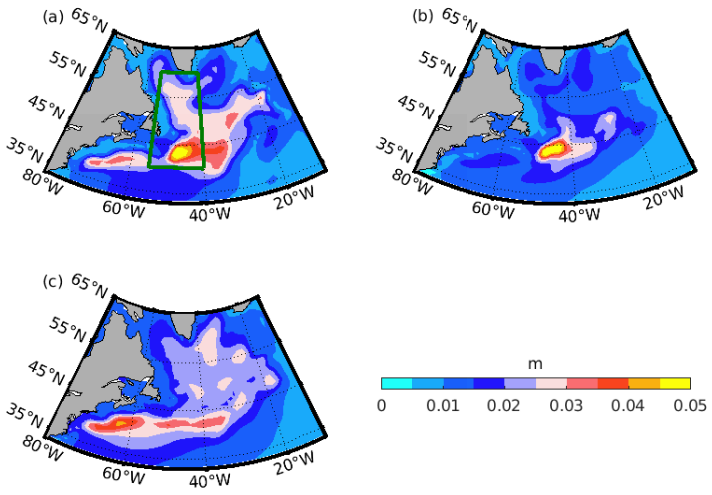

Figure 3.5 Sea surface height (SSH) LF STD after removing its linear trend. REST and HIST are the averaged STD from each member's STD. The green line indicate zonal-averaged region (40°W-55°W, 40°N-60°N) where Figure 3.6 refers.

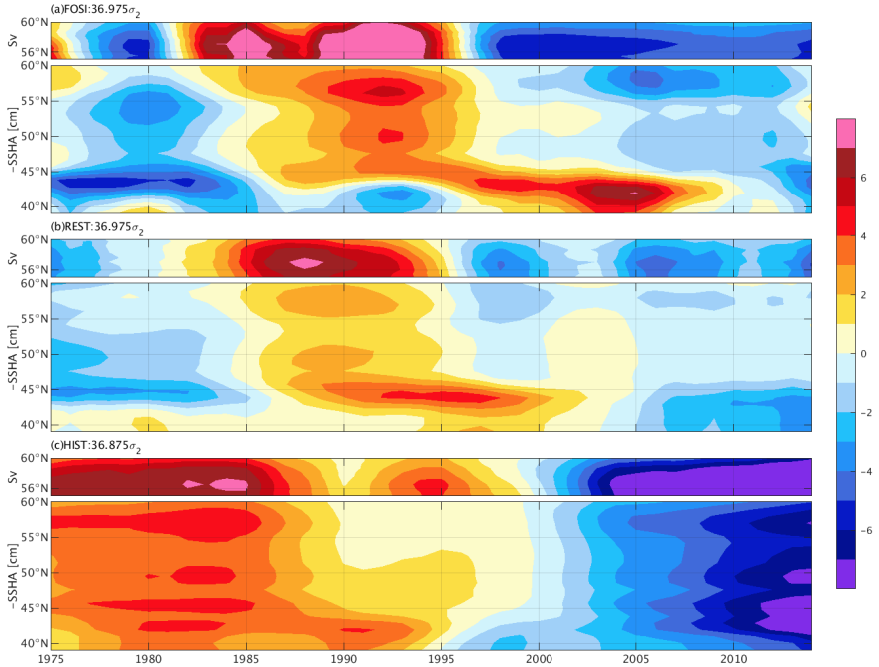

Figure 3.6 LF AMOC(σ_2) anomalies along dense density surfaces in the deep ocean (upper, unit: Sv) and LF negative zonal-averaged SSH anomalies between 40°W and 55°W (bottom, unit: cm) in (a) FOSI, (b) ensemble mean of REST, and (c) ensemble mean of HIST. The dense density surface in each simulation corresponds to the maximum LF STD of AMOC(σ_2).

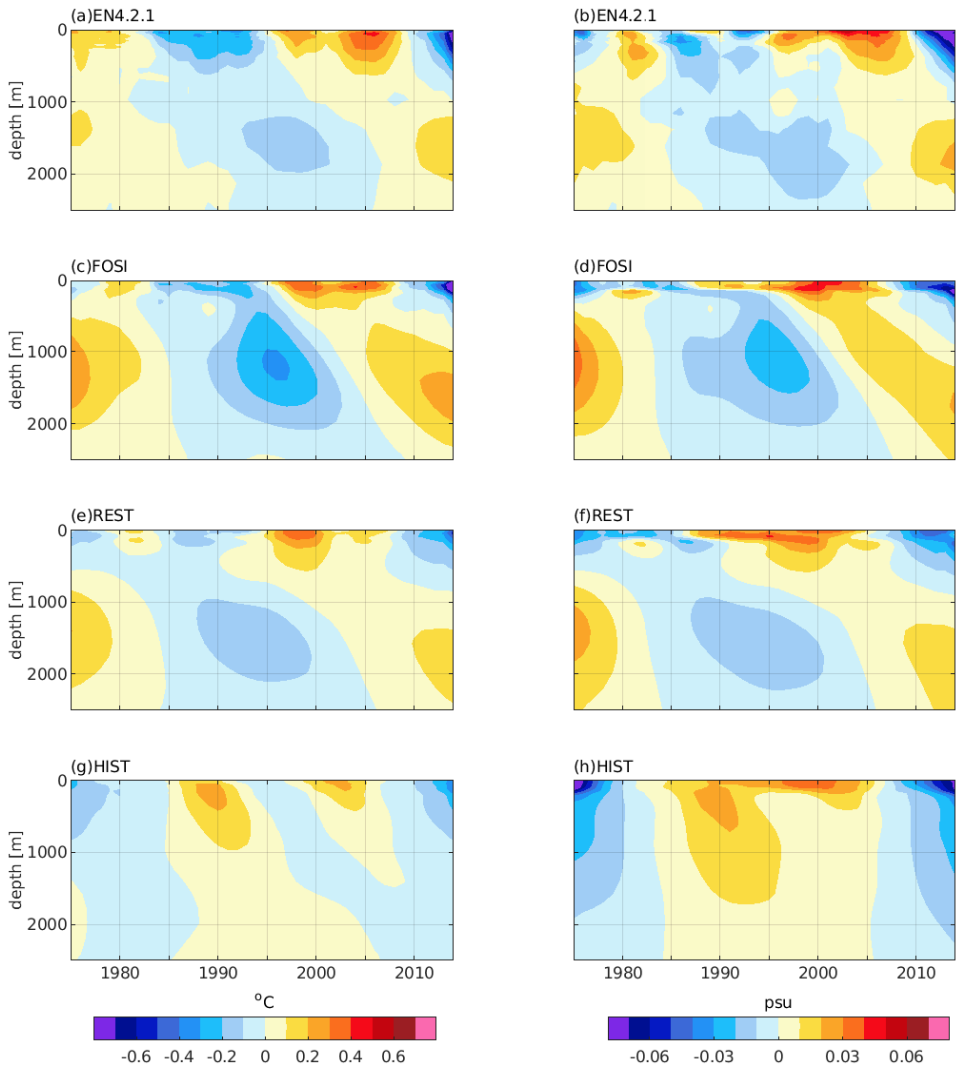

Figure 3.7 LF, area-averaged, linearly detrended (left) potential temperature (unit: °C) and (right) salinity (unit: psu) anomalies as a function of depth and time in (a, b) EN4.2.1, (c, d) FOSI, (e, f) ensemble mean of REST, and (g, h) ensemble mean of HIST. The area-average is computed over the North Atlantic region (45°-60°N,15°-45°W) shown in first panel of Figure 3.4. 0-2500 m depth range is shown in all the panels.

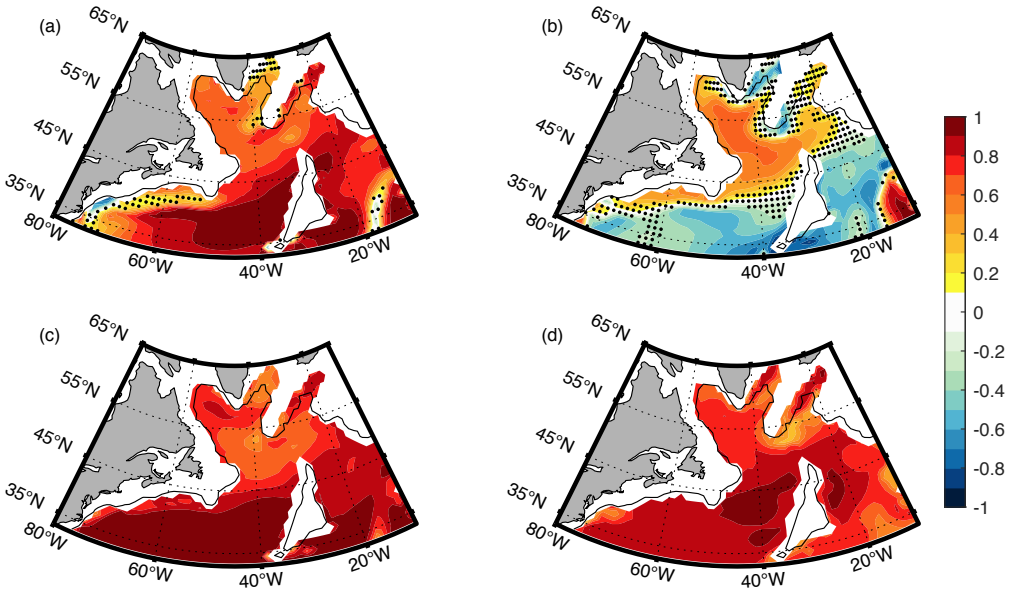

Figure 3.8 ACC of LF Labrador Sea Water thickness (Z_{LSW}) between FOSI and (a) ensemble mean of REST, and (b) ensemble mean of HIST. Dots indicate regions where correlation is not significant at 95% level. The square root of the potential predictable variance fraction (PPVF) of Z_{LSW} anomalies (ΔZ_{LSW}) in (c) REST and (d) HIST. The black contours in (a-d) show the 3000-m isobath.

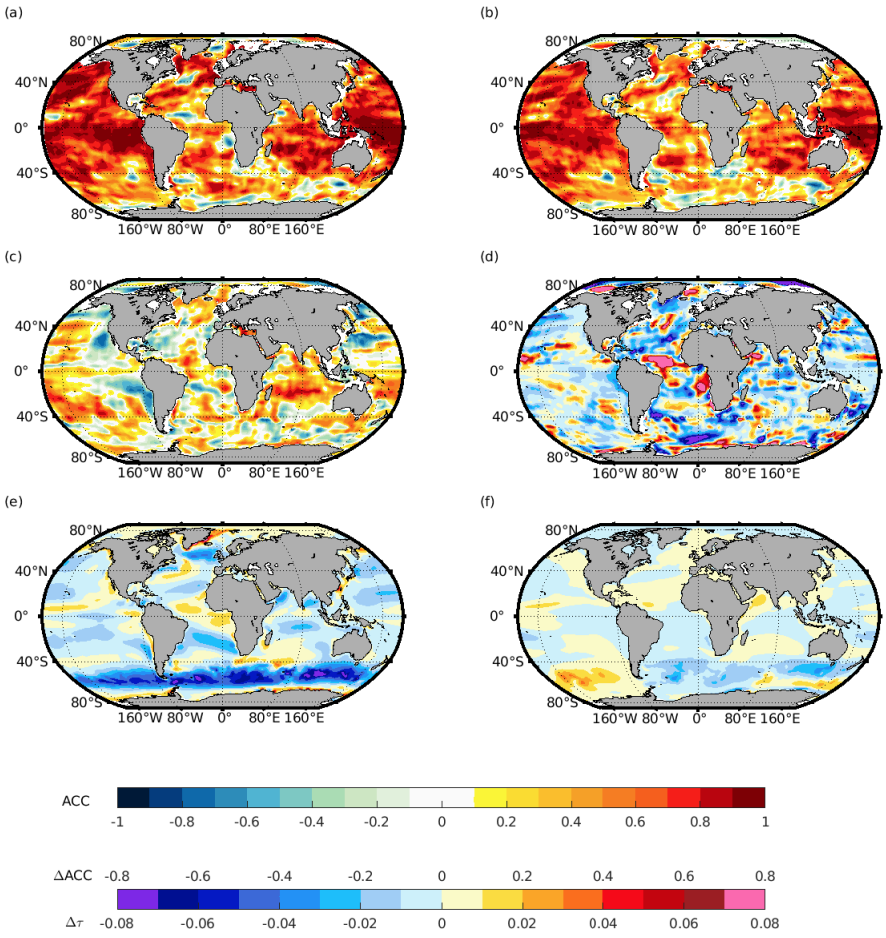

Figure 3.9 ACC of LF, linearly detrended T295m between EN4.2.1 and (a) FOSI, (b) ensemble mean of REST, and (c) ensemble mean of HIST. (d) ΔACC between REST and FOSI (REST minus FOSI). Wind stress differences ($\Delta\tau$, unit: N/m^2) (e) between FOSI and HIST (FOSI minus HIST), and (f) between REST and HIST (REST minus HIST). Regions where ACC is not significant at the 95% level are shown as white.

CHAPTER IV

SENSITIVITY EXPERIMENTS OF SURFACE RESTORING TECHNIQUES

4.1 Motivation

It is worth emphasizing that SSS restoring is essential in REST to replicate the AMOC decadal variability in FOSI simulation, because SSS can influence near-surface density in SPNA, which is critical for the deep convection in the high latitudes of North Atlantic. However, SSS changes in SPNA can be induced by local or remote influences. The local influence primarily comes from NAO-related atmospheric variability while the remote influence can come from the tropics. For example, changes in tropical precipitation can lead to the redistribution of freshwater in the tropical Atlantic, which then can propagate to SPNA along the Gulf Stream and North Atlantic Current, modifying SSS in the deep convection region and causing changes in AMOC and AMV (Latif et al., 2000; Mignot & Frankigonoul, 2005). If this tropical remote influence outweighs the local influence, then by assimilating only SST into coupled climate models we should be able to capture the decadal variation of AMOC and AMV.

Indeed, several modeling studies have suggested that SST-only assimilation can simulate realistic decadal variations of AMOC. For example, Counillon et al. (2016) assimilated observed SST, using an Ensemble Kalman Filter method, to an isopycnal coordinate ocean model within the Norwegian Climate Prediction Model and showed a comparable AMOC decadal variation to that in FOSI. However, we should note that since they used an isopycnal coordinate ocean model, their assimilation scheme used a conjugate adjustment of salinity, which can affect salinity in the model. In other words,

even though no salinity data is directly assimilated into their model, there was a salinity adjustment introduced to the model to compensate for surface density changes due to assimilating SST. Keenlyside et al. (2008) ran strongly (4 days) restored-SST simulations between 30°S-30°N with buffer zones to 60°S and 60°N in the Southern and Northern Hemisphere, respectively, using the ECHAM5/MPI-OM model and showed an improved surface temperature hindcast skill in parts of the North Atlantic. However, SST in LS and western North Atlantic where salinity plays an important role in forming the North Atlantic Deep Water remained at a relatively low level. This is in sharp contrast to the results from CESM DPLE that show highest SST forecast skill in the SPNA, hinting the importance of local forcing in the North Atlantic. Dunstone & Smith (2010) showed that the positive results in Keenlyside et al. (2008) were unable to reproduce, suggesting that the improvement of decadal prediction skill by restoring strong SST may be model-dependent.

Nevertheless, the question of how important SSS is for a realistic simulation of AMOC decadal variation in a fully coupled climate model is still open. The focus of this Chapter is on addressing this question. Specifically, we will conduct an extensive set of CESM sensitivity experiments to examine the following questions: Is SSS-restoring in the coupled CESM simulation critical to reproduce AMOC decadal variation in FOSI? If so, which component of SSS, climatology or anomalies, or both, are more important for a realistic simulation of AMOC decadal variation? Can AMOC decadal variation be simulated by restoring model SSS to observed SSS instead of FOSI SSS? Given the

large uncertainty in the observed SSS dataset as discussed in Chapter 2, can we use observed SSS climatology as a restoring target to simulate AMOC decadal variation?

In the following, we first introduce all the sensitivity experiments conducted in this study in Section 4.2 and then present their results in Section 4.3. Conclusions and discussions of the results are presented in Section 4.4.

4.2 Sensitivity Experiment Design

We conducted 6 sets of experiments to address the scientific questions listed above. As in REST, all the simulations are based on CESM2 and each set contains an ensemble of 6 simulations. The differences among different sets lie in the treatment of restoring term in the model. We give a brief summary of each experiment and its purpose in the following. A complete list of sensitivity experiments is shown in Table1.

Strong SSS-restoring (*S-SSS*): This ensemble and its companion ensemble *weak SSS-restoring* described below are designed to test model AMOC simulation sensitivity to SSS restoring time scale. In this experiment the modeled SST is restored to the observed monthly mean SST from ERSSTv5 with a restoring time scale of 10 days over upper 10 m, while SSS is restored to the observed monthly mean SSS climatology from WOA13v2 with the same 10-day restoring time scale over upper 10 m. By comparing the results of this experiment to those of REST, we can also learn whether realistic AMOC decadal variation can be simulated by using observed SST and observed SSS climatology, instead of monthly mean SST and SSS from FOSI.

Weak SSS-restoring (*W-SSS*): This is the companion experiment to the above *S-SSS*. It is identical to *S-SSS* except that the SSS restoring time scale is changed to 365

days from 10 days in *S-SSS*. Together with *S-SSS* this experiment is designed to evaluate the impact of SSS restoring on simulating AMOC decadal variation.

Monthly-Mean SSS-restoring (*M-SSS*): This ensemble is similar to REST except that observed monthly-mean SST from ERSSTv5, instead of FOSI SST, is used as the restoring SST target. Therefore, this experiment can be used to test the effect of observed *vs.* FOSI SST on AMOC simulation with the mismatched monthly-mean FOSI SSS. When compared to its companion ensemble *Climatological SSS-restoring* described below, this experiment can also be used to examine the impact of restoring to monthly-mean SSS *vs.* climatological SSS on AMOC decadal variation.

Climatological SSS-restoring (*C-SSS*): This ensemble is the same as *M-SSS* except that the simulated SSS in CESM2 is restored to the climatology of monthly-mean SSS derived from FOSI. A comparison between *M-SSS* and *C-SSS* can help address the importance of including SSS anomalies in the restoring simulations.

Anomaly-restoring (*A-RES*): In this ensemble, the CESM2 simulated SST and SSS are restored to a reconstructed monthly-mean SST and SSS datasets that consist of the anomalies derived from FOSI and climatologies derived from CESM2 HIST. In the framework of REST where we assume FOSI SST and SSS as "*observations*", this experiment only "assimilates *observed*" SST and SSS anomalies into the coupled system. Therefore, its purpose is to test whether SST and SSS anomalies are determining factors for simulating realistic AMOC decadal variation.

4.3 Results

4.3.1 Impact of Strong vs. Weak SSS Restoring

We first compare the results of *S-SSS* to those of REST, which have been demonstrated to be skillful in replicating historical AMOC decadal variability in Chapter 3. The differences between *S-SSS* and REST are in the former 1) the SST is strongly restored to monthly-mean ERSSTv5 instead of FOSI monthly-mean SST and 2) the SSS is strongly restored to observed monthly climatological SSS from WOA13v2 dataset instead of FOSI monthly-mean SSS in the latter. The mean state differences between FOSI SST and ERSSTv5 are small in low- and mid-latitudes (Figure 4.1a), because in FOSI the model SST is strongly constrained by the observed surface air temperature that is closely related to the observed SST. The main differences come from the Southern Ocean and the SPNA. The global-averaged FOSI SST RMSE between 65°S-65°N compared to ERSSTv5 is 0.47°C. However, the annual-mean correlation coefficients between FOSI SST and ERSSTv5 are higher than 0.8 in most regions including the eastern SPNA (Figure 4.1c). The western SPNA is somewhat lower with a value of ~0.6. The global-averaged correlation between 65°S-65°N reaches 0.83±0.31. Therefore, we do not expect that restoring to ERSSTv5 SST in *S-SSS* can cause a major difference in the simulation results between REST and *S-SSS*, although the simulated SST and upper ocean heat content in *S-SSS* should be closer to observations in *S-SSS* than those in REST. The impact of changing the SSS restoring target to the observed SSS climatology in *S-SSS* from FOSI SSS in REST can be potentially large, because the FOSI simulation is nudged to observed climatological freshwater flux at 1-year restoring timescale. The

global FOSI SSS RMSE between 65°S-65°N is 0.28 psu compared to WOA13v2 SSS. Figure 4.1b reveals significant FOSI SSS saline biases compared to the observation in most regions, but fresh biases only exist in SPNA. This raises an interesting question: Can the AMOC decadal variation still be replicated by SSS restoring using observed SSS climatology as restoring target?

We examine this question by comparing AMOC(z) streamfunction transport, phase propagations of denser LSW and SSH, and ΔZ_{LSW} in *S-SSS*, FOSI and REST. As shown in Figure 4.2, *S-SSS* shows a high fidelity in replicating the AMOC decadal variation in FOSI and REST. The detrended AMOC maximum transport time series in *S-SSS* tracks closely with that in FOSI and REST (Figure 4.2a). The correlation between LF detrended AMOC overturning streamfunctions in *S-SSS* and FOSI is above 0.7 in much of the region where AMOC is strong and exceeds 0.9 in the maximum AMOC cell (Figure 4.2b), similar to the correlation patterns between FOSI and REST (not shown). The maximum decadal variations of AMOC(σ_2) is along 36.925σ_2, lighter than the density in both FOSI and REST (Figure 3.6), but still in the lower limb region (denser than 36.775σ_2, not shown). The phase pattern of LF detrended dense AMOC in *S-SSS* is comparable to the pattern in FOSI and REST with the peak value ahead of the year 1995 (Figure 4.2c & Figure 4.3). The maximum value occurs in early 1990s in *S-SSS*, even more consistent with that in FOSI (early 1990s) compared to REST (late 1980s). The decadal variations of LF detrended SSH in *S-SSS* (lower panel in Figure 4.2c), similar to FOSI and REST (lower panels in Figure 4.3), follows the phase transition of dense AMOC, meridionally propagating from high-latitudes (55°N – 60°N) to mid-latitudes

(~45°N). The phase transition of SSH from the positive to negative in *S-SSS* is also more consistent with that in FOSI and later than that in REST, due to the earlier phase transition of dense AMOC in *S-SSS* and FOSI. Figure 4.2d & e show the ACC of detrended Z_{LSW} between *S-SSS* and FOSI in the North Atlantic and PPVF in *S-SSS*, respectively. ACC of Z_{LSW} reaches 0.8 almost everywhere except the Gulf stream extension and northeastern Atlantic near Africa coast. The value of PPVF is above 0.8 in most regions. Particularly, the deep convection region, eastern and western flanks of MAR can reach above 0.9, suggesting the high potential predictability from dense AMOC decadal signals. Therefore, we conclude that using the observed SSS monthly climatology as restoring target, *S-SSS* can replicate AMOC decadal variation with similar or perhaps higher fidelity than REST.

The fact that replicability of AMOC decadal variation using SST/SSS restoring in coupled CESM2 simulations is independent of using FOSI SST and SSS suggests that the results presented here are not likely model dependent. It also suggests that SSS anomalies may not play an important role in generating surface density anomalies in SPNA that drive AMOC decadal variation. The main role of SSS restoring is to reduce salinity bias in CESM and the surface density anomalies for driving AMOC decadal variations are primarily determined by SST anomalies. We will discuss this issue further in the subsequent subsection.

Having now established the fact that *S-SSS* can replicate AMOC decadal variation with high fidelity, we can assess the importance of SSS restoring in simulating AMOC variability by comparing *S-SSS* to *W-SSS*. As shown in Figure 4.4a, reducing the

SSS-restoring strength in *W-SSS* leads to a shutdown of deep convection in LS. This is partly caused by positive feedback between AMOC weakening and sea-ice growth. Because AMOC transports a significant amount of heat northward into SPNA, a weakening in AMOC can lead to a cooling in SPNA, causing more sea-ice to form. As sea-ice continues to expand, it causes more ice coverage in LS. This will lead to a further reduction in deep convection, and subsequently a further weakening in AMOC. This positive feedback eventually leads to a complete shutdown of deep convection in LS and a collapse of AMOC in *W-SSS*. In contrast, *S-SSS*, where SSS is strongly restored to the observed SSS climatology, can reproduce the sea-ice extent and mixed layer depth in FOSI (Figure 4.4b & c).

As the LS deep convection change in *W-SSS* is dominated by a decreasing trend, the detrended LF mixed-layer depth variance is very weak compared to that in *S-SSS* and FOSI (Figure 4.4d-f). Interestingly, the LF mixed-layer depth variance over the Irminger Sea region in *W-SSS* remains similar to that in *S-SSS*, indicating that the impact of the SSS-restoring is mainly confined to LS. Since AMOC variance in CESM2 is primarily controlled by the variability of LS deep convection, AMOC also experiences a linear decreasing in *W-SSS* (not shown).

In summary, the results from *S-SSS* and *W-SSS* indicate that AMOC decadal variation in REST and *S-SSS* is unlikely forced by remote influence from the tropics, because otherwise we would expect to see a similar AMOC response from *S-SSS* and *W-SSS* as both experiments used the same SST-restoring. The findings also indicate a realistic SSS climatology in SPNA is critical for simulating historical AMOC decadal

variation in a coupled model, but realistic SSS anomalies may be less important for AMOC simulations, at least in the framework of CESM2. In the next subsection, we will further address this issue by comparing *M-SSS* and *C-SSS*.

4.3.2 Role of SSS-climatology vs. SSS-anomaly in SSS-restoring

In this subsection, we first compare *M-SSS* and *C-SSS* to further examine the importance of SSS-climatology and SSS-anomaly in SSS-restoring. Recall that these two experiments are nearly identical except that the model SSS is restored to monthly-mean FOSI SSS in *M-SSS*, whereas it is restored to monthly climatological FOSI SSS in *C-SSS*.

The maximum AMOC(σ_2) streamfunctions are examined in Figure 4.5. The structure of the 40-year mean AMOC in density space is similar. The maximum values in *M-SSS* and *C-SSS* both locate around 55°N at the surface of 36.925σ_2, but are in different strengths. AMOC in *C-SSS* is stronger than the one in *M-SSS* even though the mean state of constrained SST and SSS are the same. The detrended LF STDs of AMOC(σ_2) in SPNA (50°N - 60°N) lower limb region are similar in both *M-SSS* and *C-SSS*, indicating that the surface information in both experiments is able to propagate to the deep ocean in SPNA. Figure 4.5c & d reveal the decadal variations of AMOC maximum values in density space along the latitudes from 20°N to 60°N after removing linear trends from *M-SSS* and *C-SSS*. The historical AMOC decadal variations in both experiments show an "invert U" pattern from high latitudes to low latitudes with a stronger amplitude in *C-SSS*. The timeseries along 45°N are selected as representatives to show more details (Figure 4.5e). It is clear the maximum value of AMOC index in *C-*

SSS occurs at the same time with the one in *M-SSS*, both slightly earlier than FOSI with similar strengths, indicating that the peak value may depend on the monthly-mean SST restoring, rather than the monthly-mean SSS restoring or together. Thus, even with restoring to climatological SSS the model is still capturing the decadal variation of AMOC.

The decadal variations of detrended dense AMOC and zonal-averaged SSH anomalies are analyzed to examine the relationship between AMOC and upper ocean variability in *M-SSS* and *C-SSS* (Figure 4.6). The locations of maximum LF STD of AMOC(σ_2) for both *M-SSS* and *C-SSS* are along the density surface of 37.025σ_2, indicating that the deep structure of AMOC(σ_2) variability is influenced by the mean state of surface density. In addition, both *M-SSS* and *C-SSS* clearly show that zonal-averaged SSH anomalies generated from the high latitudes propagate meridionally to the mid-latitudes. However, it is worth noting that there exists transition time difference between these two experiments. The mid-1990s phase transition in FOSI (Figure 4.3a) is delayed to mid-2000s in *M-SSS* but comparable in *C-SSS*. It is possible explained by the unpaired monthly-mean SST- and SSS-restoring in *M-SSS*, leading to the mismatched phase transition, although the large similarity exists between ERSSTv5 and FOSI SST (Figure 4.1). Instead, the SSS-climatology restoring in *C-SSS*, correcting the surface density mean state and getting rid of the possible uncertainty from surface density anomaly, simulates much closer phase transition to FOSI. It suggests the role of SSS-restoring is to adjust the deep convection through correcting surface density mean state.

The unpaired SST and SSS anomaly restoring may break the historical AMOC decadal variation, degrading the performance of deep ocean.

A-RES, in which model SST and SSS anomalies are restored to monthly FOSI SST and SSS anomalies while keeping the climatological SST and SSS to the same as those in the free-coupled simulations, HIST, is analyzed to further assess the relative importance of climatological SSS vs. SSS anomalies in simulating AMOC decadal variations. SST and SSS anomalies in *A-RES* are corrected to anomalous FOSI's values but the mean SST and SSS states are kept to those in HIST. Therefore, *A-RES* can shed further light on whether it is more important to correct mean SST and SSS bias in the model or keep realistic SST and SSS anomalies to replicate the historical AMOC decadal variation.

Figure 4.7 shows AMOC mean states and the corresponding decadal variations in REST and *A-RES*. Although the mean state of SST and SSS in *A-RES* is restored to that of HIST, AMOC(σ_2) in *A-RES* (Figure 4.7b) is still weaker than that in HIST (Figure 3.1c), but stronger than that of REST (Figure 3.1b/Figure 4.7a). The density surface that separates the upper and lower limbs in *A-RES* is 36.825σ_2, which is also in-between HIST (36.775σ_2) and REST (36.875σ_2). These results suggest that the mean AMOC is not simply determined by the mean SST and SSS states. This is likely because the density is a nonlinear function of temperature and salinity, and thus the same mean SST and SSS do not necessarily give rise to the same mean surface density.

The LF detrended STD in the upper limb in *A-RES* is comparable to that of FOSI due to FOSI SST and SSS anomalies restoring (Fig.3.1a & Fig. 4.7b). In contrast, the LF

detrended STD in the lower limb (Figure 4.7b) is weaker than that in both FOSI and REST (Fig.3.1a & Fig.4.7a), indicating that the near-surface anomaly may not be able to propagate into the deep ocean in *A-RES*. In addition, the strength of AMOC decadal variations along latitudes is much weaker in *A-RES* compared to REST, particularly north of 45°N. The amplitude in *A-RES* is even weaker than 0.4 Sv south of 35°N (Figure 4.7c & d). The peak value in *A-RES* occurs consistent to FOSI and REST at 45°N (Figure 4.7e), indicating SST and SSS anomaly restoring contribute to AMOC decadal variation locally. However, the weak strength of AMOC decadal variation in *A-RES* fails to propagate the dense water southwards. Together with the timeseries of detrended AMOC index in *M-SSS* and *C-SSS* (Figure 4.5e), it directly demonstrates that SST and SSS anomaly restoring may mainly affect the upper limb of AMOC and less touch the lower limb of AMOC.

The relation between decadal variations of AMOC lower limb and SSH in *A-RES* is shown in Figure 4.8. Unlike FOSI and REST in Figure 4.3, the transition phases of AMOC and SSH in *A-RES* are mismatched. It is difficult to identify a clear southward propagation in SSH, suggesting that AMOC variability in the abyssal ocean does not drive SSH variability as reasoned by Yeager (2020) in *A-RES*. Together with the over twice weaker amplitude in dense AMOC compared to FOSI and REST, it is evident that *A-RES* fails to simulate a comparable historical AMOC decadal variation that drives the upper ocean (Figure 4.3 and Figure 4.8).

Overall, this subsection demonstrates the role of SSS climatologies and SSS anomalies in simulating decadal variability of AMOC. SSS climatology is the dominant

factor, which corrects the near-surface density mean state to dictate the deep convection, while SSS anomaly restoring only plays a role in the upper ocean without bias correction of mean state. Even so, unrealistic SSS anomaly restoring may still mess up the deep ocean variability, like *M-SSS*. Thus, SSS-climatology restoring may be the optimal choice for the restoring technique, considering the large uncertainty of SSS anomaly in the reality.

4.4 Conclusion and Discussion

In this chapter, we mainly discuss the role of SSS in simulating historical decadal variability of AMOC and model AMOC simulation sensitivity to the treatment of SSS restoring in CESM2 framework. The results from a suite of CESM2 sensitivity experiments indicate:

1) Strong SSS restoring is essential to produce decadal variability in CESM2 through dictating the deep convection in the Labrador Sea;
2) Compared to correcting SSS anomaly, correcting climatological SSS has a more dominant impact on simulations of AMOC decadal variation. A realistic SSS climatology along with a strong realistic SST restoring is critical for maintaining a realistic Arctic sea-ice extent and mean near-surface density state in the North Atlantic, which are vital for simulating deep convection activities in the Labrador Sea and ensuring propagation of dense water anomalies in the deep ocean;
3) Local near-surface density anomalies in the Labrador Sea that drive the decadal variability of AMOC are primarily controlled by SST anomalies in the North Atlantic, indicating the importance of local surface heat flux forcing;

4) Only constraining SST and SSS anomalies while keeping model climatology intact can lead to inconsistencies between anomalies and mean state, which can have a negative impact on anomaly propagation, causing the simulated AMOC decadal variation too weak and too confined near the source region;
5) Finally, the skillful simulation of AMOC decadal variation does not depend on FOSI solution, and similar results are obtained using observed monthly SST combined with observed SSS climatology, suggesting these results may be more general than for the CESM only.

Understanding the role of SSS in simulating historical decadal variations of AMOC has important implication to how we should assimilate ocean observations into climate models to generate realistic AMOC variation. Since observed SSS data is much sparser than observed SST, how to assimilate SSS into climate models is an issue. Our sensitivity experiments suggest that assimilating observed SSS climatology should be sufficient for a realistic simulation of AMOC decadal variation. If this result holds, it may suggest that assimilating monthly mean SST observation, such as ERSSTv5, and SSS climatology, such as WOA13v2, may be a strong candidate for initializing decadal predictions. However, it remains to be demonstrated that this alternative initialization can lead to improved decadal prediction skill.

Table 1 List of sensitivity experiments

Experiments	Ensemble Size	Restoring Target: SST	Restoring Target: SSS	Restoring Timescales (day): SST	Restoring Timescales (day): SSS	Purpose
S-SSS	6	Monthly-mean ERSSTv5	Monthly climatological WOA13v2 SSS	10	10	Examine the impact of SSS-restoring on AMOC simulation
W-SSS	6	Monthly-mean ERSSTv5	Monthly climatological WOA13v2 SSS	10	365	
M-SSS	6	Monthly-mean ERSSTv5	Monthly-mean FOSI SSS	10	10	Examine the relative importance of SSS climatology *vs.* anomalies
C-SSS	6	Monthly-mean ERSSTv5	Monthly climatological FOSI SSS	10	10	
A-RES	6	Monthly-mean FOSI SST anomalies + monthly climatological HIST SST	Monthly-mean FOSI SSS anomalies + monthly climatological HIST SSS	10	10	

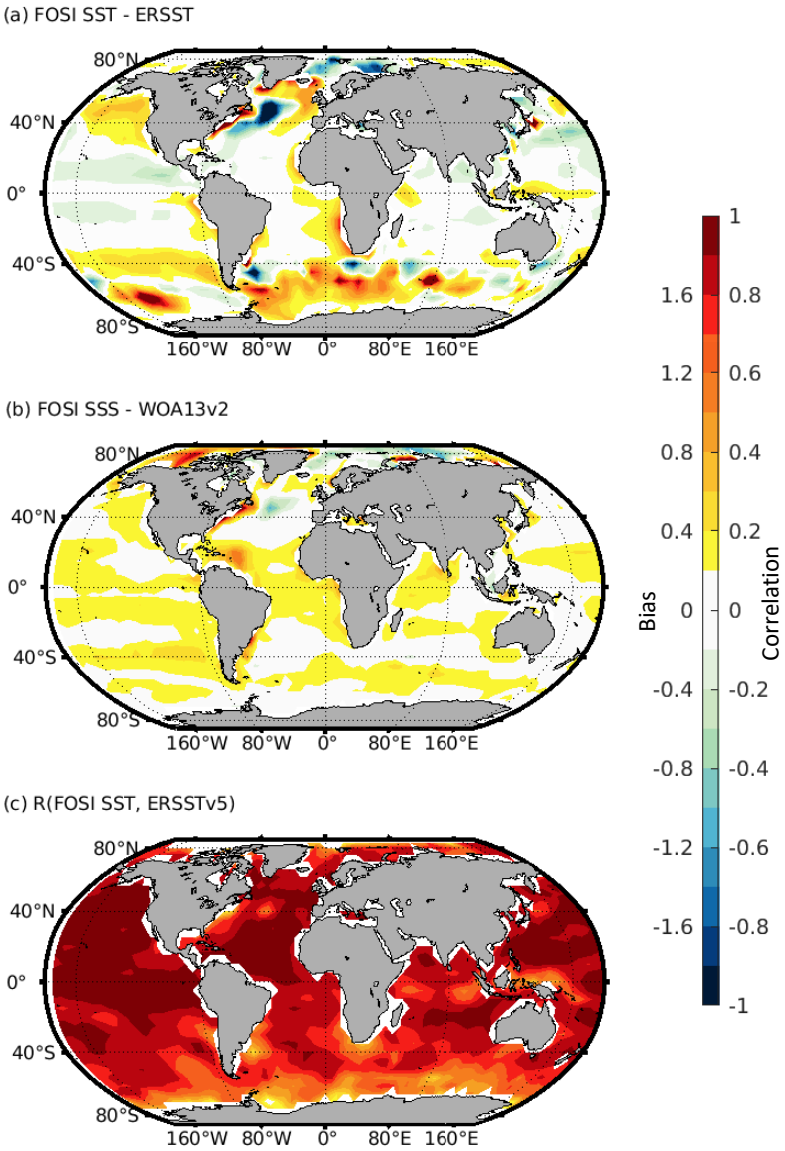

Figure 4.1 FOSI bias in SST and SSS compared to observations. Mean state differences between (a) FOSI SST and ERSSTv5, (b) FOSI SSS and WOA13v2 SSS. (c) Correlation coefficients between annual-mean FOSI SST and annual-mean ERSSTv5. Time period for both FOSI and ERSSTv5 is 1975 - 2014. Climatological period for WOA13v2 is between 1955 and 2012.

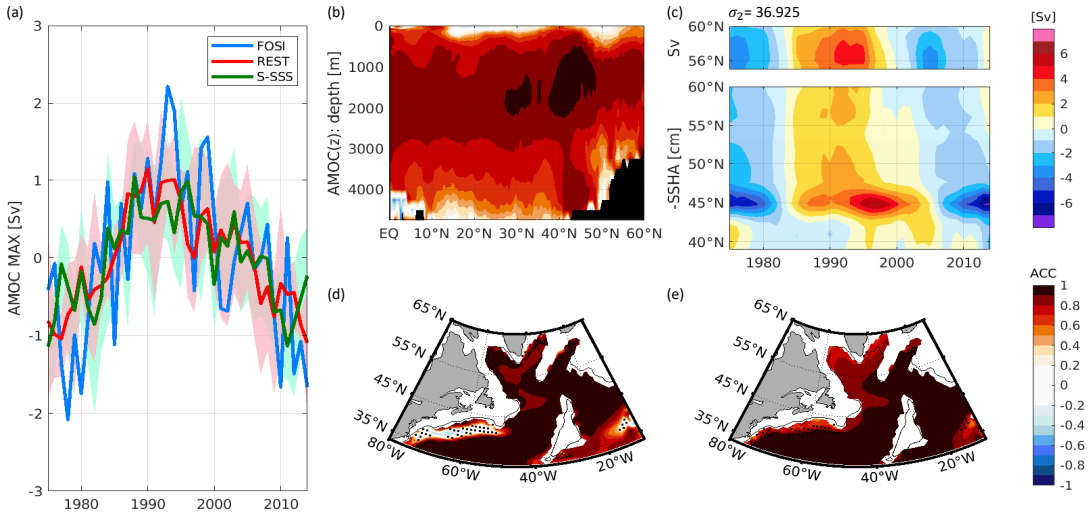

Figure 4.2 Replicability of *S-SSS* to FOSI and REST in decadal variability of AMOC and its related features. (a) Detrended annual-mean AMOC(z) streamfunction maximum transport anomaly time series for the 1975-2014 period from FOSI (blue), ensemble mean of REST (red), and ensemble mean of *S-SSS* (green); (b) ACC of detrended LF AMOC(z) between ensemble mean of *S-SSS* and FOSI; (c) LF detrended AMOC (σ_2) along 36.925σ_2(upper, unit: Sv) and LF detrended zonal-averaged sea surface height (SSH) anomalies (multiplied by -1) between 40°W and 55°W (bottom, unit: cm) in ensemble mean of *S-SSS*; (d) ACC of LF detrended Z_{LSW} between ensemble mean of *S-SSS* and FOSI; (e) The square root of PPVF of ΔZ_{LSW} in *S-SSS*. Light red and light green shadings in (a) indicate the range of respective ensemble spreads in REST and *S-SSS*. The black contours and dots in (d) and (e) show the 3000-m isobath and regions where correlation is not significant at 95% level, respectively.

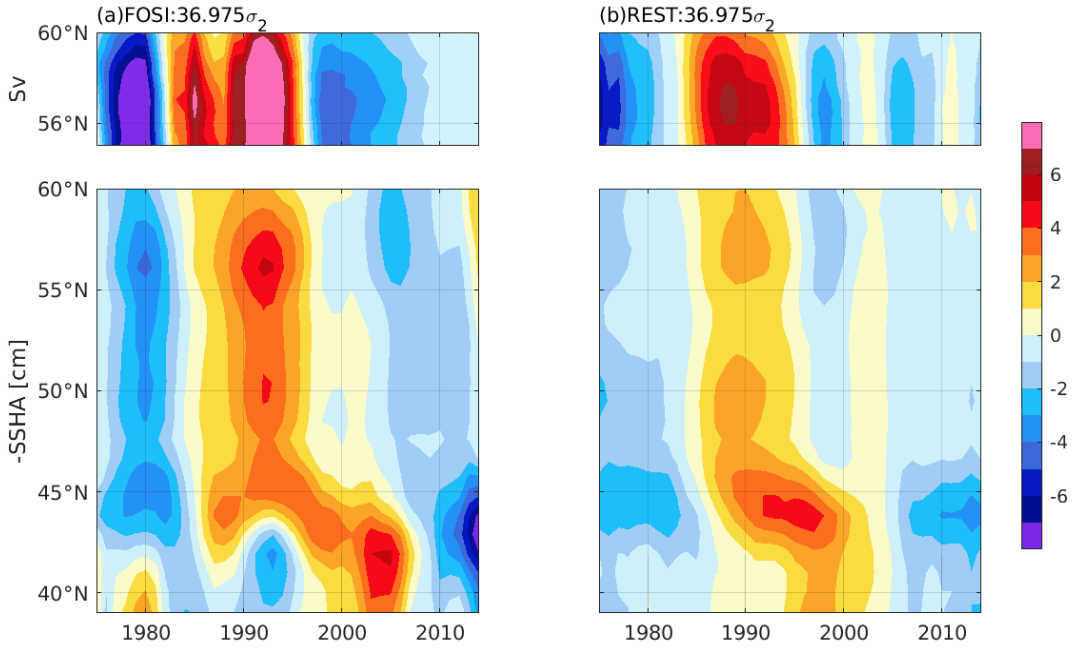

Figure 4.3 Same to Figure 3.6 a &b but removing linear trends.

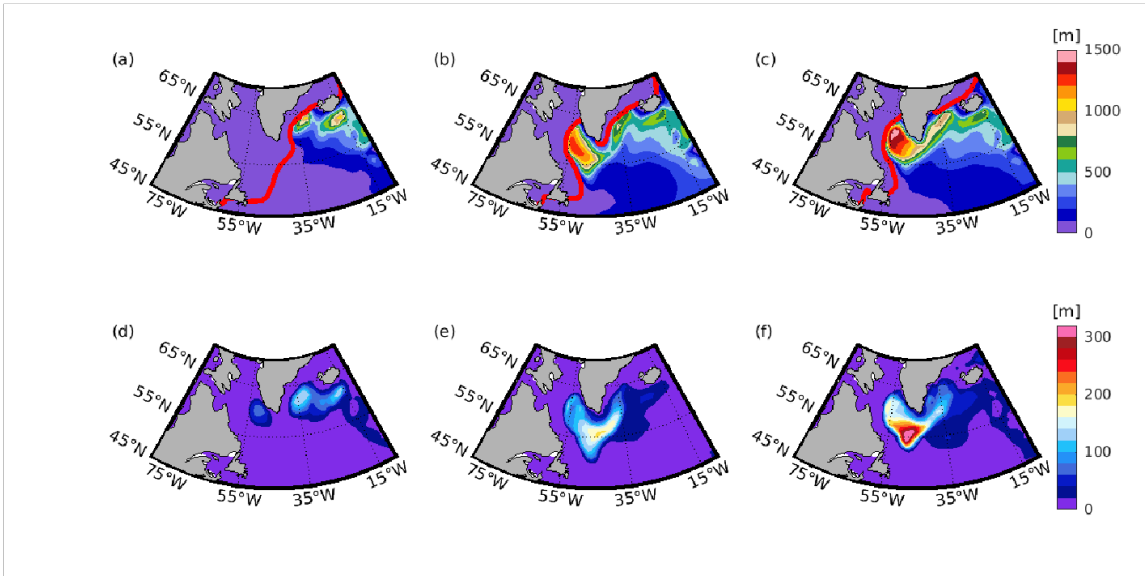

Figure 4.4 March mixed-layer depth and sea-ice edge (15% sea-ice concentration). The mean states of mixed-layer depth (color fill) and sea-ice edge (red line) in March for (a) *W-SSS*, (b) *S-SSS*, and (c) FOSI; detrended LF STD of mixed-layer depth in March for (d) *W-SSS*, (e) *S-SSS*, and (f) FOSI.

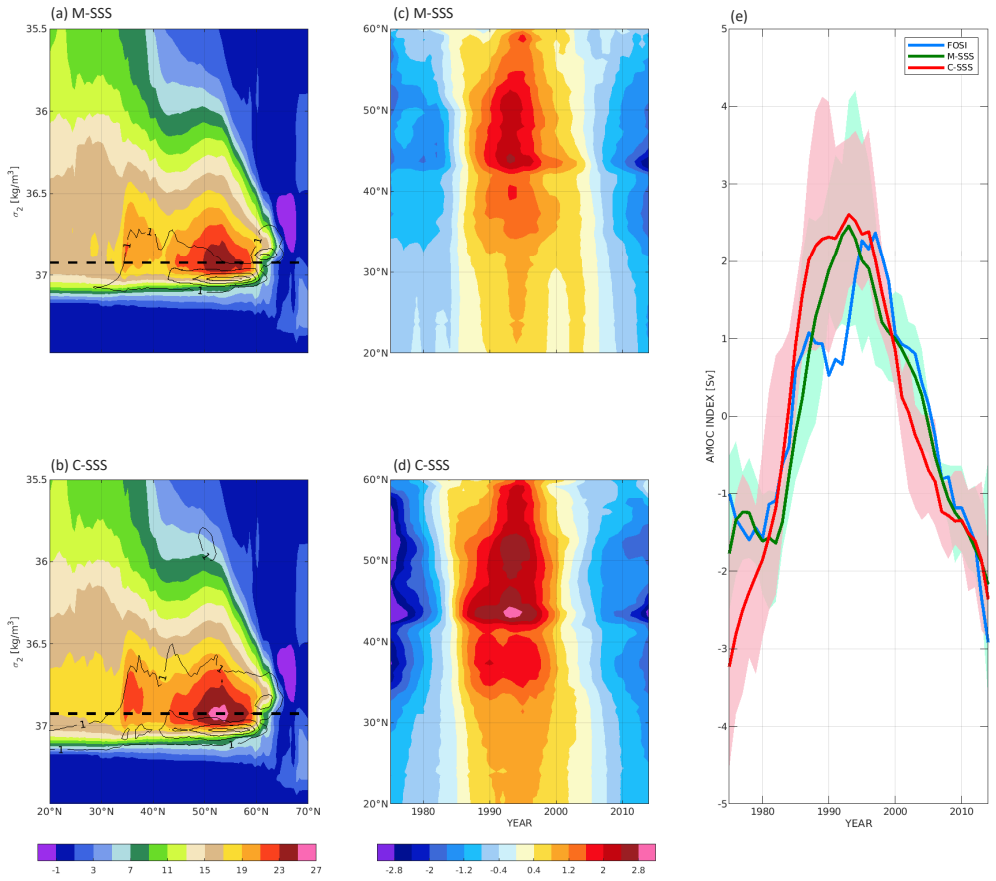

Figure 4.5 Comparisons of AMOC(σ_2) between *M-SSS* and *C-SSS*. Time mean AMOC(σ_2, color fill) and its LF detrended STD (contoured at 1 Sv interval) in (a) *M-SSS* and (b) *C-SSS*. The black dashed line at (a) 36.925σ_2 and (b) 36.925$\sigma_2$indicates the density surface where the maximum AMOC transport locates, separating the upper and lower limb of AMOC(σ_2). The LF detrended maximum AMOC(σ_2) anomaly time series from 20°N to 60°N is shown in (c) *M-SSS* and (d) *C-SSS*. The LF detrended AMOC indices (the detrended maximum AMOC(σ_2) anomaly time series at 45°N) for the 1975-2014 period from FOSI (blue), ensemble mean of M-SSS (green), and ensemble mean of C-SSS (red) are shown in (e). Light green and light red shadings indicate the range of respective ensemble spreads in *M-SSS* and *C-SSS*.

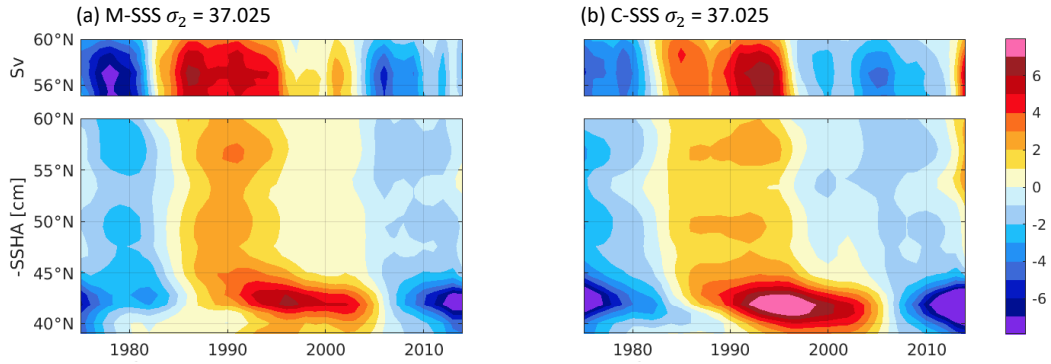

Figure 4.6 Same to Figure 4.3 except for ensemble mean of (a) *M-SSS* and (b) *C-SSS*. The AMOC density surfaces where the strongest LF detrended STDs of AMOC locate are both 37.025σ_2.

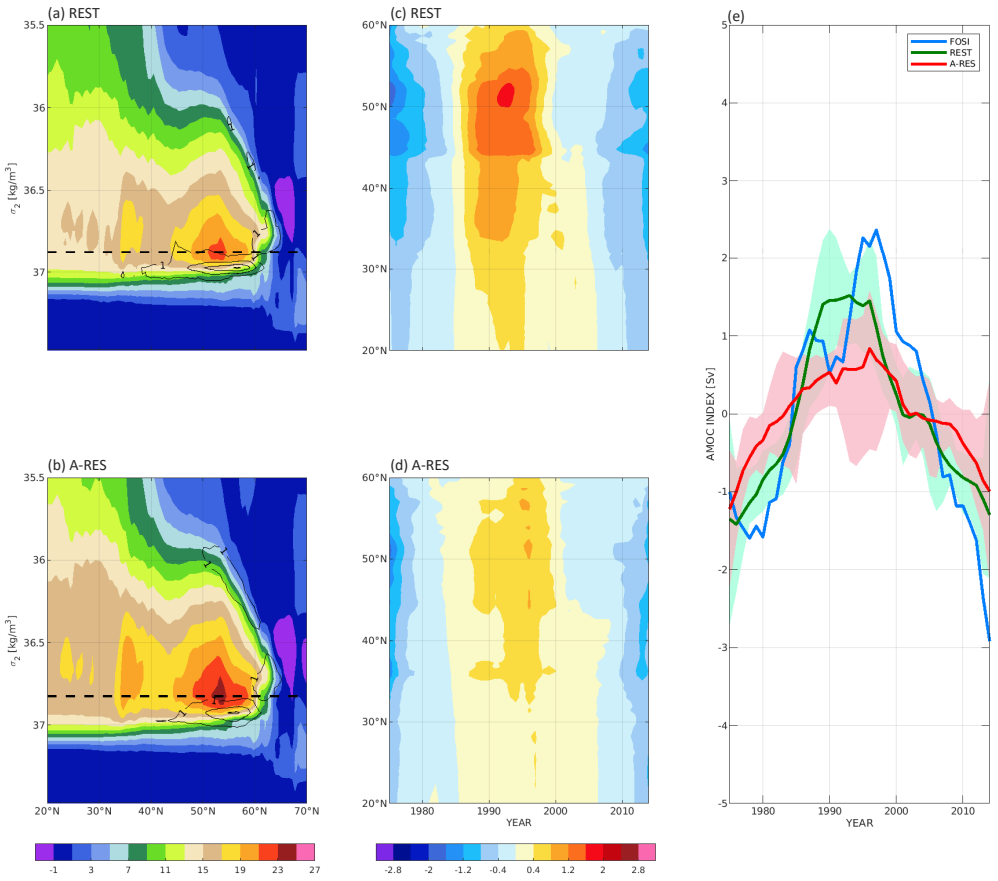

Figure 4.7 Same to Figure 4.5 but for REST and *A-RES*. Time mean AMOC(σ_2, color fill) and its LF detrended STD (contoured at 1 Sv interval) in (a) REST and (b) *A-RES*. The black dashed line at (a) 36.875σ_2 and (b) 36.825$\sigma_2$indicates the density surface where the maximum AMOC transport locates, separating the upper and lower limb of AMOC(σ_2). The LF detrended maximum AMOC(σ_2) anomaly time series from 20°N to 60°N in (c) REST and (d) *A-RES*. LF detrended AMOC indices are shown in (e) for the 1975-2014 period from FOSI (blue), ensemble mean of REST (green), and ensemble mean of *A-RES* (red). Light green and light red shadings indicate the range of respective ensemble spreads in REST and *A-RES*.

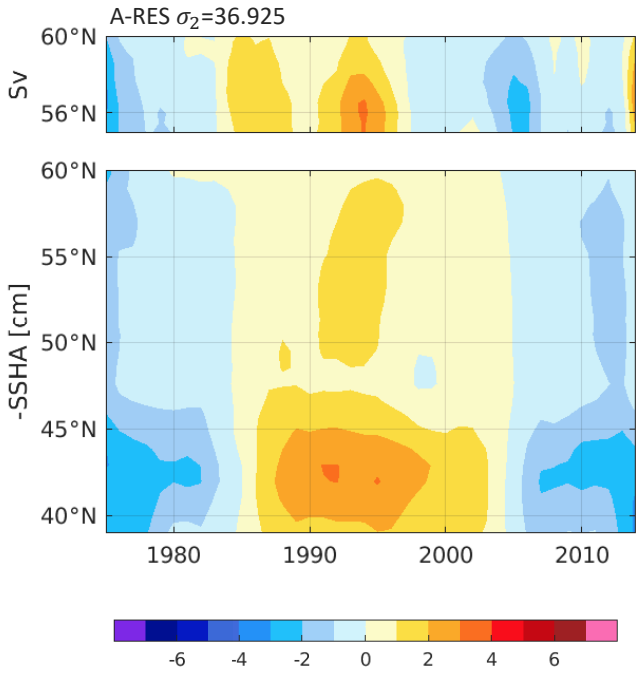

Figure 4.8 Same to Figure 4.6 except for the ensemble of *A-RES*. The AMOC density surface where the strongest LF detrended STD of AMOC locates is $36.925\sigma_2$.

CHAPTER V

PRELIMINARY ASSESSMENT OF DECADAL PREDICTION SKILL INITIALIZED FROM A NUDGED COUPLED MODEL SOLUTION

5.1 Motivation

Decadal climate prediction is relatively a new concept and has challenged the climate research community (Meehl et al, 2014). It is not a simple extension of seasonal climate predictions that have been in operations in decades and shown success in many application domains (Penny, 2017), because there are some key differences between decadal and seasonal prediction dynamics. For seasonal climate predictions, the key dynamics is centered around El Niño-Southern Oscillation (ENSO) – a spectacular coupled ocean-atmosphere phenomenon on interannual time scales that involves interactions between the tropical atmosphere and upper ocean heat content. For this reason, a skillful seasonal prediction requires a realistic initialization of the upper ocean heat content in the tropics, which is achieved by assimilating available atmospheric observations, and surface and upper ocean observations to coupled prediction models (e.g., Zhang et al., 2007; Mulholland et al., 2015). In contrast, decadal prediction dynamics resides in deep ocean variability, particularly AMOC variability in the North Atlantic (Yeager 2020), which is much less observed compared to the upper ocean heat content variability. The quality of decadal predictions very much depends on a realistic initialization of AMOC state, which has proven to be much more difficult primarily due to the lack of deep ocean observations, especially in the abyssal ocean below 2000m. As a result, initialization techniques developed for seasonal climate predictions, such as

three-dimensional data assimilations, have shown difficulties in decadal climate predictions. For example, Karspeck et al. (2017) show that the existing three-dimensioanl data assimilation products have an inconsistent AMOC vertical structure and inconsistent historical AMOC decadal variation, which may lead to poor decadal prediction skill. Therefore, Yeager et al. (2018) have advocated for using FOSI, instead of three-dimensional data assimilation, to initialize decadal climate prediction.

As discussed in Chapter 1, unlike the data assimilation products, multi-model FOSI simulations revealed a similar AMOC decadal variation despite of large differences in the time-mean AMOC state. This result suggests that historical AMOC decadal variation is robust and FOSI solution may be used to initialize decadal climate prediction. CESM-DPLE with 40 ensemble members and 62 start years in Yeager et al. (2018) demonstrates the feasibility of FOSI-initialization in generating skillful decadal predictions, particularly in the northern North Atlantic where long ocean memory is provided by AMOC decadal variation (Figure 5.1).

Despite of the initial success of CESM-DPLE, as discussed in the previous Chapters, FOSI initialization can suffer from significant ocean initialization shock which may degrade the initialization prediction skill based on the experience of seasonal prediction (Chen et al., 1995). A potential remedy to this problem is to use surface restoring in a coupled prediction model, as shown in Chapter 3 and 4. In this chapter, we will test this alternative initialization method to FOSI by a carrying out two ensembles of prediction simulations: one ensemble is initialized by FOSI and another is initialized by the surface-restored coupled model solution. After a brief description of decadal

prediction simulations in section 5.2, a preliminary assessment of the two prediction ensembles is discussed in section 5.3 by comparing the predictions to hindcasts, UI and persistent prediction. A short discussion will be followed in section 5.4.

5.2 Experimental Description

Two initialized decadal prediction ensembles are performed with the same CESM2 that was used to generate REST. The first ensemble is initialized from REST, named as Decadal Prediction initialized from REST (DPRE), and the other ensemble is initialized from FOSI, named as Decadal Prediction initialized from FOSI (DPFO). Each ensemble includes 30 start dates (Nov. 1st from 1980 to 2009) and each start date includes 10-member, 62-month prediction simulations, totaling 300 CESM2 simulations forced by CMIP6 historical external forcings. The DPRE members are generated from the 6 members of REST and round-off perturbations to atmospheric initial conditions. The initial conditions of land, atmosphere and river components in DPFO are more complicated, 6 of which are from REST, plus one from S-SSS (restored to ERSSTv5 and WOA13v2 SSS), and the other 3 members are initialized from JRA55 reanalysis (Kobayashi et al., 2015) with round-off perturbations added. The JRA55 based initial conditions are also used for the Seasonal-to-multiyear Large Ensemble (SMYLE) Experiment at NCAR (https://www.cesm.ucar.edu/working-groups/earth-system-prediction/?ref=nav). The atmosphere model data in SMYLE is directly interpolated from JRA55 analysis and the land is forced by CRU JRA (Harris, 2019; Yeager, 2021). The different initial conditions of land, atmosphere and river components in DPRE and DPFO are not expected to have a major impact on decadal prediction results considering

their relatively short memory compared to the ocean memory. Table 2 shows a brief overview of these two initialized prediction ensembles. We note that all the initial conditions from the surface restoring technique are restored to SST and SSS globally including the sea ice regions in this chapter due to the similar results in AMOC and deep ocean with/without SST and SSS restoring under the sea ice.

Besides the two initialized prediction ensembles, uninitialized forecast (UI) and persistence forecast will also be used in this chapter as a baseline to assess the prediction skill. UIs are the 10-member HIST forced by the same external forcing with DPRE and DPFO, which reveals the role of external forcings in the long-term predictions. The persistence forecast starts from the year of initialization, which includes the first 2 lead months that DPRE and DPFO predict, November and December, persist for the following 5 years.

In addition, annual-mean is defined over January – December and lead year means the annual-mean of the prediction. For example, the first lead year, denoted as LY1, is the average of month 3 (January) to month 15 (December) from initialized predictions. LY0 refers to the first lead month of predictions (November in each start year), whose fields are close to initial conditions. The 5-year mean prediction is the average of the first 5 lead years of prediction (hereafter LY1-5). All analyses are carried out after a drift adjustment is applied, which is introduced in Section 2.4.3. We focus on anomaly analyses unless otherwise noted, and all results are based on the average of 10-ensemble member.

5.3 Preliminary Results

5.3.1 Prediction Skill in Global Upper Ocean

The decadal prediction skill of global SST is first assessed. Figure 5.2 shows the pentadal ACC skill score in DPRE, DPFO, HIST and its difference, ΔACC, between these experiments and persistent prediction derived from ERSSTv5. The positive ACC score in DPRE locates in the North Atlantic, Indian Ocean and the Western Pacific, where DPFO also shows positive ACC values. However, the positive ACC score in DPRE reveals higher values compared to that of DPFO in SPNA, Indian Ocean and Western Pacific, and ΔACC between DPRE and DPFO (DPRE minus DPFO) can reach as high as 0.3 in the central SPNA (Figure 5.2e). This improved forecast skill may be related to the reduced initialization shock in DPRE compared to DPFO with more balanced atmosphere and ocean states in DPRE as shown in previous Chapters. That is, reducing initialization shock can improve forecast skill not only on seasonal time scales as shown in many previous studies (e.g. Chen et al., 1995; Keenlyside et al., 2005), but also on decadal time scales. However, we also note some ΔACC negative values in the eastern Pacific, indicating a worsening forecast skill in DPRE compared to DPFO. One possible reason may be that ENSO-related upper ocean heat content variability in DPRE initial condition is less realistic than that in DPFO initial condition, because the latter is generated using observation-based atmospheric forcing, while the former is generated by an atmospheric model forced by observed SST. Any biases in atmospheric model simulation of ENSO-related tropical atmosphere variability can lead to errors in tropical ocean heat content, deteriorating model ENSO forecast skill in the eastern Pacific.

Comparing ACC scores between DPRE and HIST (UI) indicates that the improved forecast skill in the initialized prediction is largely confined in SPNA where AMOC dominates decadal variability (Figure 5.2c&f). This suggests that external forcings make a significant contribution to the high ACC scores outside of SPNA, which is consistent with the results from Yeager et al. (2018). In addition, a part of the subtropical North Atlantic shows a higher score (~0.15) in DPRE relative to UI. Another better performant region in DPRE relative to UI is the eastern Pacific, although the score in DPRE remains negative. Compared to persistent prediction, the initialized decadal prediction is superior nearly everywhere (Figure 5.2d&g), which is again in agreement with Yeager et al. (2018).

ACC of global upper ocean heat content (T295m) is displayed in Figure 5.3. All prediction ensembles show positive ACC scores with an AMV-like pattern in the North Atlantic, suggesting the long ocean memory in this region. Compared to UI and persistent prediction, the skill in DPRE is higher in the extra-tropical North Atlantic. The ACC score in DPRE is also slightly higher than that of DPFO over much North Atlantic, although the increase is small with a value of 0.1-0.2 over the SPNA and ~0.4 near the coast of Northern Africa. Within SPNA, DPRE shows a higher skill than DPFO just south of Greenland, where the ocean current transports relatively warm and salty North Atlantic water into LS and affects deep convection in the region, which in turn can have an impact on AMOC variability. As shown in Chapter 1 (see Figure 1.2), CESM2 has a significant bias in its simulated surface wind stress in SPNA. Therefore, it is plausible that DPFO experiences a significant initialization shock in this region because of the

large wind stress bias. The improved ACC score in DPRE may be related to the reduction of initialization shock in DPRE (Figure 5.4). In the next subsection, we present more detailed analyses in the North Atlantic sector where DPRE shows improved ACC score than DPFO.

5.3.2 Prediction skill in North Atlantic Sector

In this subsection, we focus on the SST in the northern North Atlantic and the Sahel precipitation, where decadal variability is pronounced as shown by previous studies (e.g. Born et al., 2012; Nicholson & Entekhabi, 1986) and initialized decadal prediction shows higher ACC score than UI climate simulations as shown in Yeager et al (2018) and in the previous subsection.

The regionally averaged SSTs from DPRE and DPFO over SPNA at lead year 1 to 5 are shown in Figure 5.5 superimposed on the observed ERSSTv5. A visual inspection clearly indicates that DPRE follows more closely to ERSSTv5 than DPFO with less departures from ERSSTv5 at all lead years. For example, the LY1 forecasts in DPFO depart further apart from ERSSTv5 than in DPRE, indicative of more rapid drift from initial condition (LY0) in DPFO than DPRE. This rapid drift in DPFO is particularly evident in year 1982, 1983 and 1984. Another period when DPRE and DPFO show a significant difference is during 1998-2004, in which LY1 in DPFO consistently shows warmer-than-observed forecasted SST in SPNA.

The predicted SST time series from lead year 1 to 5 in DPRE, DPFO and HIST is shown in Figure 5.6. It is evident that the observation shows a shift in mid-1990s from a cold state prior to the mid-1990s to a warm state after the mid-1990s. As such, the SST

timeseries may be separated into three periods: 1) a colder state period from 1980 to 1994, 2) a transition period from 1994 to 1998, and 3) a warmer state period from 1998 to early 2010s. The predicted SST in DPRE shows a good agreement with the observation in all lead years compared to DPFO and HIST. HIST fails to simulate the abruptness of the shift, instead predicts a gradual warming from the early 1980s to the early 2000s. DPFO predicts these three periods but with a relatively poor agreement with the observations in the early 1980s, particularly at long lead times. In contrast, DPRE shows a consistently good agreement with the observations in all three periods at all lead years.

The improved prediction skill in DPRE is further confirmed by the ACC and RMSE skill scores of regionally averaged SST time series over the SPNA shown in Figure 5.7. The skill score at LY0 is included for DPRE and DPFO. It is evident that DPFO has higher skill scores at LY0 than DPRE, because the initial condition from FOSI is closer to the observations than that from restored coupled model solution. From LY1 onwards, the skill score from DPFO drops rapidly and becomes lower than that of DPRE. For example, the ACC score of DPRE remains at 0.86 or higher from LY3 to LY5, whereas the score of DPFO drops to just above 0.8. In fact, the ACC score of DPFO is even below that of HIST from LY3 to LY5, while the score of DPRE is always higher than that of HIST. The RMSE skill score shows similar results: DPFO has much lower RMSE at LY0 than that of DPRE, but RMSE increases rapidly from LY1 onwards and becomes higher in DPFO than in DPRE. The rapid increase of RMSE in DPFO is consistent with the notion that there is a significant initialization shock in DPFO, causing

a rapid adjustment in the ocean after initialization. In contrast, the RMSE in DPRE remains relatively steady throughout LY0 to LY5, indicating a much less initialization shock. Overall, both ACC and RMSE scores show that DPRE possesses the best forecast skill at LY3 to LY5, more superior than DPFO, HIST and persistent forecast.

It has been shown by previous studies that a skillful decadal forecast of SST in the North Atlantic can translate to a skillful forecast of Sahel rainfall over the West Africa (e.g., Yeager et al. 2018). This result is confirmed by DPRE. Figure 5.8 shows predicted and observed rainfall anomaly time series averaged over the West African Sahel (20°W – 10°E, 10°N – 20°N) during boreal summer months of July, August and September (JAS) that corresponds to the onset of West Africa Monsoon. The predicted rainfall is based on the average of LY1 to LY5. The ACC of the predicted Sahel rainfall is 0.68, 0.65, 0.74 and 0.13 for DPRE, DPFO, HIST and persistent prediction, respectively. MSSS (an assessment metric related to the magnitude bias comparison explained in the section 2.4.4) of DPRE is 0.016, 0.033 and 0.659 with the reference to DPFO, HIST and persistent prediction, respectively. There is no obvious improvement for decadal prediction of summer Sahel rainfall from DPRE over DPFO. In fact, the ACC score is the highest using HIST. This may suggest that the recent trend in Sahel rainfall may be dominantly forced by external forcings. However, it may be premature to conclude that initialized decadal prediction does not lead to any improvements in predicting Sahel rainfall, because 1) the results presented here is based on a relatively short period from early 1980s to early 2010s, and 2) the ensemble size 10 may be inadequate to evaluate rainfall prediction skill because the larger internal variability in

the atmosphere than in the ocean. Therefore, the skill of predicting Sahel rainfall needs to be further examined by extending prediction period further back in time and by increasing the ensemble size as argued by Yeager et al. (2018).

5.4 Discussion and Conclusion

In this chapter, we show some preliminary results from two ensemble decadal prediction experiments, DPRE and DPFO. The predicted SST over the northern North Atlantic shows improved skill scores in DPRE over DPFO, which supports the notion that a more balanced atmosphere-ocean states in DPRE can reduce initialization shock, leading to more skillful decadal forecast. However, no significant improvement in decadal prediction of summer Sahel rainfall is found in DPRE, which may be attributed to the shortness of prediction period and the small ensemble size used in these preliminary prediction experiments.

As we discussed previously, realistic AMOC initialization is vital for skill decadal predictions. Reducing initialization shock can help minimize spurious wave generation during ocean adjustment caused by imbalance between atmosphere and ocean initial state, which can lead to a more smoothed AMOC evolution during a prediction cycle (Figure 5.9). Comparing AMOC evolutions between DPRE and DPFO, it is clear that AMOC change in DPRE is much smoother and follow more closely to the AMOC in FOSI, which is considered as “observation” in our modeling framework. In DPFO, LY1 AMOC states are generally much further away from the observation compared to those in DPRE, suggesting that there is a rapid drift in these AMOC states from the initial states given by FOSI. These “noisy” AMOC evolutions in DPFO are consistent

with the notion of imbalanced ocean-atmosphere initial states that cause initialization shock. Therefore, the results shown in Figure 5.9 is consistent with those shown in Figure 5.5. We hypothesize that the "noisy" SST evolutions are connected with the "noisy" AMOC evolutions in DPFO. But future studies need to show how the dynamic linkage between the two.

Finally, we would like to discuss the potential improvement of DPRE. We notice that the ocean initial condition from DPRE, REST, has a larger bias and lower ACC than the ocean initial condition from DPFO, FOSI (Figure 5.7 LY0), which may degrade the prediction skill at short lead times. Particularly, in the tropical Pacific where upper ocean heat content plays a dominant role in SST prediction at seasonal time scales the less realistic initial condition from REST can have a major negative impact on SST prediction. That is, even though the initialization shock may be reduced from REST initialization, the short-term forecast skill may still be degraded from the less realistic upper ocean initial condition in REST. Figure 5.10 and Figure 5.11 show SST (raw data) mean state bias in tropical Pacific and the vertical temperature (raw data) mean state bias along the equator from DPRE and DPFO, relative to the initial states from REST and FOSI, respectively. It is obvious that the error in DPFO is larger than that in DPRE at the first lead month (LM) due to the initialization shock for both surface and vertical structures. The thermocline in DPFO adjusts rapidly due to the inconsistent atmospheric forcing field between FOSI and DPFO. The bias increases rapidly in DPFO as the lead time increases, whereas the error in DPRE develops much slower without apparently thermocline adjustment. The magnitude of bias in DPFO is almost twice or even larger

than that in DPRE at LM3. These results suggest that the REST initialization strategy enables to a smooth transition from the ocean initial state in the upper ocean. Thus, if the error in REST could be reduced, there should be a potential to generate higher prediction skill, specifically in the regions dominated by upper ocean heat content.

Table 2 Overview of the experimental setups of the two initialized decadal prediction simulations

		DPRE	DPFO
Model		CESM2 (1°)	
Initialization	ocn/ice	REST*	FOSI
	atm/lnd/rof	REST*	REST*/S-SSS*/SMYLE
Forcing		CMIP6 historical	
Ensembles	Ensemble size	10	
	Start dates	Annual; Nov 1, 1980-2009 (N=30)	
	Ensemble generation	01-06: Nov start days from REST* 07-10: round-off perturbation of atm initial conditions from REST* start days	01-06: Nov start days from REST* 07: Nov start days from S-SSS* 08-10: Nov start days from SMYLE and round-off perturbation of atm initial conditions
	Simulation length	62 months	

* Both SST and SSS are restored globally including the region covered by sea ice.

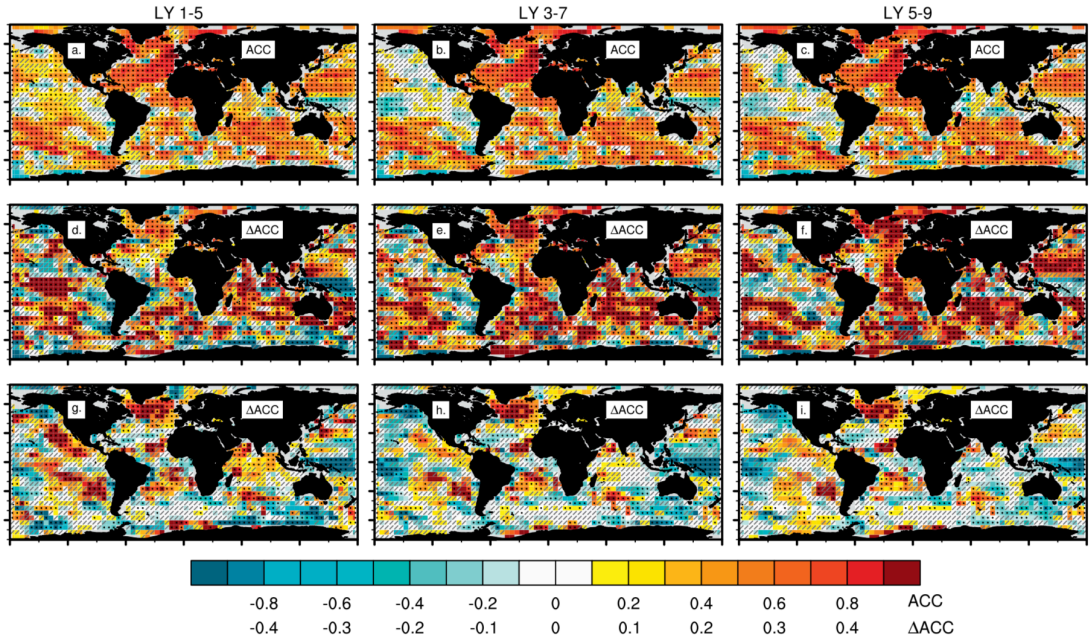

Figure 5.1 Decadal prediction skill of annual T295m in CESM-DPLE (from Yeager et al., 2018 FIG. 1). ACC skill score between DPLE and EN4.2.1 for lead year (a) 1-5, (b) 3-7, and (c) 5-9; ΔACC between DPLE and persistent prediction for lead year (d) 1-5, (e) 3-7, and (f) 5-9; ΔACC between DPLE and uninitialized simulation (UI) for lead year (g) 1-5, (h) 3-7, and (i) 5-9.

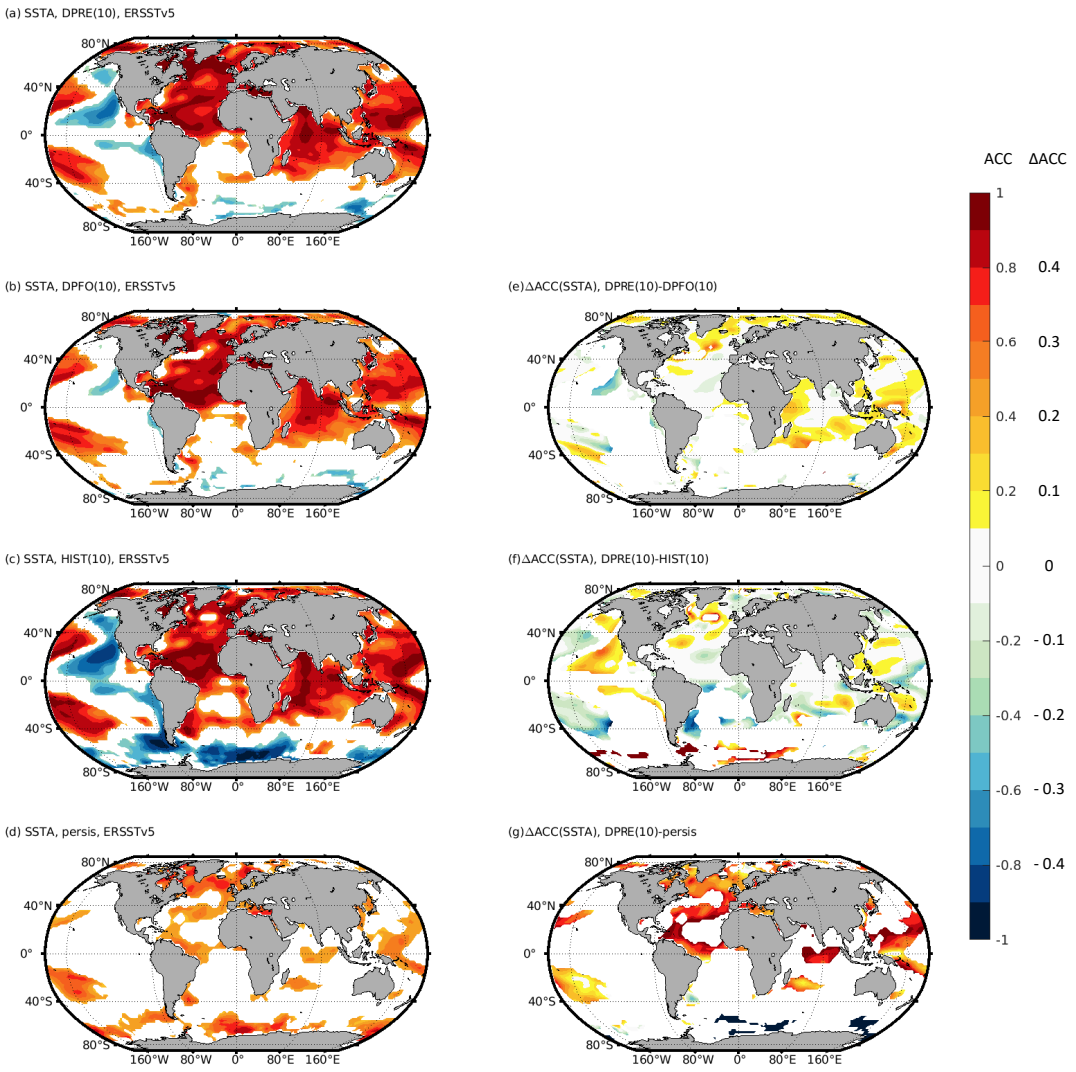

Figure 5.2 Prediction skill of annual SST globally for LY1-5. ACC relative to ERSSTv5 from (a) DPRE, (b) DPFO, (c) HIST, and (d) persistent prediction; ΔACC between (e) DPRE and DPFO, (f) DPRE and HIST, and (g)DPRE and persistent prediction. Color filled grids are regions where ACC pass 95% significant level. All fields are mapped to 2° × 2° grids.

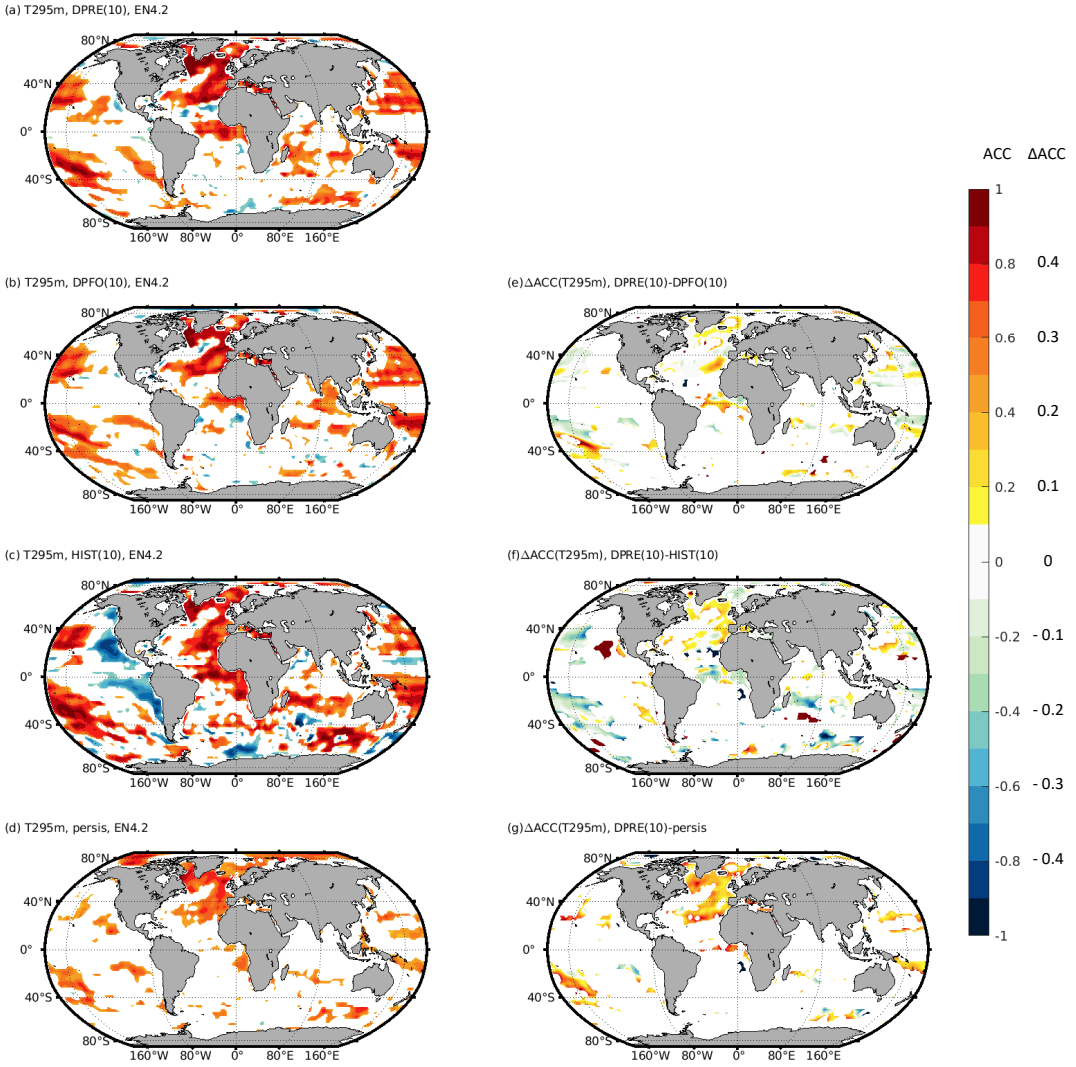

Figure 5.3 Prediction skill of annual T295m globally for LY1-5. ACC relative to EN4.2.1 from (a) DPRE, (b) DPFO, (c) HIST, and (d) persistent prediction; ΔACC between (e) DPRE and DPFO, (f) DPRE and HIST, and (g)DPRE and persistent predictions. Color filled grids are regions where ACC pass 95% significant level. All fields are mapped to 2° × 2° grids.

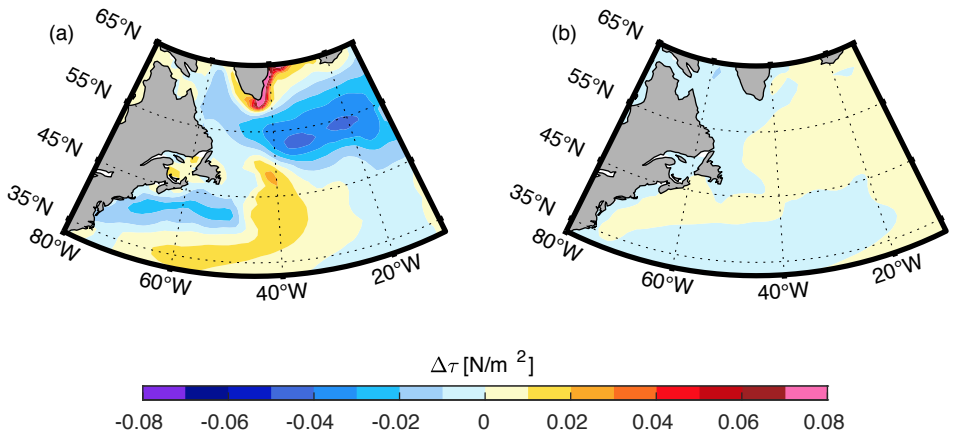

Figure 5.4 Same to Figure 3.9 e&f but focuses on the North Atlantic. Wind stress differences in the North Atlantic between (a) FOSI and HIST, and (b) REST and HIST (unit: N/m^2).

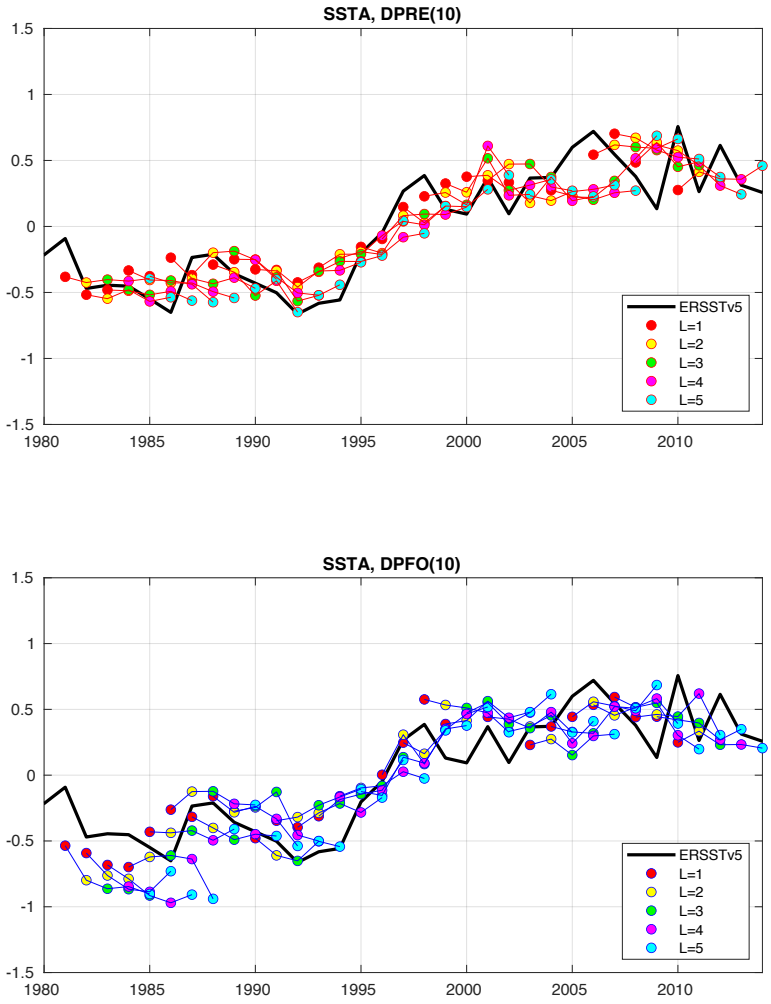

Figure 5.5 regionally averaged SST timeseries in (upper) DPRE and (lower) DPFO for the period of 1980-2014. The black line represents ERSSTv5; the ensemble mean prediction simulations from each start time are plotted in red lines (DPRE) and blue lines (DPFO), respectively; the colorful dots suggest the 10-ensemble-member-mean at different lead years from LY1 to LY5. The analysis region is in 45°N-65°N, 75°W-0.

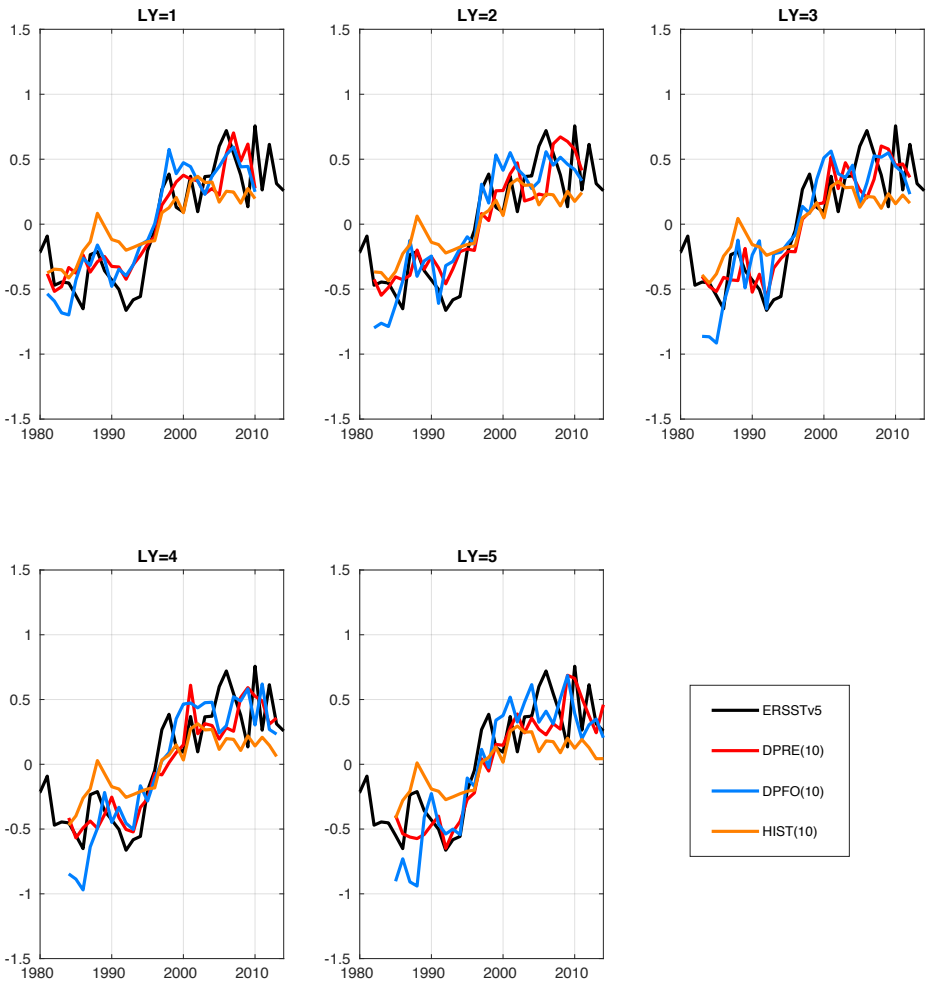

Figure 5.6 Regionally averaged SST timeseries at different lead years from ERSSTv5 (black), ensemble mean of DPRE (red), ensemble mean of DPFO (blue), and ensemble mean of HIST. The analysis region is in 45°N-65°N, 75°W-0, same to the one in Figure 5.5. The number after the legend indicates the ensemble member.

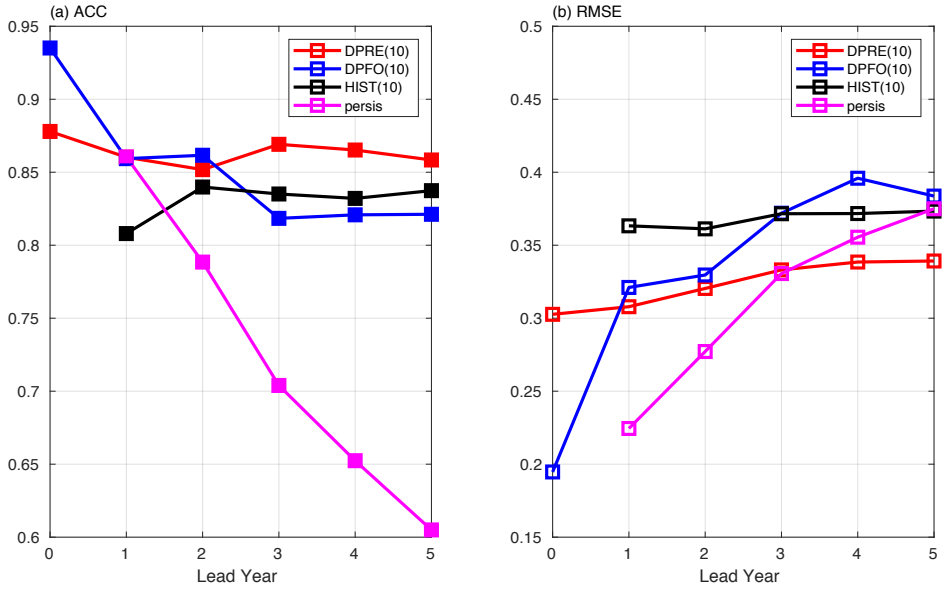

Figure 5.7 Prediction skill of SST in regionally averaged SPNA relative to ERSSTv5. (a) ACC and (b) RMSE at different lead years in DPRE (red), DPFO (blue), HIST (black), and persistent predictions (magenta). The solid squares in (a) indicate the values that pass 95% significant level. The analysis region is in 45°N-65°N, 75°W-0.

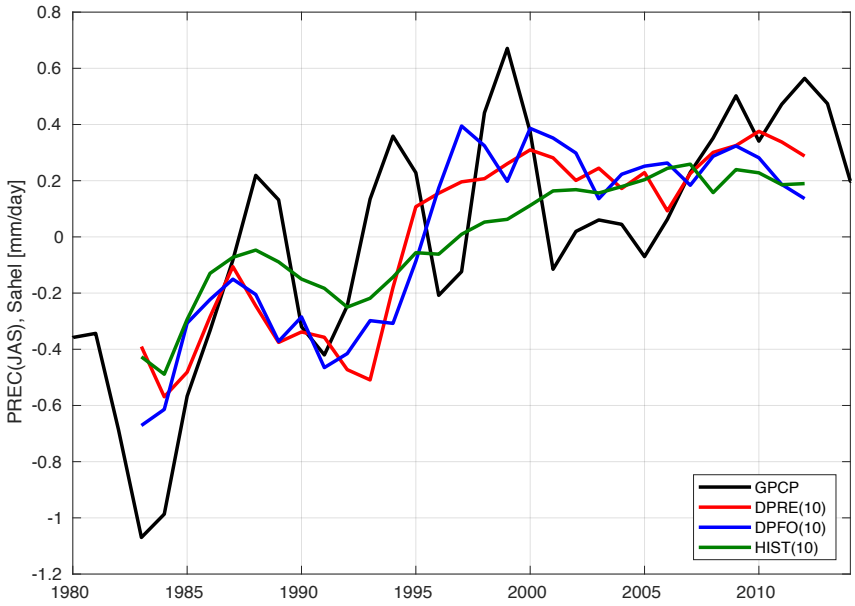

Figure 5.8 Regionally averaged- boreal summer (JAS) precipitation anomaly timeseries for the West African Sahel (10°N – 20°N, 20°W – 10°E). GPCPv2.3 (black) and the ensemble mean of HIST (green) timeseries have been smoothed with a 5-year-running-mean; the ensemble mean of DPRE (red) and the ensemble mean of DPFO (blue) timeseries are over LY1-5.

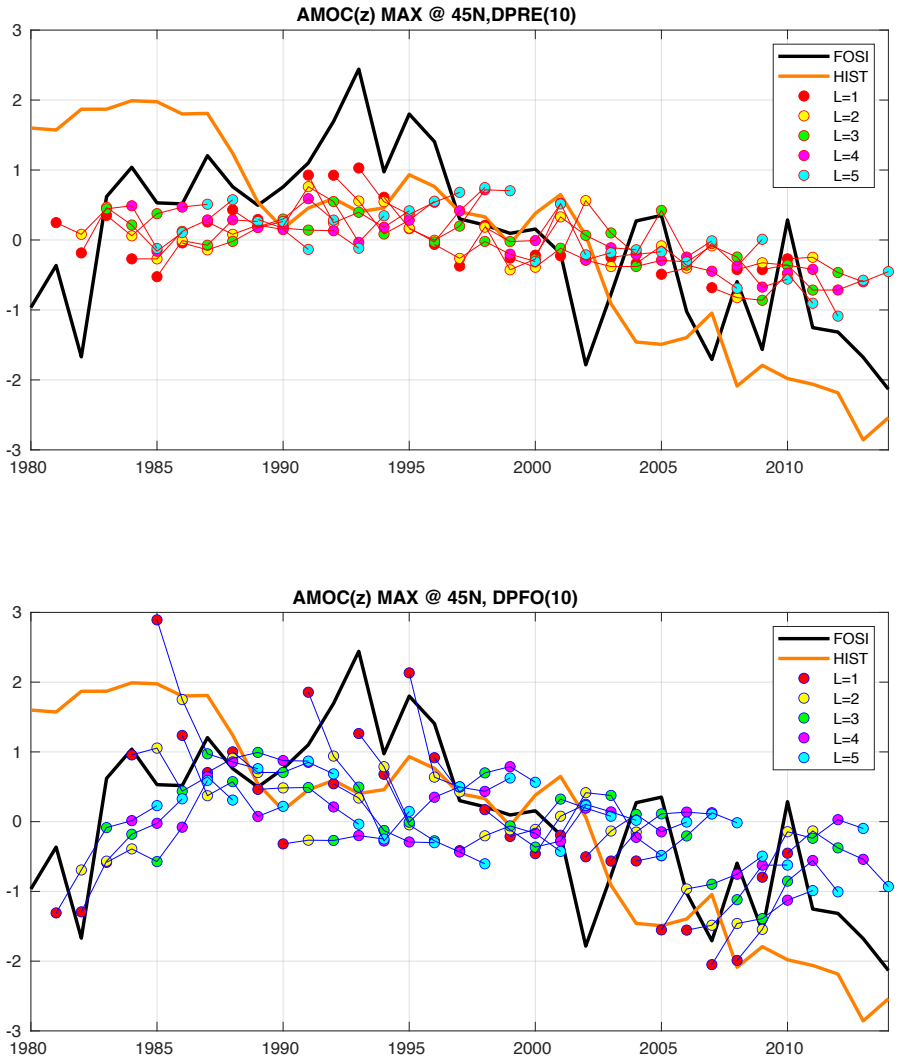

Figure 5.9 AMOC(z) maximum timeseries at 45°N in DPRE (upper) and DPFO (lower) from FOSI (black), HIST (orange), DPRE (red), and DPFO (blue). The different filed circle in different colors indicate different lead years.

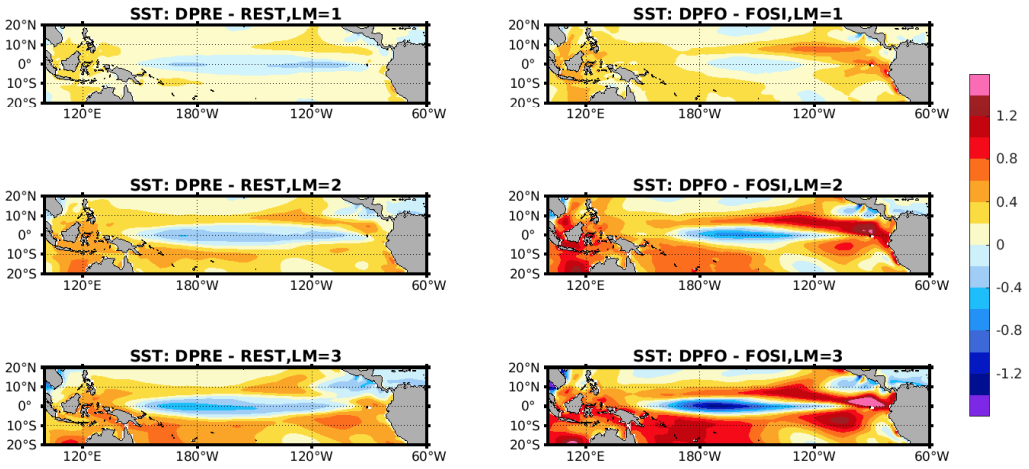

Figure 5.10 SST (raw data; unit: °C) mean state bias in tropical Pacific from DPRE (left) and DPFO (right) relative to REST and FOSI from the first lead month to the third lead month (LM1 – LM3).

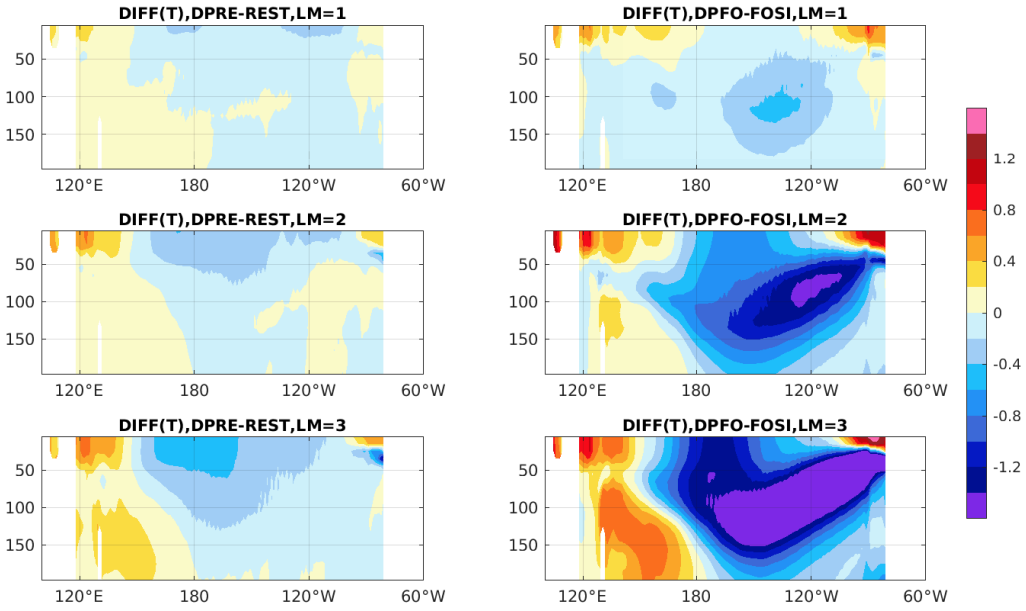

Figure 5.11 Same to Figure 5.10 but for the vertical temperature (raw data; unit: °C) at Pacific equation

CHAPTER VI

CONCLUSIONS AND FUTURE WORKS

The overall goal of this dissertation is to show that 1) the historical AMOC decadal variation can be simulated in a coupled climate model that is used for decadal climate prediction, 2) such a coupled model simulation can then be used to initialize decadal climate prediction and yield improved forecast skill through reducing initialization shock. Using FOSI as "truth" due to the lack of long-term AMOC observations, we developed and evaluated a coupled modeling strategy to simulate historical AMOC decadal variation by restoring only SST and SSS in a coupled model simulation. We then investigated the role of SSS restoring in simulating AMOC decadal variation by conducting an extensive set of model sensitivity experiments. Finally, we carried out ensembles of decadal climate prediction simulations, totaling 600 individual initialized predictions in each ensemble, to examine the feasibility of using this coupled modeling strategy to initialize decadal predictions. The main conclusions could be summarized as follows.

6.1 Conclusions

Firstly, the hypothesis that restoring SST and SSS to observations alone in fully coupled CESM2 simulations can replicate the historical AMOC decadal variability is validated in the framework of FOSI. Using FOSI as *observations*, a set of 6-member coupled CESM2 simulations with SST and SSS restored to FOSI SST and SSS at 10-day restoring timescale (REST) was performed for the period of 1958-2014. A detailed analysis of AMOC decadal variation reveals that REST can replicate not only FOSI

AMOC decadal variation, but also AMOC-related deep ocean anomalies. For example, the southward and downward propagation of decadal temperature and salinity anomalies from SPNA, as well as LSW propagation in the deep ocean are captured by REST, demonstrating the high fidelity of REST in replicating AMOC decadal variability in FOSI. In addition, the upper ocean heat content simulated by REST is highly correlated with EN4.2.1 observation, further demonstrating that the high fidelity of REST is not only limited to the North Atlantic, but also extend to other ocean basins including the Pacific and Indian Ocean. Compared to FOSI, the atmospheric state in REST is much closer to that of the free coupled simulation (HIST), which rationalizes its potential use as an alternative initialization technique to FOSI in decadal prediction to reduce initialization shock.

Although previous studies (e.g. Keenlyside et al., 2018) addressed the importance of SST-restoring, strongly SSS-restoring is found to be essential for simulating historical AMOC decadal variation. A weak SSS-restoring can lead to unrealistic surface buoyancy forcing in LS, which can impede the deep convection, AMOC and the associated meridional heat transport, resulting in over-extensive winter sea-ice coverage in SPNA, and eventually shutting down AMOC. On the other hand, restoring SSS anomaly alone while keeping model mean SSS intact will also not work, because the density bias in the model can cause inconsistencies between surface density anomalies and mean density distribution in the model, which can weaken the downward propagation of surface density anomalies into the deep ocean (denser than $37\sigma_2$), causing surface density anomalies trapped in the upper ocean. This explains why AMOC

decadal variation is so weak and shallow in SSS-anomaly-restoring simulations. In contrast, the SSS-climatology-restoring simulations which correct the mean density bias in the model are more effective for simulating historical AMOC decadal variation. As long as model density bias is reduced, surface density anomalies generated by SST changes in SPNA can propagate downward into the deep ocean during deep convective events in LS and then propagate southward along the deep western boundary in the deep basin. Therefore, a major conclusion of this study is that assimilating SSS climatology into coupled climate models seems to be more important than assimilating SSS anomalies for simulating historical AMOC decadal variation.

Finally, the hypothesis that REST can be used as an alternative initialization technique to FOSI in decadal prediction to improve model forecast skill by reducing initialization shock is tested by carrying out a preliminary set of decadal prediction experiments. Although the ensemble size is smaller and prediction length is shorter than those in CESM-DPLE (Yeager et al., 2018), the initial results reveal that using REST initialization in DPRE leads to improved forecast skill in both SST and T295m compared to using FOSI initialization in DPFO. The improvement is specifically observed in the northern North Atlantic. Further analyses suggest that initialization shock reduction in DPRE seems to play a significant role in skill improvement. However, there is a room for further improvement of model forecast skill to improve simulation of upper ocean heat content in REST. This may be achieved by assimilating observed atmospheric forcing anomalies into the coupled predictive model.

Overall, SST- and SSS-restoring strategy in a coupled climate model brings a new perspective to decadal prediction research. Instead of assimilating three-dimensional ocean observations into coupled predictive models, which can be challenging due to the lack of deep ocean observations, decadal prediction may be benefited from assimilating only surface observations, such as SST, SSS and surface winds that are more readily available. The reduced initialization shock provided by such a modeling approach can potentially lead to improvements in decadal prediction skill.

6.2 Future Work

An immediate next step of this research is to examine whether this SST/SSS-restoring coupled model initialization strategy will remain effective if FOSI SST and SSS are replaced by observed SST and SSS as restoring target. The experiment S-SSS in which SST is restored to monthly ERSSTv5 and SSS to climatological WOA13v2 SSS can be used to initialize decadal prediction ensembles. The advantages of using S-SSS as initialization are to 1) narrow the difference between initial conditions and observations, possibly improving the prediction skill at short lead times; 2) make the results more general and independent from a specific model system, i.e. CESM FOSI.

There are several other possible improvements for initialization technique that can be tested. Based on the experience of seasonal prediction that using daily or 6-hourly observations as restoring targets can further improve model forecast skills (e.g. Keenlyside et al., 2005; Sluka et al., 2016), it is worthwhile repeating the decadal prediction experiment using daily SST observations as restoring target in coupled model initialization. Reducing model drift is another potential method to improve model

forecast skills. Theoretically, using anomaly-restoring coupled model simulations as initialization should both reduce initialization shock and model drift. But as shown in Chapter 4, anomaly-restoring can lead to inconsistency in surface density anomalies and mean density distribution, resulting in unrealistic AMOC decadal variation. One potential solution to overcome this inconsistency is to restore SST to observation while including a salinity correction based on T/S relation, so that density anomalies are more consistent with mean density distribution.

In summary, many potential improvements can be made to coupled model initialization in decadal climate prediction. The results shown in this study present only a first step to develop a comprehensive initialization approach for decadal climate prediction.

REFERENCES

Adler, R. F., Huffman, G. J., Chang, A., Ferraro, R., Xie, P. P., Janowiak, J., ... & Nelkin, E. (2003). The version-2 global precipitation climatology project (GPCP) monthly precipitation analysis (1979–present). Journal of hydrometeorology, 4(6), 1147-1167. https://doi.org/10.1175/1525-7541(2003)004<1147:TVGPCP>2.0.CO;2

Boer, G. J., Kharin, V. V., & Merryfield, W. J. (2013). Decadal predictability and forecast skill. *Climate dynamics*, 41(7-8), 1817-1833. https://doi.org/10.1007/s00382-013-1705-0

Born, A., & Mignot, J. (2012). Dynamics of decadal variability in the Atlantic subpolar gyre: a stochastically forced oscillator. *Climate dynamics*, 39(1), 461-474. https://doi.org/10.1007/s00382-011-1180-4

Bjerknes, J. (1969). Atmospheric teleconnections from the equatorial pacific. Journal of Physical Oceanography, 97(3), 163-172. https://doi.org/10.1175/1520-0493(1969)097<0163:ATFTEP>2.3.CO;2

Booth, B. B., Dunstone, N. J., Halloran, P. R., Andrews, T., & Bellouin, N. (2012). Aerosols implicated as a prime driver of twentieth-century North Atlantic climate variability. *Nature*, *484*(7393), 228-232. https://doi.org/10.1038/nature10946

Bryden, H. L., Longworth, H. R., & Cunningham, S. A. (2005). Slowing of the Atlantic meridional overturning circulation at 25 N. *Nature*, *438*(7068), 655-657. https://doi.org/10.1038/nature04385

Buckley, M. W., & Marshall, J. (2016). Observations, inferences, and mechanisms of the Atlantic Meridional Overturning Circulation: A review. *Reviews of Geophysics*, 54(1), 5-63. https://doi.org/10.1002/2015RG000493

Cane, M. A., Clement, A. C., Murphy, L. N., & Bellomo, K. (2017). Low-pass filtering, heat flux, and Atlantic multidecadal variability. Journal of Climate, 30(18), 7529-7553. https://doi.org/10.1175/JCLI-D-16-0810.1

Chen, D., Zebiak, S. E., Busalacchi, A. J., & Cane, M. A. (1995). An improved procedure for EI Nino forecasting: Implications for predictability. *Science*, 269(5231), 1699-1702. https://doi.org/10.1126/science.269.5231.1699

Clement, A., Bellomo, K., Murphy, L. N., Cane, M. A., Mauritsen, T., Rädel, G., & Stevens, B. (2015). The Atlantic Multidecadal Oscillation without a role for

ocean circulation. *Science*, *350*(6258), 320-324. https://doi.org/10.1126/science.aab3980

Counillon, F., Keenlyside, N., Bethke, I., Wang, Y., Billeau, S., Shen, M. L., & Bentsen, M. (2016). Flow-dependent assimilation of sea surface temperature in isopycnal coordinates with the Norwegian Climate Prediction Model. *Tellus A: Dynamic Meteorology and Oceanography*, 68(1), 32437. https://doi.org/10.3402/tellusa.v68.32437

Danabasoglu, G., Yeager, S. G., Kim, W. M., Behrens, E., Bentsen, M., Bi, D., ... & Canuto, V. M. (2016). North Atlantic simulations in Coordinated Ocean-ice Reference Experiments phase II (CORE-II). Part II: Inter-annual to decadal variability. *Ocean Modelling*, 97, 65-90. https://doi.org/10.1016/j.ocemod.2015.11.007

Danabasoglu, G., Lamarque, J. F., Bacmeister, J., Bailey, D. A., DuVivier, A. K., Edwards, J., ... & Hannay, C. (2020). The Community Earth System Model version 2 (CESM2). *Journal of Advances in Modeling Earth Systems*, 12(2), e2019MS001916. https://doi.org/10.1029/2019MS001916

Dunstone, N. J., & Smith, D. M. (2010). Impact of atmosphere and sub-surface ocean data on decadal climate prediction. *Geophysical Research Letters*, 37(2). https://doi.org/10.1029/2009GL041609

Dijkstra, H. A. (2006). The ENSO phenomenon: theory and mechanisms. *Advances in Geosciences*, 6, 3-15. https://doi.org/10.5194/adgeo-6-3-2006

Drews, A., Greatbatch, R. J., Ding, H., Latif, M., & Park, W. (2015). The use of a flow field correction technique for alleviating the North Atlantic cold bias with application to the Kiel Climate Model. *Ocean Dynamics*, 65(8), 1079-1093. https://doi.org/10.1007/s10236-015-0853-7

Giannini, A., Saravanan, R., & Chang, P. (2003). Oceanic forcing of Sahel rainfall on interannual to interdecadal time scales. Science, 302(5647), 1027-1030. https://doi.org/10.1126/science.1089357

Goddard, L., Kumar, A., Solomon, A., Smith, D., Boer, G., Gonzalez, P., ... & Delworth, T. (2013). A verification framework for interannual-to-decadal predictions experiments. *Climate Dynamics*, 40(1), 245-272. https://doi.org/10.1007/s00382-012-1481-2

Goldenberg, S. B., Landsea, C. W., Mestas-Nuñez, A. M., & Gray, W. M. (2001). The recent increase in Atlantic hurricane activity: Causes and

implications. *Science*, *293*(5529), 474-479. https://doi.org/10.1126/science.1060040

Good, S. A., Martin, M. J., & Rayner, N. A. (2013). EN4: Quality controlled ocean temperature and salinity profiles and monthly objective analyses with uncertainty estimates. *Journal of Geophysical Research: Oceans*, 118(12), 6704-6716. https://doi.org/10.1002/2013JC009067

Hansen, J. W. (2002). Realizing the potential benefits of climate prediction to agriculture: issues, approaches, challenges. Agricultural systems, 74(3), 309-330. https://doi.org/10.1016/S0308-521X(02)00043-4

Harris, I. C. (2019). CRU JRA v1. 1: A forcings dataset of gridded land surface blend of Climatic Research Unit (CRU) and Japanese reanalysis (JRA) data, January 1901–December 2017, University of East Anglia Climatic Research Unit, Centre for Environmental Data Analysis. published by: *University of East Anglia Climatic Research Unit, Centre for Environmental Data Analysis*, p-2905. http://dx.doi.org/10.5285/13f3635174794bb98cf8ac4b0ee8f4ed

Huang, B., Thorne, P. W., Banzon, V. F., Boyer, T., Chepurin, G., Lawrimore, J. H., ... & Zhang, H. M. (2017). Extended reconstructed sea surface temperature, version 5 (ERSSTv5): upgrades, validations, and intercomparisons. *Journal of Climate*, 30(20), 8179-8205. https://doi.org/10.1175/JCLI-D-16-0836.1

Huck, T., de Verdiere, A. C., Estrade, P., & Schopp, R. (2008). Low-frequency variations of the large-scale ocean circulation and heat transport in the North Atlantic from 1955–1998 in situ temperature and salinity data. *Geophysical Research Letters*, 35(23). https://doi.org/10.1029/2008GL035635

Hunke, E. C, Lipscomb, W. H., Turner, A. K., Jeffery, N., & Elliott, S. (2015). CICE: The Los Alamos Sea Ice Model. Documentation and Software User's Manual. Version 5.1. T-3 Fluid Dynamics Group, *Los Alamos National Laboratory*, Tech. Rep. LA-CC-06-012. https://csdms.colorado.edu/w/images/CICE_documentation_and_software_user's_manual.pdf

Iacono, M. J., Delamere, J. S., Mlawer, E. J., Shephard, M. W., Clough, S. A., & Collins, W. D. (2008). Radiative forcing by long-lived greenhouse gases: Calculations

with the AER radiative transfer models. *Journal of Geophysical Research: Atmospheres*, 113(D13). https://doi.org/10.1029/2008JD009944

Karspeck, A., Yeager, S., Danabasoglu, G., & Teng, H. (2015). An evaluation of experimental decadal predictions using CCSM4. *Climate Dynamics*, 44(3-4), 907-923. https://doi.org/10.1007/s00382-014-2212-7

Karspeck, A. R., Stammer, D., Köhl, A., Danabasoglu, G., Balmaseda, M., Smith, D. M., ... & Rosati, A. (2017). Comparison of the Atlantic meridional overturning circulation between 1960 and 2007 in six ocean reanalysis products. *Climate Dynamics*, 49(3), 957-982. https://doi.org/10.1007/s00382-015-2787-7

Keenlyside, N., Latif, M., Botzet, M., Jungclaus, J., & Schulzweida, U. (2005). A coupled method for initializing El Nino Southern Oscillation forecasts using sea surface temperature. *Tellus A: Dynamic meteorology and oceanography*, 57(3), 340-356. https://doi.org/10.3402/tellusa.v57i3.14661

Keenlyside, N. S., Latif, M., Jungclaus, J., Kornblueh, L., & Roeckner, E. (2008). Advancing decadal-scale climate prediction in the North Atlantic sector. Nature, 453(7191), 84-88. https://doi.org/10.1038/nature06921

Kim, W. M., Yeager, S., Chang, P., & Danabasoglu, G. (2018). Low-frequency North Atlantic climate variability in the Community Earth System Model large ensemble. Journal of Climate, 31(2), 787-813. https://doi.org/10.1175/JCLI-D-17-0193.1

Kobayashi, S., Ota, Y., Harada, Y., Ebita, A., Moriya, M., Onoda, H., ... & Takahashi, K. (2015). The JRA-55 reanalysis: General specifications and basic characteristics. *Journal of the Meteorological Society of Japan. Ser. II*, 93(1), 5-48. https://dx.doi.org/10.2151/jmsj.2015-001

Kostov, Y., Armour, K. C., & Marshall, J. (2014). Impact of the Atlantic meridional overturning circulation on ocean heat storage and transient climate change. *Geophysical Research Letters*, 41(6), 2108-2116. https://doi.org/10.1002/2013GL058998

Kushnir, Y., Scaife, A.A., Arritt, R. et al. Towards operational predictions of the near-term climate. Nature Clim Change 9, 94–101 (2019). https://doi.org/10.1038/s41558-018-0359-7

Kwon, Y. O., & Frankignoul, C. (2014). Mechanisms of multidecadal Atlantic meridional overturning circulation variability diagnosed in depth versus density

space. *Journal of Climate*, 27(24), 9359-9376. https://doi.org/10.1175/JCLI-D-14-00228.1

Landsea, C. W., Pielke, R. A., Mestas-Nunez, A. M., & Knaff, J. A. (1999). Atlantic basin hurricanes: Indices of climatic changes. *Climatic change*, *42*(1), 89-129. https://doi.org/10.1023/A:1005416332322

Langehaug, H. R., Rhines, P. B., Eldevik, T., Mignot, J., & Lohmann, K. (2012). Water mass transformation and the North Atlantic Current in three multicentury climate model simulations. *Journal of Geophysical Research: Oceans*, 117(C11). https://doi.org/10.1029/2012JC008021

Larson, S. M., Buckley, M. W., & Clement, A. C. (2020). Extracting the buoyancy-driven atlantic meridional overturning circulation. *Journal of Climate*, 33(11), 4697-4714. https://doi.org/10.1175/JCLI-D-19-0590.1

Latif, M., Anderson, D., Barnett, T., Cane, M., Kleeman, R., Leetmaa, A., ... & Schneider, E. (1998). A review of the predictability and prediction of ENSO. Journal of Geophysical Research: Oceans, 103(C7), 14375-14393. https://doi.org/10.1029/97JC03413

Latif, M., Roeckner, E., Botzet, M., Esch, M., Haak, H., Hagemann, S., ... & Mitchell, J. (2004). Reconstructing, monitoring, and predicting multidecadal-scale changes in the North Atlantic thermohaline circulation with sea surface temperature. *Journal of Climate*, 17(7), 1605-1614. https://doi.org/10.1175/1520-0442(2004)017<1605:RMAPMC>2.0.CO;2

Latif, M., Roeckner, E., Mikolajewicz, U., & Voss, R. (2000). Tropical stabilization of the thermohaline circulation in a greenhouse warming simulation. *Journal of Climate*, 13(11), 1809-1813. https://doi.org/10.1175/1520-0442(2000)013<1809:L>2.0.CO;2

Lawrence, D. M., Fisher, R. A., Koven, C. D., Oleson, K. W., Swenson, S. C., Bonan, G., ... & Kluzek, E. (2019). The Community Land Model version 5: Description of new features, benchmarking, and impact of forcing uncertainty. J*ournal of Advances in Modeling Earth Systems*, 11(12), 4245-4287. https://doi.org/10.1029/2018MS001583

Li, F., & Lozier, M. S. (2018). On the linkage between Labrador Sea Water volume and overturning circulation in the Labrador Sea: A case study on proxies. *Journal of Climate*, 31(13), 5225-5241. https://doi.org/10.1175/JCLI-D-17-0692.1

Li, H. Y., Wigmosta, M. S., Wu, H., Huang, M. Y., Ke, Y. H., Coleman, A. M., & Leung, L. R. (2013). A physically based runoff routing model for land surface

and Earth system models. *Journal of Hydrometeorology*, 14, 808–828. https://doi.org/10.1175/Jhm-D- 12-015.1

Lin, S. J., & Rood, R. B. (1997). An explicit flux-form semi-Lagrangian shallow-water model on the sphere. *Quarterly Journal of the Royal Meteorological Society*, 123(544), 2477-2498. https://doi.org/10.1002/qj.49712354416

Lozier, M. S., Bacon, S., Bower, A. S., Cunningham, S. A., De Jong, M. F., De Steur, L., ... & Zika, J. D. (2017). Overturning in the Subpolar North Atlantic Program: A new international ocean observing system. *Bulletin of the American Meteorological Society*, *98*(4), 737-752. https://doi.org/10.1175/BAMS-D-16-0057.1

Lozier, M. S., Li, F., Bacon, S., Bahr, F., Bower, A. S., Cunningham, S. A., ... & Zhao, J. (2019). A sea change in our view of overturning in the subpolar North Atlantic. *Science*, *363*(6426), 516-521. https://doi.org/10.1126/science.aau6592

Lu, L., Zhang, S., Yeager, S. G., Danabasoglu, G., Chang, P., Wu, L., ... & Lu, F. (2020). Impact of Coherent Ocean Stratification on AMOC Reconstruction by Coupled Data Assimilation with a Biased Model. *Journal of Climate*, 33(17), 7319-7334. https://doi.org/10.1175/JCLI-D-19-0735.1

Mann, M. E., Steinman, B. A., Brouillette, D. J., & Miller, S. K. (2021). Multidecadal climate oscillations during the past millennium driven by volcanic forcing. *Science*, 371(6533), 1014-1019. https://doi.org/10.1126/science.abc5810

Mann, M. E., Steinman, B. A., & Miller, S. K. (2020). Absence of internal multidecadal and interdecadal oscillations in climate model simulations. *Nature Communications*, 11(1), 49-9. https://doi.org/10.1038/s41467-019-13823-w

Mann, M. E., Steinman, B. A., Miller, S. K., Frankcombe, L. M., England, M. H., & Cheung, A. H. (2016). Predictability of the recent slowdown and subsequent recovery of large-scale surface warming using statistical methods. *Geophysical Research Letters*, 43(7), 3459-3467. doi:10.1002/2016GL068159

Meehl, G. A. (2021, Jun). Initialization method and model bias, drift, trends, and skill of seasonal-to-decadal (S2D) initialized climate predictions in CESM1 and E2SMv1[Video]. CESM Workshop: Earth System Predection Working Group. https://www.youtube.com/watch?v=NRHvnjkhm5w&t=11301s

Meehl, G. A., Goddard, L., Boer, G., Burgman, R., Branstator, G., Cassou, C., ... & Yeager, S. (2014). Decadal climate prediction: an update from the

trenches. *Bulletin of the American Meteorological Society*, 95(2), 243-267. https://doi.org/10.1175/BAMS-D-12-00241.1

Meehl, G. A., Goddard, L., Murphy, J., Stouffer, R. J., Boer, G., Danabasoglu, G., ... & Hegerl, G. (2009). Decadal prediction: Can it be skillful?. *Bulletin of the American Meteorological Society*, 90(10), 1467-1486. https://doi.org/10.1175/2009BAMS2778.1

Mignot, J., & Frankignoul, C. (2005). The variability of the Atlantic meridional overturning circulation, the North Atlantic Oscillation, and the El Ninõ–Southern Oscillation in the Bergen climate model. *Journal of climate*, 18(13), 2361-2375. https://doi.org/10.1175/JCLI3405.1

Moat, B. I., Smeed, D. A., Frajka-Williams, E., Desbruyères, D. G., Beaulieu, C., Johns, W. E., ... & Bryden, H. L. (2020). Pending recovery in the strength of the meridional overturning circulation at 26° N. *Ocean Science*, *16*(4), 863-874. https://doi.org/10.5194/os-16-863-2020

Mulholland, D. P., Laloyaux, P., Haines, K., & Balmaseda, M. A. (2015). Origin and impact of initialization shocks in coupled atmosphere–ocean forecasts. *Monthly Weather Review*, 143(11), 4631-4644. https://doi.org/10.1175/MWR-D-15-0076.1

Murphy, L. N., Bellomo, K., Cane, M., & Clement, A. (2017). The role of historical forcings in simulating the observed Atlantic multidecadal oscillation. *Geophysical Research Letters*, 44(5), 2472-2480. https://doi.org/10.1002/2016GL071337

Neelin, J. D., Battisti, D. S., Hirst, A. C., Jin, F. F., Wakata, Y., Yamagata, T., & Zebiak, S. E. (1998). ENSO theory. Journal of Geophysical Research: Oceans, 103(C7), 14261-14290. https://doi.org/10.1029/97JC03424

Nicholson, S. E., & Entekhabi, D. (1986). The quasi-periodic behavior of rainfall variability in Africa and its relationship to the Southern Oscillation. *Archives for meteorology, geophysics, and bioclimatology, Series A*, 34(3), 311-348. https://doi.org/10.1007/BF02257765

Ortega, P., Guilyardi, E., Swingedouw, D., Mignot, J., & Nguyen, S. (2017). Reconstructing extreme AMOC events through nudging of the ocean surface: a perfect model approach. Climate Dynamics, 49(9-10), 3425-3441. https://doi.org/10.1007/s00382-017-3521-4

Park, T., Park, W., & Latif, M. (2016). Correcting North Atlantic sea surface salinity biases in the Kiel Climate Model: influences on ocean circulation and Atlantic

Multidecadal Variability. *Climate dynamics*, 47(7), 2543-2560. https://doi.org/10.1007/s00382-016-2982-1

Penny, Stephen. (2017). Coupled Data Assimilation for Integrated Earth System Analysis and Prediction: Goals, Challenges and Recommendations. https://library.wmo.int/doc_num.php?explnum_id=10830

Philander, S. G. (1990). El Niño, La Niña, and the southern oscillation. San Diego, CA: Academic.

Polyakov, I. V., Bhatt, U. S., Simmons, H. L., Walsh, D., Walsh, J. E., & Zhang, X. (2005). Multidecadal variability of North Atlantic temperature and salinity during the twentieth century. *Journal of Climate*, 18(21), 4562-4581. https://doi.org/10.1175/JCLI3548.1

Rayner, N. A. A., Parker, D. E., Horton, E. B., Folland, C. K., Alexander, L. V., Rowell, D. P., ... & Kaplan, A. (2003). Global analyses of sea surface temperature, sea ice, and night marine air temperature since the late nineteenth century. *Journal of Geophysical Research: Atmospheres*, 108(D14). https://doi.org/10.1029/2002JD002670

Robson, J., Sutton, R., Lohmann, K., Smith, D., & Palmer, M. D. (2012). Causes of the rapid warming of the North Atlantic Ocean in the mid-1990s. *Journal of Climate*, *25*(12), 4116-4134. https://doi.org/10.1175/JCLI-D-11-00443.1

Rodríguez-Fonseca, B., Mohino, E., Mechoso, C. R., Caminade, C., Biasutti, M., Gaetani, M., ... & Polo, I. (2015). Variability and predictability of West African droughts: a review on the role of sea surface temperature anomalies. Journal of Climate, 28(10), 4034-4060. https://doi.org/10.1175/JCLI-D-14-00130.1.

Ruprich-Robert, Y., Moreno-Chamarro, E., Levine, X., Bellucci, A., Cassou, C., Castruccio, F., ... & Tourigny, E. (2021). Impacts of Atlantic multidecadal variability on the tropical Pacific: a multi-model study. *npj Climate and Atmospheric Science*, *4*(1), 1-11. https://doi.org/10.1038/s41612-021-00188-5

Sluka, T. C., Penny, S. G., Kalnay, E., & Miyoshi, T. (2016). Assimilating atmospheric observations into the ocean using strongly coupled ensemble data assimilation. *Geophysical Research Letters*, 43(2), 752-759. https://doi.org/10.1002/2015GL067238

Smeed D.; Moat B.I.; Rayner D.; Johns W.E.; Baringer M.O.; Volkov D.L.; Frajka-Williams E.(2019). Atlantic meridional overturning circulation observed by the RAPID-MOCHA-WBTS (RAPID-Meridional Overturning Circulation and Heatflux Array-Western Boundary Time Series) array at 26N from 2004 to 2018.

British Oceanographic Data Centre, National Oceanography Centre, NERC, UK. doi:10/c72s.

Smith, D. M., Eade, R., Scaife, A. A., Caron, L. P., Danabasoglu, G., DelSole, T. M., ... & Kharin, V. (2019). Robust skill of decadal climate predictions. npj Climate and Atmospheric Science, 2(1), 1-10. https://doi.org/10.1038/s41612-019-0071-y

Smith, R., Jones, P., Briegleb, B., Bryan, F., Danabasoglu, G., Dennis, J., ... & Hecht, M. (2010). The parallel ocean program (POP) reference manual: ocean component of the community climate system model (CCSM) and community earth system model (CESM). *LAUR-01853*, 141, 1-140. https://www.cesm.ucar.edu/models/cesm2/ocean/doc/sci/POPRefManual.pdf

Swingedouw, D., Mignot, J., Labetoulle, S., Guilyardi, E., & Madec, G. (2013). Initialisation and predictability of the AMOC over the last 50 years in a climate model. *Climate dynamics*, 40(9-10), 2381-2399. https://doi.org/10.1007/s00382-012-1516-8

Tang, Y., Zhang, R. H., Liu, T., Duan, W., Yang, D., Zheng, F., ... & Mu, M. (2018). Progress in ENSO prediction and predictability study. *National Science Review*, 5(6), 826-839. https://doi.org/10.1093/nsr/nwy105

Tsujino, H., Urakawa, S., Nakano, H., Small, R. J., Kim, W. M., Yeager, S. G., ... & Böning, C. W. (2018). JRA-55 based surface dataset for driving ocean–sea-ice models (JRA55-do). *Ocean Modelling*, 130, 79-139. https://doi.org/10.1016/j.ocemod.2018.07.002

Tung, K. K., Chen, X., Zhou, J., & Li, K. F. (2019). Interdecadal variability in pan-Pacific and global SST, revisited. *Climate Dynamics*, 52(3-4), 2145–2157. https://doi.org/10.1007/s00382-018-4240-1

Villamayor, J., & Mohino, E. (2015). Robust Sahel drought due to the Interdecadal Pacific Oscillation in CMIP5 simulations. Geophysical Research Letters, 42(4), 1214-1222. https://doi.org/10.1002/2014GL062473

Wallace, J. M., Rasmusson, E. M., Mitchell, T. P., Kousky, V. E., Sarachik, E. S., & Von Storch, H. (1998). On the structure and evolution of ENSO-related climate variability in the tropical Pacific: Lessons from TOGA. *Journal of Geophysical Research: Oceans*, 103(C7), 14241-14259. https://doi.org/10.1029/97JC02905

Wang, Y., Counillon, F., Keenlyside, N., Svendsen, L., Gleixner, S., Kimmritz, M., ... & Gao, Y. (2019). Seasonal predictions initialised by assimilating sea surface

temperature observations with the EnKF. *Climate Dynamics*, 53(9), 5777-5797. https://doi.org/10.1007/s00382-019-04897-9

Wills, R. C., Armour, K. C., Battisti, D. S., & Hartmann, D. L. (2019). Ocean–atmosphere dynamical coupling fundamental to the Atlantic multidecadal oscillation. *Journal of Climate*, 32(1), 251-272. https://doi.org/10.1175/JCLI-D-18-0269.1

Xu, X., Chassignet, E. P., & Wang, F. (2019). On the variability of the Atlantic meridional overturning circulation transports in coupled CMIP5 simulations. *Climate Dynamics*, 52(11), 6511-6531. https://doi.org/10.1007/s00382-018-4529-0

Yan, X., Zhang, R., & Knutson, T. R. (2017). The role of Atlantic overturning circulation in the recent decline of Atlantic major hurricane frequency. *Nature Communications*, *8*(1), 1-8.

Yan, X., Zhang, R., & Knutson, T. R. (2018). Underestimated AMOC variability and implications for AMV and predictability in CMIP models. *Geophysical Research Letters*, *45*(9), 4319-4328. https://doi.org/10.1029/2018GL077378

Yeager, S. (2020). The abyssal origins of North Atlantic decadal predictability. *Climate Dynamics*, 55(7), 2253-2271. https://doi.org/10.1007/s00382-020-05382-4

Yeager, S. (2021). Seasonal-to-Multiyear Large Ensemble (SMYLE): A new Earth system prediction dataset using CESM2 [PowerPoint slides]. CESM Earth System Prediction Working Group. https://www.cesm.ucar.edu/events/wg-meetings/2021/files/system/Yeager.pdf

Yeager, S., Castruccio, F., Chang, P., Danabasoglu, G., Maroon, E., Small, J., ... & Zhang, S. (2021). An outsized role for the Labrador Sea in the multidecadal variability of the Atlantic overturning circulation. *Science advances*, 7(41), eabh3592. https://doi.org/10.1126/sciadv.abh3592

Yeager, S. G., Danabasoglu, G., Rosenbloom, N. A., Strand, W., Bates, S. C., Meehl, G. A., ... & Lovenduski, N. S. (2018). Predicting near-term changes in the Earth System: A large ensemble of initialized decadal prediction simulations using the Community Earth System Model. *Bulletin of the American Meteorological Society*, 99(9), 1867-1886. https://doi.org/10.1175/BAMS-D-17-0098.1

Yeager, S., Karspeck, A., Danabasoglu, G., Tribbia, J., & Teng, H. (2012). A decadal prediction case study: Late twentieth-century North Atlantic Ocean heat

content. Journal of Climate, 25(15), 5173-5189. https://doi.org/10.1175/JCLI-D-11-00595.1

Yeager, S. G., & Robson, J. I. (2017). Recent progress in understanding and predicting Atlantic decadal climate variability. *Current Climate Change Reports*, *3*(2), 112-127. https://doi.org/10.1007/s40641-017-0064-z

Zhang, R. (2007). Anticorrelated multidecadal variations between surface and subsurface tropical North Atlantic. *Geophysical Research Letters*, *34*(12). https://doi.org/10.1029/2007GL030225

Zhang, R. (2010a). Latitudinal dependence of Atlantic meridional overturning circulation (AMOC) variations. *Geophysical Research Letters*, 37(16). https://doi.org/10.1029/2010GL044474

Zhang, R. (2010b). Northward intensification of anthropogenically forced changes in the Atlantic meridional overturning circulation (AMOC). *Geophysical Research Letters*, 37(24). https://doi.org/10.1029/2010GL045054

Zhang, R., & Delworth, T. L. (2007). Impact of the Atlantic multidecadal oscillation on North Pacific climate variability. *Geophysical Research Letters*, *34*(23). https://doi.org/10.1029/2007GL031601

Zhang, R., Delworth, T. L., Sutton, R., Hodson, D. L., Dixon, K. W., Held, I. M., ... & Vecchi, G. A. (2013). Have aerosols caused the observed Atlantic multidecadal variability?. *Journal of the Atmospheric Sciences*, *70*(4), 1135-1144. https://doi.org/10.1175/JAS-D-12-0331.1

Zhang, R., Sutton, R., Danabasoglu, G., Delworth, T. L., Kim, W. M., Robson, J., & Yeager, S. G. (2016). Comment on "The Atlantic Multidecadal Oscillation without a role for ocean circulation". *Science*, *352*(6293), 1527-1527. https://doi.org/10.1126/science.aaf1660

Zhang, R., Sutton, R., Danabasoglu, G., Kwon, Y. O., Marsh, R., Yeager, S. G., ... & Little, C. M. (2019). A review of the role of the Atlantic meridional overturning circulation in Atlantic multidecadal variability and associated climate impacts. *Reviews of Geophysics*, 57(2), 316-375. https://doi.org/10.1029/2019RG000644

Zhang, S., Harrison, M. J., Rosati, A., & Wittenberg, A. (2007). System design and evaluation of coupled ensemble data assimilation for global oceanic climate

studies. *Monthly Weather Review*, 135(10), 3541-3564. https://doi.org/10.1175/MWR3466.1

Zhu, J., Kumar, A., Lee, H. C., & Wang, H. (2017). Seasonal predictions using a simple ocean initialization scheme. *Climate Dynamics*, 49(11), 3989-4007. https://doi.org/10.1007/s00382-017-3556-6

Zweng, M.M, J.R. Reagan, J.I. Antonov, R.A. Locarnini, A.V. Mishonov, T.P. Boyer, H.E. Garcia, O.K. Baranova, D.R. Johnson, D.Seidov, M.M. Biddle, 2013. World Ocean Atlas 2013, Volume 2: Salinity. S. Levitus, Ed., A. Mishonov Technical Ed.; NOAA Atlas NESDIS 74, 39. https://www.ncei.noaa.gov/data/oceans/woa/WOA13/DOC/woa13_vol2.pdf